

**Analysis of GNSS-R Observations for Altimetry and  
Characterization of Earth Surfaces**

by

**Jake R. Mashburn**

B.S., Aerospace Engineering, University of Tennessee Knoxville, 2012

M.S., Aerospace Engineering Sciences, University of Colorado at  
Boulder, 2014

A thesis submitted to the  
Faculty of the Graduate School of the  
University of Colorado in partial fulfillment  
of the requirements for the degree of  
Doctor of Philosophy  
Department of Aerospace Engineering Sciences

2018

This thesis entitled:  
Analysis of GNSS-R Observations for Altimetry and Characterization of Earth Surfaces  
written by Jake R. Mashburn  
has been approved for the Department of Aerospace Engineering Sciences

---

Dr. Penina Axelrad

---

Dr. Kristine Larson

Date \_\_\_\_\_

The final copy of this thesis has been examined by the signatories, and we find that both the content and the form meet acceptable presentation standards of scholarly work in the above mentioned discipline.

Mashburn, Jake R. (Ph.D., Aerospace Engineering Sciences)

Analysis of GNSS-R Observations for Altimetry and Characterization of Earth Surfaces

Thesis directed by Dr. Penina Axelrad

Global Navigation Satellite Systems (GNSS) provide abundant, opportunistic signals that can be used to probe the Earth’s environment and surface. Utilizing reflected GNSS signals for remote sensing is called GNSS Reflectometry (GNSS-R). Sensing of the ocean, land, and ice, with potentially dense measurement coverage and rapid revisit times, is possible due to the distributed geometry of GNSS constellations. GNSS-R can provide some advantages over other Earth observation systems, like traditional radar altimeters or microwave radiometers. GNSS signals are well characterized and encoded with precise ranging and timing information. There are multiple transmitters in view at any time, and GNSS signals occupy a protected frequency band (L-band) that penetrates Earth’s atmosphere in all weather conditions.

This dissertation focuses on the development of methods and analysis techniques to observe sea surface height and sea ice extent with reflected GNSS signals. A tool-kit is developed to take advantage of experimental data sets from aircraft and spacecraft, and to produce state-of-the-art altimetric retrievals. Algorithms for the re-tracking of altimetric delays are demonstrated. Techniques to characterize and models to correct GNSS-R path delay errors are built through analysis of TechDemoSat-1 (TDS-1) and NASA’s Cyclone Global Navigation Satellite System (CYGNSS) flight data. Neither TDS-1 nor CYGNSS were designed to make precise altimetry observations. Thus, this work evaluates practical performance limitations of these GNSS-R observations, and establishes requirements for future missions. Altimetry results with height retrieval standard deviation of  $\sigma_H = 11$  m with 1 sec and  $\sigma_H = 3.8$  m with 10 sec observations, are shown.

This work creates a foundation of techniques that can support future GNSS-R mis-

sions dedicated to ocean surface altimetry by producing results with sufficient accuracy and precision to the ocean science community. These tools are built to inform future mission designs and aid scientific interpretation of GNSS-R measurements.



## Dedication

For my parents.

## Acknowledgments

Through the past six years I have had the tremendous opportunity to work with Dr. Penina Axelrad. Your guidance helped shape a collection of figures and numbers into a story worth telling and something to be proud of. Thank you.

Thank you to Dr. Kristine Larson. You helped to support my work when I needed it most. Thank you for being my teacher and mentor.

I spent three of these summers at the NASA Jet Propulsion Laboratory and have had the opportunity to work on CYGNSS and SMAP projects thanks to support from Dr. Cinzia Zuffada and Dr. Stephen Lowe. You have both been invaluable in this work.

Thank you to my committee members - Dr. Dallas Masters, Dr. Dennis Akos, and Dr. Cora Randall - each of whom provided valuable technical assistance and perspective.

I have benefited from many more notable advisors. The following individuals have generously shared their ideas, code, data, and knowledge. Thank you to Dr. Clara Chew, Stephan Esterhuizen, Dr. Scott Gleason, Dr. Andrew O'Brien, Dr. Valery Zavorotny, Dr. Attila Komjathy, Dr. Anthony Mannucci, Dr. Bruce Haines, and Dr. Victor Zlotnicki.

This dissertation is the culmination and product of my life's most challenging chapter yet. The past years have spanned the full range of emotions with many beginnings and ends. I've learned as much in life as in school, and have spent a relatively short amount of time feeling like an "expert" in anything. My success here is due in tremendous amounts to the unwavering support of my family, friends, and colleagues. Without you, I would absolutely not be writing this now. Thank you, it means more than I know how to express in words. I owe you all so much, and I wish for you everything that is good.

## Contents

### Chapter

|          |  |    |
|----------|--|----|
| <b>1</b> | Introduction   | 1  |
| <b>2</b> | Background and Theory  | 6  |
| 2.1      | Bistatic Radar Signal Scattering . . . . .   | 6  |
| 2.2      | GNSS-R Receiver Operations . . . . .   | 12 |
| 2.3      | Brief Review of GNSS-R Ocean and Sea Ice Remote Sensing . . . . .  | 15 |
| 2.4      | GNSS-R Space Missions . . . . .  | 17 |
| <b>3</b> | An Assessment of the Precision and Accuracy of Altimetry Retrievals for a Monterey Bay GNSS-R Experiment | 19 |
| 3.1      | Introduction . . . . .   | 20 |
| 3.2      | Experimental Campaign and Data Set . . . . .   | 22 |
| 3.2.1    | Data Collection Campaign . . . . .   | 22 |
| 3.2.2    | GNSS-R Instrument . . . . .  | 22 |
| 3.2.3    | Data Set . . . . .   | 23 |
| 3.3      | Methodology . . . . .  | 24 |
| 3.3.1    | Specular Delay Tracking Algorithms . . . . .   | 24 |
| 3.3.2    | Delay Model . . . . .  | 27 |
| 3.3.3    | Surface Height Retrieval . . . . .   | 29 |
| 3.3.4    | Measurement Precision Calculation . . . . .  | 30 |

|          |  |           |
|----------|--|-----------|
| 3.4      | Results . . . . .  | 30        |
| 3.4.1    | Precision . . . . .  | 30        |
| 3.4.2    | Accuracy . . . . .   | 35        |
| 3.5      | Conclusions and Future Work . . . . .                                  | 41        |
| <b>4</b> | <b>Global Ocean Altimetry With GNSS Reflections From TechDemoSat-1</b> | <b>44</b> |
| 4.1      | Introduction . . . . .   | 45        |
| 4.2      | Spaceborne GNSS-R with TechDemoSat-1 . . . . .                         | 47        |
| 4.3      | Ocean Altimetry Retrieval Methods . . . . .                            | 50        |
| 4.3.1    | Reflection Modeling . . . . .  | 51        |
| 4.3.2    | DDM Re-tracking . . . . .  | 60        |
| 4.3.3    | On-board Delay Calculation and DDM Correlator Positioning . . . . .    | 62        |
| 4.3.4    | TDS-1 On-board Model Calibration . . . . .                             | 63        |
| 4.4      | Results . . . . .  | 65        |
| 4.5      | Summary and Conclusions . . . . .                                      | 69        |
| <b>5</b> | <b>Modeling GNSS-R Reflections</b>                                     | <b>72</b> |
| 5.1      | Modeling Coherent and Diffuse Scattering . . . . .                     | 73        |
| 5.2      | A MATLAB Implementation of VZ18 . . . . .                              | 75        |
| 5.3      | Modifications to VZ18 . . . . .  | 79        |
| 5.3.1    | Modeling Limited Receiver Bandwidth . . . . .                          | 79        |
| 5.3.2    | Modeling Continuous Azimuthal Geometries . . . . .                     | 80        |
| 5.3.3    | Modeling the CYGNSS Antenna Pattern . . . . .                          | 82        |
| 5.4      | Model Representations of CYGNSS GNSS-R Data . . . . .                  | 83        |
| <b>6</b> | <b>GNSS-R Altimetry Methods</b>  | <b>86</b> |
| 6.1      | Mapping Path Delay to Reflector Height . . . . .                       | 87        |
| 6.2      | Altimetric Delay Re-tracking . . . . .                                 | 89        |

|          |   |            |
|----------|---|------------|
| 6.2.1    | Single Point Re-trackers . . . . .  | 90         |
| 6.2.2    | Re-tracking in the Presence of Coherent Measurements . . . . .            | 92         |
| 6.2.3    | Model Re-trackers . . . . .   | 99         |
| 6.2.4    | VZ18 DDM Re-tracking . . . . .  | 100        |
| 6.2.5    | Re-tracking Error Statistics . . . . .                                    | 102        |
| 6.3      | Reflection Modeling . . . . .   | 106        |
| 6.3.1    | Receiver and Transmitter Orbits . . . . .                                 | 106        |
| 6.3.2    | Model Target Surface and Specular Point Prediction . . . . .              | 109        |
| 6.3.3    | Ionospheric Delay . . . . .   | 113        |
| 6.3.4    | Tropospheric Delay . . . . .  | 118        |
| 6.3.5    | Bistatic Antenna Baseline Effect . . . . .                                | 119        |
| 6.3.6    | Future Components of the High-fidelity Model . . . . .                    | 120        |
| <b>7</b> | <b>Analysis of CYGNSS GNSS-R Observations for Ocean Surface Altimetry</b> | <b>122</b> |
| 7.1      | Introduction . . . . .  | 122        |
| 7.2      | CYGNSS Mission Description . . . . .                                      | 123        |
| 7.3      | The CYGNSS GNSS-R Receiver and Observations . . . . .                     | 123        |
| 7.4      | CYGNSS Onboard Processing and Issues for Altimetry . . . . .              | 125        |
| 7.5      | A Case Study in Indonesia . . . . .                                       | 127        |
| 7.6      | Analyzing CYGNSS Data . . . . .   | 129        |
| 7.6.1    | Effects of Precise Orbit Determination . . . . .                          | 131        |
| 7.6.2    | Re-tracking in the Presence of Coherent Signals . . . . .                 | 134        |
| 7.7      | CYGNSS Height Retrievals in Indonesia . . . . .                           | 138        |
| 7.8      | Conclusions . . . . .   | 141        |
| <b>8</b> | <b>Sea Ice Detection Methodology and Preliminary Results</b>              | <b>148</b> |
| 8.1      | Introduction . . . . .  | 148        |
| 8.2      | TDS-1 GNSS-R Data and Ancillary Sea Ice Data . . . . .                    | 149        |

|          |   |            |
|----------|---|------------|
| 8.3      | Ice Detection Methodology . . . . .     | 149        |
| 8.4      | Ice Detection Results . . . . .         | 151        |
| 8.5      | Future Work . . . . .                   | 152        |
| <b>9</b> | <b>Conclusions and Future Work</b>      | <b>154</b> |
| 9.1      | Research Summary . . . . .              | 154        |
| 9.2      | Considerations Moving Forward . . . . . | 156        |
|          | <b>Bibliography</b>                     | <b>157</b> |

## Tables

### Table

|     |   |     |
|-----|---|-----|
| 3.1 | Standard deviation of altitude measurement residuals for each of the three timing algorithms over various incoherent integration times. . . . . | 32  |
| 4.1 | TDS-1 HiFi delay model error breakdown. . . . .   | 53  |
| 4.2 | Residual delay and height anomalies from TDS-1 altimetry combining data sets RD17 and 18. . . . .   | 65  |
| 4.3 | Budget of residual measurement errors for a 1 second integration time. . . .  | 66  |
| 6.1 | Re-tracking precision with the VZ18WAVE and VZ18DDM algorithms as a function of synthetic observation SNR. . . . .                              | 104 |
| 6.2 | High-fidelity path delay model error breakdown. . . . .   | 107 |
| 7.1 | CYGNSS data level definitions. . . . .  | 124 |
| 7.2 | CYGNSS specific table of error contributions. . . . .   | 130 |
| 7.3 | Surface height retrieval standard deviation with the P70 and VZ18DDM re-tracking methods. . . . .   | 141 |
| 8.1 | Arctic GNSS-R sea ice detection results as compared to the OSISAF sea ice concentration products. . . . .                                       | 152 |

## Figures

### Figure

|      |  |    |
|------|--|----|
| 2.1  | Spaceborne GNSS bistatic radar. . . . .  | 7  |
| 2.2  | Specular reflection geometry. . . . .  | 8  |
| 2.3  | The GNSS-R glistening zone is divided into delay and Doppler bins. . . . .                                   | 10 |
| 2.4  | An example delay-Doppler map (DDM) and glistening zone map. . . . .  | 11 |
| 2.5  | Illustration of mapping from the glistening zone to delay-Doppler space. . . . .                             | 13 |
| 2.6  | Block diagram of a typical GNSS-R receiver. . . . .  | 14 |
| 3.1  | Planned flight pattern over Monterey Bay, California, USA. . . . .   | 21 |
| 3.2  | A one-second incoherently integrated waveform. . . . .   | 23 |
| 3.3  | Components of the PARA3 waveform model. . . . .  | 26 |
| 3.4  | Measured aircraft heights and the residual from the ellipsoid height. . . . .                                | 31 |
| 3.5  | Surface height retrievals in Monterey Bay from 5 sec observations. . . . .                                   | 33 |
| 3.6  | Height anomaly in Monterey Bay with 5 sec observations. . . . .  | 34 |
| 3.7  | MB4 height anomaly plotted versus time. . . . .  | 36 |
| 3.8  | MB4 correlation waveform width plotted versus time. . . . .  | 37 |
| 3.9  | Monterey Bay delay anomaly plotted versus waveform width. . . . .  | 39 |
| 3.10 | Leg 9 surface heights, height anomalies, and residual distributions from MB4PM,<br>MB5AM, and MB5PM. . . . . | 41 |
| 4.1  | Spacebased GNSS-R and the TDS-1 global coverage in 4 days. . . . .   | 48 |



|     |   |    |
|-----|---|----|
| 4.2 | Example TDS-1 ocean reflection DDM. . . . .   | 50 |
| 4.3 | Ionospheric delay model. . . . .  | 57 |
| 4.4 | Example of P70 re-tracking on a measured correlation waveform. . . . .  | 61 |
| 4.5 | Delay retracking on a TDS-1 DDM. . . . .  | 62 |
| 4.6 | Global measured surface heights and height anomalies from TDS-1 data. . . .   | 67 |
| 4.7 | Delay anomaly distribution and residual. . . . .  | 68 |
| 4.8 | Estimated tracking error of the reflected signal as a function of SNR. . . . .  | 68 |
| 5.1 | Illustration of the radially oriented discrete surface grid utilized in the VZ18<br>model. . . . .                    | 76 |
| 5.2 | Modeled components of the bistatic radar equation projected onto the reflect-<br>ing surface. . . . .                 | 78 |
| 5.3 | Modeling the CYGNSS bandlimited waveform. . . . .   | 80 |
| 5.4 | Measured CYGNSS antenna pattern. . . . .  | 82 |
| 5.5 | Modeled effect of the receiver antenna pattern on the DDM. . . . .  | 84 |
| 5.6 | Example VZ18 model fit with an observed DDM from CYGNSS. . . . .  | 85 |
| 6.1 | Illustration of some common altimetry terms. . . . .  | 87 |
| 6.2 | Estimated error from linearized delay to height mapping. . . . .  | 89 |
| 6.3 | Example of P70 point tracking on a measured waveform. . . . .   | 91 |
| 6.4 | Illustration of the change in specular reflection tracking point on coherent and<br>diffuse waveforms. . . . .        | 92 |
| 6.5 | Measured P70 delay anomaly correlation with SNR and waveform width. . .   | 94 |
| 6.6 | Delay anomaly distribution with and without consideration of coherent reflec-<br>tions using PEAK tracking. . . . .   | 95 |
| 6.7 | Height anomaly retrievals in Indonesia with and without considering coherent<br>reflections by PEAK tracking. . . . . | 96 |
| 6.8 | P70 + PEAK delay anomaly plotted against waveform width. . . . .  | 97 |

|      |  |     |
|------|--|-----|
| 6.9  | The predicted P70 delay re-tracking error on VZ18 simulated observations. .                        | 97  |
| 6.10 | Calibrated P70 delay re-tracking results as a function of waveform width. . .                      | 98  |
| 6.11 | Sensitivity of power-normalized VZ18 waveforms to wind speed. . . . .                              | 99  |
| 6.12 | Examples of VZ18 Waveform model fitting to characteristic CYGNSS obser-<br>vations. . . . .        | 101 |
| 6.13 | VZ18 waveform re-tracking cost versus reflected signal range rate. . . . .                         | 101 |
| 6.14 | VZ18DDM retrieved Doppler versus reflection azimuth. . . . .                                       | 103 |
| 6.15 | P70, VZ18WAVE, and VZ18DDM re-tracking precision versus SNR. . . . .                               | 105 |
| 6.16 | RIC orbit differences between CYGNSS point solutions and GipsyX filtered<br>solution. . . . .      | 109 |
| 6.17 | Difference between DTU15 and DTU10 MSS models. . . . .   | 110 |
| 6.18 | Delay prediction error with the quasi-spherical Earth model. . . . .                               | 112 |
| 6.19 | Predicted change in P70 re-track delay for Doppler shifted correlation wave-<br>forms. . . . .     | 113 |
| 6.20 | Ionospheric delay model. . . . .   | 115 |
| 6.21 | CYGNSS Delay anomaly before and after considering the GIM ionosphere<br>corrections. . . . .       | 117 |
| 6.22 | Delay anomaly before and after considering IRI-2012 ionosphere corrections.                        | 118 |
| 6.23 | CYGNSS body frame illustration. . . . .  | 121 |
| 7.1  | CYGNSS onboard path delay prediction and a method of compensation for<br>quantized values. . . . . | 126 |
| 7.2  | Observed coherence patterns with correlation waveform width and SNR across<br>Indonesia. . . . .   | 128 |
| 7.3  | CYGNSS retrieved surface heights in Indonesia compared to the DTU10 MSS<br>model. . . . .          | 132 |

|      |  |     |
|------|--|-----|
| 7.4  | Change in height anomaly from the GipsyX orbit solutions decomposed into radial, in-track, and cross-track components. . . . . | 133 |
| 7.5  | Change in height anomaly when using GipsyX filtered orbit solutions. . . . .   | 134 |
| 7.6  | Delay anomaly versus waveform width comparing P70 and VZ18WAVE. . . . .  | 136 |
| 7.7  | CYGNSS height anomaly in Indonesia with P70 and VZ18WAVE re-tracking. . . . .  | 137 |
| 7.8  | VZ18DDM delay anomaly vs correlation waveform width. . . . .   | 138 |
| 7.9  | P70 1 sec height anomaly in Indonesia. . . . .   | 144 |
| 7.10 | P70 10 sec height anomaly in Indonesia. . . . .  | 145 |
| 7.11 | VZ18DDM 10 sec height anomaly in Indonesia. . . . .  | 146 |
| 7.12 | Ascending and descending track delay anomaly, waveform width, and SNR. . . . .   | 147 |
| 8.1  | Example ice and water DDMs from TDS-1. . . . .   | 150 |
| 8.2  | Distribution of arctic reflection events by correlation SNR and delay waveform width. . . . .                                  | 151 |
| 8.3  | Detailed look at ice retrievals in the Sea of Okhotsk and Bearing Sea. . . . .   | 153 |

## **Chapter 1**

### **Introduction**

Radar remote sensing has become a tool of principal importance in the fields of science and engineering since its invention in the 20th century. The ability to probe targets from afar opens a world of possibilities for scientific applications and associated engineering challenges. When deployed in orbit, radar remote sensing has significantly advanced or enabled many new fields of study and technologies including: Earth and planetary sciences, oceanography, wireless communications, and atmospheric sounding.

Recently, NASA has developed the Technology Roadmaps to guide the direction of technology development for planetary research [NASA, 2015]. These roadmaps identify the need for cost effective means to allow continuous observation of the earth. A focus is placed on “low power radar electronics and on-board data processing” to “open new mission opportunities, including small satellite bus architectures.” They call on researchers and engineers to find efficient ways to do science, while increasing the performance of new radar concepts, all within a limited frequency space. Utilization of signals-of-opportunity to repurpose existing resources for new scientific applications is an obvious choice to meet these goals.

Signals from Global Navigation Satellite System (GNSS) satellites are a powerful choice for opportunistic, multi-static, remote sensing of diverse surface types around the globe. GNSS signals are abundantly available; each signal is well characterized and encoded with precise ranging and timing information; and they are designed to have low cross-correlation properties. Furthermore, GNSS signals occupy a protected frequency band (L-band) that

also penetrates Earth’s atmosphere.

The techniques for bistatic remote sensing with reflected GNSS signals are collectively referred to as GNSS Reflectometry (GNSS-R). GNSS-R will, in some cases, fill a complementary role along side requirements driven and optimized remote sensing missions. This is certainly the case for the applications considered in this dissertation. A complementary data source can better resolve features on scales that were previously difficult to observe, and maintain continuous measurement records.

This work considers the application of GNSS-R techniques for ocean surface altimetry and polar sea ice detection. There is a strong scientific interest in measuring sea level and sea ice extent to better inform global weather models and understand long-term climate trends. More specifically, mesoscale ocean topography features ( $\sim 50 - 100$  km horizontal and  $\sim 0.1 - 1$  m vertical) are critical parts of the energy transport system within the ocean [Delworth et al., 2012; Drijfhout, 1994; Farneti et al., 2010]. Thus, several dedicated and high-performance spaceborne observatories have already been deployed (e.g. JASON-2 [Lambin et al., 2010] and AMSR [NSIDC, 2001]).

Traditional ocean surface altimetry relies on wide-band, active radar observations. Spaceborne altimeters are flown in geodetic orbits that repeatedly over-fly the same ground-tracks. The JASON-2 spacecraft, for example, revisits the same ground-track every 10 days [Lambin et al., 2010]. Traditional altimeters are nadir-viewing, observing only the surface directly beneath the spacecraft. While these traditional systems are able to make very precise ocean height observations ( $\leq 10$  cm error [Lambin et al., 2010]), the constraints in revisit time and observation density leave significant measurement gaps. At the equator, the geodetic orbit ground-tracks are  $\sim 300$  km apart. Thus, mesoscale ocean topography features, like eddies, are difficult to resolve using the traditional configuration. A small constellation of GNSS-R spacecraft has the potential to sample the surface with faster revisit times, and from non-repeating orbital geometries. Sampling between the geodetic repeat tracks in time and in space would allow GNSS-R altimetry to resolve ocean height signals that were not

previously possible.

It is important to recognize the complementary role of such GNSS-R measurements. There are inherent limitations of the GNSS-R techniques and signal structures for some remote sensing applications. For example, the relatively low bandwidth with which the GPS L1 C/A code is typically tracked (2 MHz bandwidth) as compared to the JASON-3 Poseidon 3B altimeter (320 MHz bandwidth) means that the GNSS-R 1-second measurement performance will likely always be inferior. However, unlike active altimeters, GNSS-R instrumentation can be flown feasibly on a constellation of small satellites, providing an opportunity to have several benefits that would otherwise be difficult to achieve. Li et al. [2016] have recently shown that, combined with advanced data assimilation techniques, GNSS-R altimetry measurements could be used to aid in retrieving mesoscale ocean topography features.

My work focuses on the development of retrieval methods, error correction models, calibration procedures, and performance analysis tools that can facilitate the use of GNSS-R measurements for altimetry and other applications. With an emphasis on analysis of flight data, this dissertation attempts to advance the state-of-the-art capabilities of GNSS-R altimetry and sea ice detection retrievals some steps closer to the theoretical boundaries of the measurement. Contributions in these areas will allow engineers and science users to make informed decisions about novel receiver design, mission proposals, and appropriate interpretation of their results.

Specifically, the contributions of this work include

- (1) A comparison analysis of the reflection tracking performance between single point methods and waveform model fitting methods including both empirical (PARA3) [Mashburn et al., 2016] and physical (VZ18) [Mashburn et al., 2018; Zavorotny and Voronovich, 2000] models.
- (2) Characterization of re-tracking performance of “single-point” and model-based methods in the presence of both weak and strong diffuse scattering.

- (3) The first estimates of accuracy of experimental airborne and spaceborne GNSS-R ocean surface altimetry measurements using GPS L1 P(Y) and C/A codes respectively [Mashburn et al., 2016, 2018].
- (4) The first global analysis of spaceborne ocean surface altimetry with GNSS-R flight data [Mashburn et al., 2018].
- (5) Development of GNSS- R propagation error correction models accounting for precise geometry and reflecting surface models, ionosphere delays, and neutral atmosphere delays [Mashburn et al., 2016, 2018].
- (6) Development and validation of methods to calibrate spacecraft timing and measurement biases in precise applications such as ocean surface altimetry.
- (7) Development of a sea ice detection method that has strong sensitivity to the presence of ice (Probability of detection  $\approx 0.97$ ).

The following chapters of this dissertation cover the theoretical background, methodology and results for ocean altimetry and sea ice detection, and a summary of the novel contributions to the field. Chapter 2 gives the background of using GNSS signals as a bistatic radar including a review of previous work and space missions flown. Subsequently, Chapters 3 and 4 describe the methods and results from two studies concerning GNSS-R ocean altimetry from aircraft and spacecraft platforms. These chapters are reproductions of the published articles “An Assessment of the Precision and Accuracy of Altimetry Retrievals for a Monterey Bay GNSS-R Experiment” [Mashburn et al., 2016] and “Global Ocean Altimetry With GNSS Reflections From TechDemoSat-1” [Mashburn et al., 2018]. The methods used in Chapters 3 and 4 are improved upon in Chapters 5 and 6. Chapter 5 details the Zavorotny and Voronovich model for GNSS-R observations and my modifications to improve the fit with CYGNSS spaceborne observations. The principles of ocean altimetry with GNSS-R and the methods to retrieve spaceborne altimetry observations are presented in Chapter 6.

Chapter 7 presents the altimetry results of a case study in Indonesia, based on data from the CYGNSS mission. A technique for the detection of sea ice and some preliminary results based on data from TDS-1 are presented in Chapter 8. Finally, Chapter 9 summarizes the contributions of this thesis and discusses some potential future directions.



## Chapter 2

### Background and Theory

GNSS Reflectometry (GNSS-R) is a remote-sensing technique that makes use of GNSS ranging signals in a bistatic configuration. By utilizing the echoes of the navigation transmissions originating from a GNSS transmitter, the passive GNSS-R receiver benefits from the continuous availability of previously existing sources. The inherent features that come from the use of existing, reliable, and distributed sources provide the main advantages of GNSS-R over other monostatic systems.

#### 2.1 Bistatic Radar Signal Scattering

Bistatic radar describes a system in which the radio transmitter and receiver are not collocated; and typically, the signal is scattered from the target in the forward direction. This configuration allows two links, a direct link and reflection link, to connect the transmitter with the receiver. Figure 2.1 illustrates the direct and reflected links for spaceborne GNSS-R. Transmissions along the direct link of a bistatic system are used for communication between transmitter and receiver. In the case of GNSS-R, the direct link is used for the conventional navigation and timing processing of a traditional GNSS receiver. The bistatic reflection link follows a path from the transmitter to the target and then to the receiver. This reflection link is then used to study a target, which is often the surface of the earth.

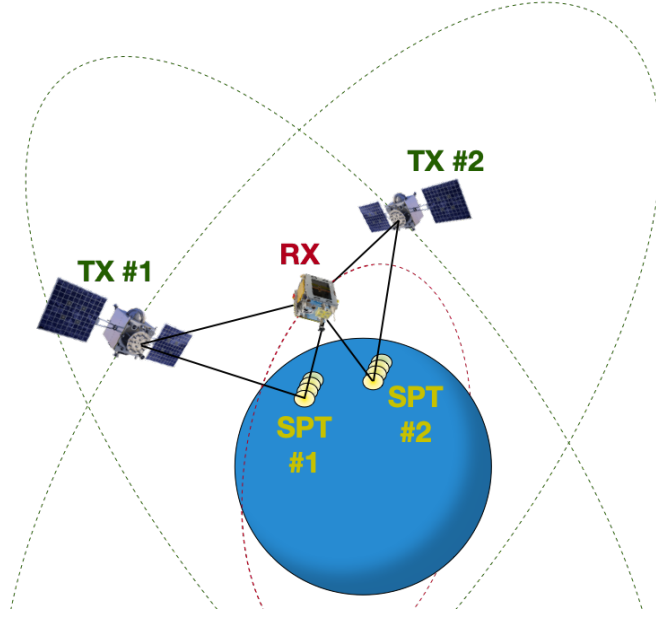


Figure 2.1: Spaceborne GNSS bistatic radar. As the transmitters (TX 1 and 2) and receiver (RX) orbit the Earth, the specular reflections (SPT 1 and 2) track along the surface. Yellow ellipses represent sequential glistering zones tracking along the surface.

A portion of the signal scattered by the target is directed toward the receiver. Information about the target can be gained from the amount of scattered power received, the excess time of flight with respect to the direct, the change in polarization, and the signal phase. The bistatic radar receiver is designed to measure these quantities, and thus gather information about the target surface.

The shortest path connecting the transmitter, target, and receiver is called the specular reflection path. Figure 2.2 illustrates the specular reflection geometry. The specular reflection path is incident on the reflecting surface at an angle  $\gamma_I$  and reflects at the same angle  $\gamma_R = \gamma_I$  relative to the surface normal. The incident signal scatters from an area on the target surface near the specular reflection point.

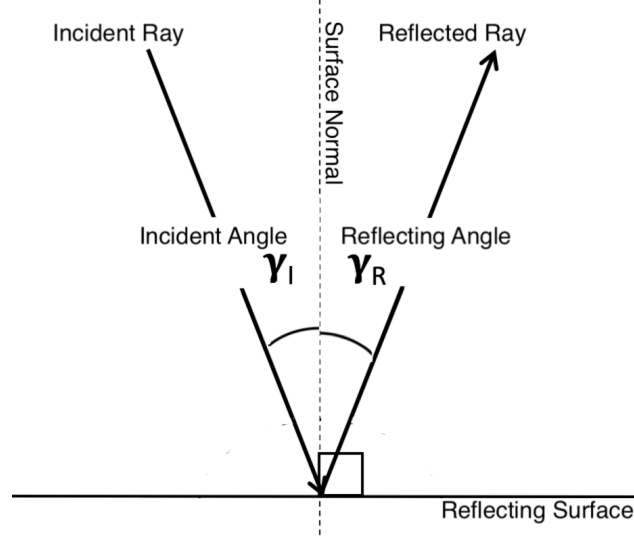


Figure 2.2: Specular reflection geometry. A specular reflection takes the shortest path from transmitter, to target, to receiver and has equal incident and reflecting angles with respect to the target surface normal. That is  $\gamma_R = \gamma_I$ .

A bistatic radar receiver sees signal power reflected from an area around the specular point on the target surface, in addition to the specular reflection ray itself. The reflecting area is called the glistening zone. The size of this contributing area is determined by the target surface roughness, the receiver height above the surface, and the incidence angle. The glistening zone on a smooth surface will be relatively small while a rough surface will produce a large glistening zone.

Surface roughness can be characterized by the distribution of surface heights or the horizontal correlation length [Elfouhaily and Johnson, 2007]. Roughness in relation to the signal wavelength determines the extent to which an observed reflection is phase coherent. Smooth surfaces, like sea ice, will yield a strong, coherent reflection where the glistening zone is limited in extent. Coherent reflections (or the coherent component) occur within the first Fresnel zone. This is the area around the specular point where the differential path delay across the reflecting surface is less than half the signal wavelength,  $\lambda/2$ . Rough surfaces, like the wind roughened open ocean, produce primarily incoherent scattering where the glistening

zone is much larger. The observation footprint, in this case, will be limited by the receiver antenna footprint, the distribution of surface slopes, or some combination of both.

The coherently scattered power that is seen by a bistatic radar receiver can be described by the bistatic radar equation, (2.1) [Zavorotny and Voronovich, 2000]. Received power  $P_R$  depends on the Fresnel reflection coefficient  $V_F$ , transmitted power  $P_T$ , transmitter and receiver antenna gains  $G_T$  and  $G_R$ , and the bistatic range from the transmitter to surface to receiver  $R$ . The radar equation gives the received signal power as,

$$P_R = \frac{P_T G_T G_R \lambda^2 V_F}{(4 \pi)^3 R^2}. \quad (2.1)$$

This model is suitable for coherent reflections from smooth surfaces, such as sea ice, where the scattering coefficient can be assumed constant over the relatively small contributing area. To model the return from a rough surface, equation (2.1) can be extended to consider a variable radar cross section as in (2.2). Now the glistening zone is expanded, and thus the reflection can no longer be considered as a point source. One must consider that the radar cross-section becomes,  $\sigma^0(\vec{p})$ , where  $\vec{p}$  is vector of locations on the surface. To construct the received power, the radar cross-section, receiver antenna footprint, and bistatic ranges are integrated over the reflecting surface beyond the first Fresnel zone. The radar equation becomes [Voronovich and Zavorotny, 2018],

$$P_R = \frac{P_T G_T \lambda^2}{(4 \pi)^3 R_{TS}^2} \int_A \frac{G_R \sigma^0}{R_{RS}^2} d\vec{p}. \quad (2.2)$$

where  $G_R$ ,  $\sigma^0$ ,  $R_{RS}$  and  $A$  are functions of  $\vec{p}$  integrated over the glistening zone. Note that in diffuse scattering, the range loss term becomes  $R_{TS}^2 R_{RS}^2$ , where  $R_{TS}$  and  $R_{RS}$  are the geometric ranges from transmitter and receiver to the surface, respectively. In (2.2), the transmitter to surface ranges, transmitted power and transmitter antenna gain are approximated as constants over the entire reflecting surface. This approximation is valid due to the large range between the GNSS transmitter and the reflecting surface, and its broad

transmitting antenna pattern. Receiver ranges to the surface and the receiving antenna pattern are not assumed to be constant as they are much closer. The increased path loss from  $(R_{TS}^2 R_{RS}^2)$  is partially offset by the increased contributing area of the glistening zone resulting in measurable reflections. Figure 2.3 illustrates the GNSS-R bistatic geometry and the extent of the glistening zone shown with iso-delay and iso-Doppler contours.

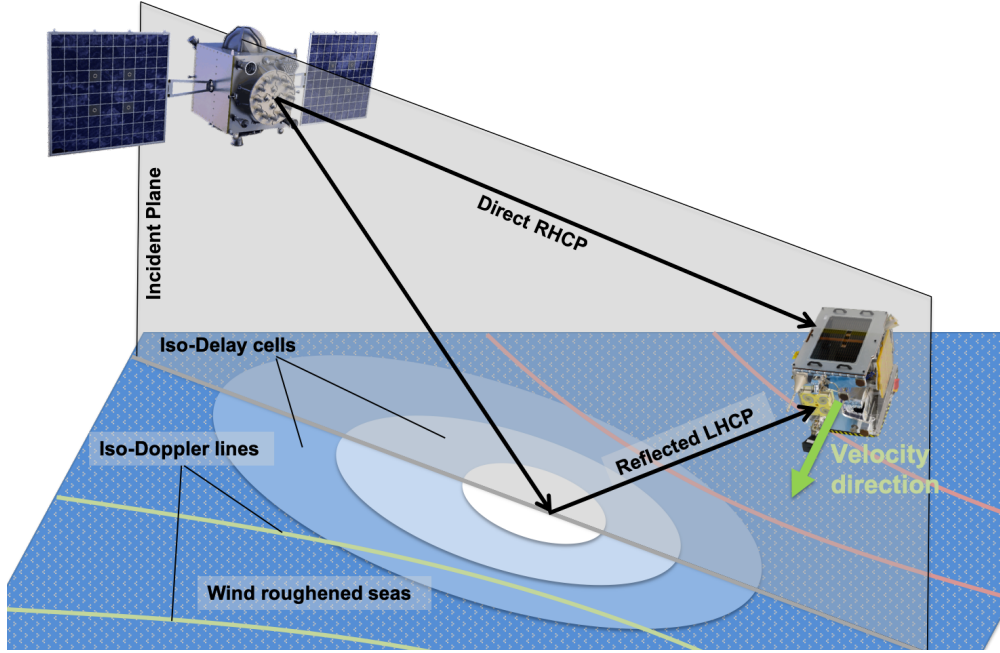


Figure 2.3: The GNSS-R glistening zone is divided into delay and Doppler bins. The radar cross section over the glistening zone is sampled by the GNSS-R receiver in delay-Doppler space. Elliptical equi-delay contours and hyperbolic equi-Doppler contours subdivide the surface into discrete contributions.

To observe the reflected signals, the GNSS-R receiver performs a cross-correlation operation between the incident signal and a locally generated replica of the GNSS pseudorandom noise (PRN) code. The cross-correlation operation is similar to the standard tracking process for direct signals, but deliberately shifted in delay and frequency to match the reflection. The actual observable from GNSS-R is then the resulting correlation function sampled over a range of delay and Doppler shifts, the delay-Doppler map (DDM) [Garrison and Katzberg, 1997]. Including the delay and Doppler filter terms in the radar equation (2.2) gives a model

for the GNSS-R DDM. The DDM model,

$$\langle |Y(\delta, f_D)|^2 \rangle = \frac{P_T G_T \lambda^2 T_i^2}{(4\pi)^3 R_{TS}^2} \int_A \frac{G_R \sigma_0}{R_{RS}^2} X^2(\delta, f_D) d\vec{p}, \quad (2.3)$$

is a function of delay ( $\delta$ ), Doppler shift ( $f_D$ ), and the surface characteristics [Zavorotny and Voronovich, 2000]. The two-dimensional Woodward Ambiguity Function (WAF),  $X^2$ , accounts for the delay and Doppler selectivity of the GNSS-R radar. The WAF in GNSS-R is the two-dimensional GNSS auto-correlation function.

The GNSS-R DDM is the observable from which geophysical parameters are retrieved. A DDM is essentially a measure of the bistatic-radar cross-section, weighted by the receiving antenna gain projection, and mapped into delay-Doppler space. The GNSS-R instrument observes the reflection scene in this delay-Doppler space. Figure 2.4(a) illustrates a simulated DDM from a wind-roughened ocean reflection based on the model in (2.3). Figure 2.4(b) shows the top-down view of the corresponding glistering zone area divided into relative delay and Doppler bins with respect to the specular point.

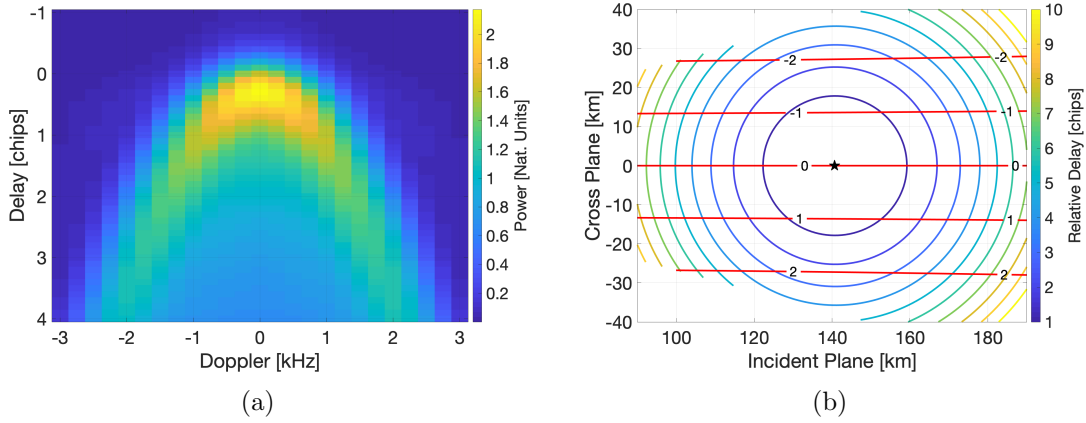


Figure 2.4: An example delay-Doppler map (DDM) and glistering zone map. (a) A DDM model generated by the method presented in Voronovich and Zavorotny [2018]. This model represents a perfectly clean observation with no sample noise. (b) The reflected power from the glistering zone is sub-divided into delay (colored contours) and Doppler (red contours shown in 1 kHz increments) bins. The reflected power is sampled in delay and Doppler space by the GNSS-R receiver to produce a DDM. The specular point in the glistering zone is marked with a black star.

On the reflecting surface, lines of equal delay form ellipses and lines of equal Doppler form hyperbola. The delay-Doppler samples of the DDM do not correspond to unique points on the surface, except along the ambiguity-free line. The ambiguity-free line follows where iso-Doppler contours are tangent to iso-delay contours on the surface corresponding to the horseshoe ridge of the DDM. Figure 2.5 shows how, in most cases, two points on the reflecting surface contribute to the same DDM pixel. Along the ambiguity-free line areas contribute unambiguously. Gradients of the receiving antenna gain pattern projection across the surface are also seen to preferentially weight contributions from certain areas. The differential antenna gain over the surface causes the Doppler asymmetry in the DDM. In Figure 2.5, the DDMs have more power in negative Doppler bins than in positive Doppler bins due to the orientation of the receiving antenna pattern.

## 2.2 GNSS-R Receiver Operations

The signal processing required to track a reflected GNSS signal builds upon the standard direct signal tracking methods. An incident signal is cross-correlated with a locally-generated PRN replica at the appropriate delay and frequency shift for direct signal tracking. Reflected signals however, are attenuated and shifted in delay and Doppler according to the relative geometry of the surface and incidence angles. Tracking a reflected signal is thus done with a so called open-loop configuration. The open-loop tracking is driven by estimates of the receiver, transmitter, and reflection positions and velocities to determine the appropriate delay and Doppler offsets. These inputs are taken from an onboard GNSS navigation solution and an Earth model to geo-locate a prediction of the reflection point [Jales, 2016; Masters, 2004; Wu et al., 1997]. Figure 2.6 shows a block diagram of the typical GNSS-R receiver structure. The open-loop delay-Doppler prediction model is used to purposely shift a bank of correlators with the local PRN replica to sample the incident reflected signal.

Both hardware and software-based GNSS-R receiver architectures have been successfully implemented [Lowe et al., 2002c; Unwin et al., 2011]. Hardware based receivers have

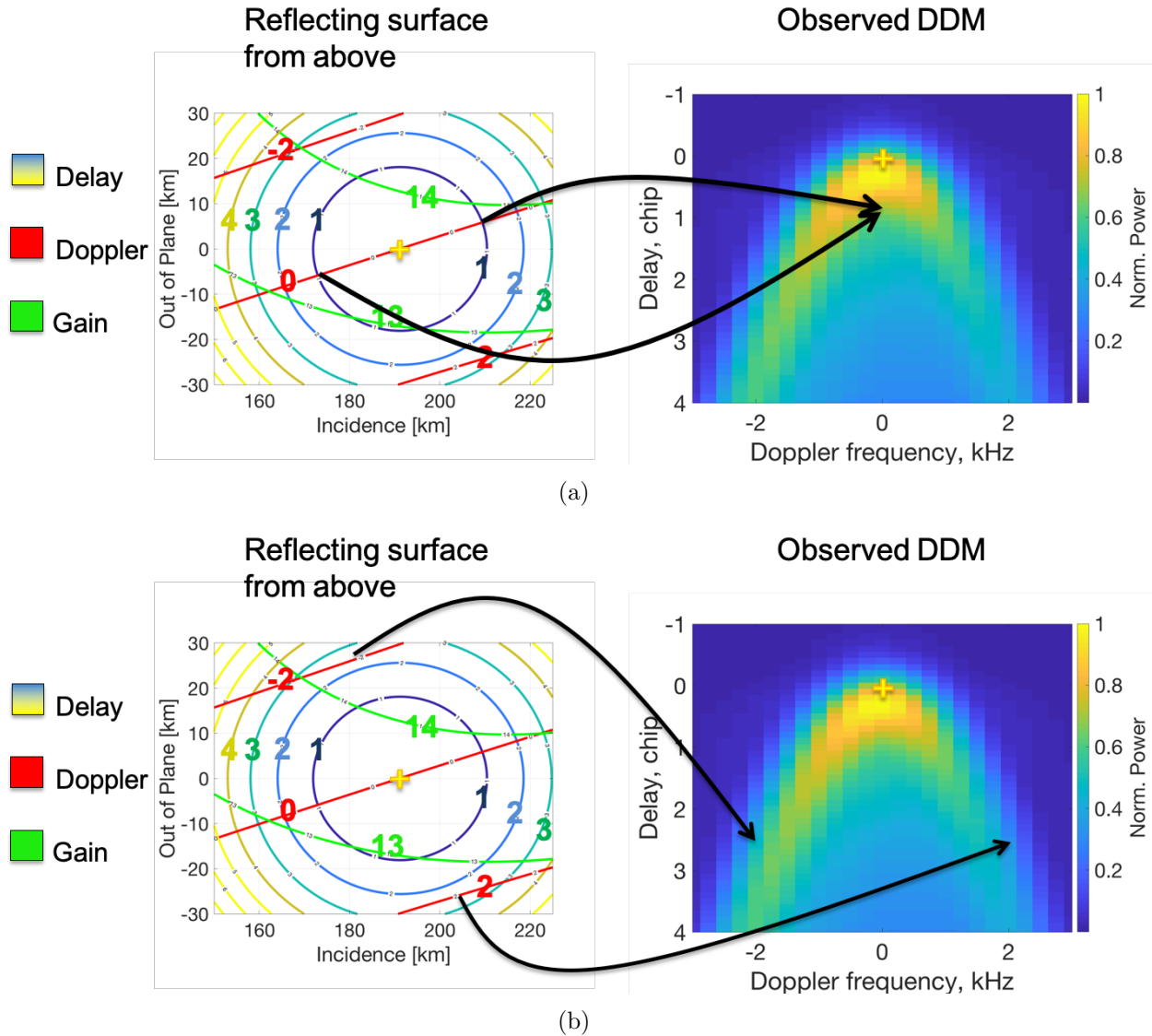


Figure 2.5: Illustration of mapping from the glistening zone to delay-Doppler space. (a) Two reflecting areas on the surface can contribute to the same DDM pixel. (b) An ambiguity-free line is found where delay contours are tangent to Doppler contours on the surface or along the DDM horse-shoe ridge. Gradients in the receiving antenna pattern cause asymmetry in the DDM.

been more practical for real-time operation, especially for spaceborne experiments. Software defined receivers offer more flexibility as the radio signal is digitally sampled in real time, allowing the signal processing to be completed onboard or reprocessed on the ground. When processing onboard, the downlink data is equivalent with both architectures. The most sig-



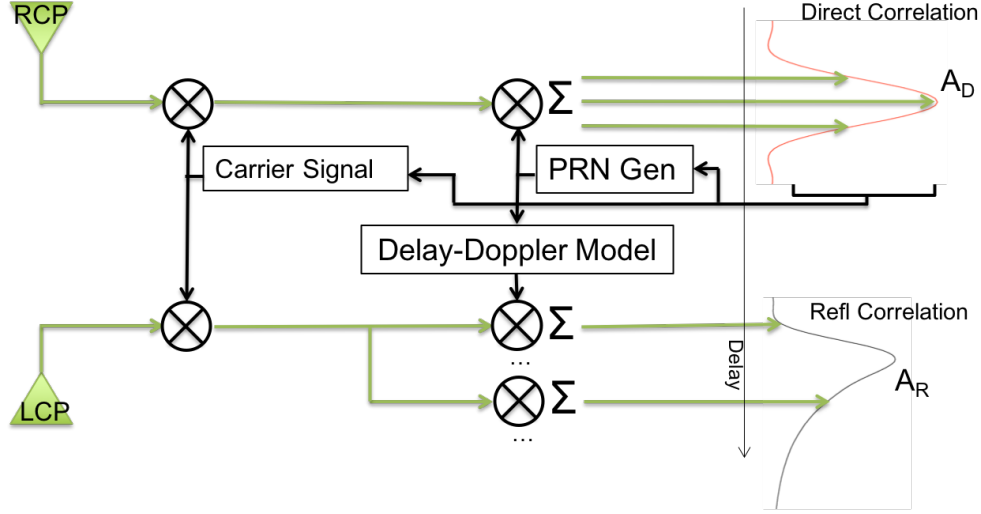


Figure 2.6: Block diagram of a typical GNSS-R receiver. Direct and reflected incident signals are down-converted to baseband and cross-correlated with a PRN code model. In the reflected channel, that PRN code model is shifted in delay and Doppler space according to a forward geometric prediction algorithm to sample the incident signal. Block diagram based on illustrations in Garrison et al. [2002].

nificant drawback to a sampling data recorder are the very large data records generated over short times, when sampling the RF signal. Data from both implementations have been used in this work [Mashburn et al., 2016, 2018].

Regardless of receiver architecture, the reflection point must be geo-located to complete the open-loop tracking process. This step requires knowledge of the receiver and transmitter positions and velocities, which can easily be taken from the standard navigation solution processing of the direct signals. A model of the reflecting surface must also be selected. Common choices are an ellipsoid Earth model, like the WGS84 reference ellipsoid, or a geoid model like the DTU13 [Andersen et al., 2015]. Precisely locating the reflection point on one of these surfaces is an iterative process [Masters, 2004; Wu et al., 1997], but closed-form approximations exist that are more suitable for real-time onboard operation [Jales, 2016].

The received power is recorded as a function of delay and Doppler after the cross-correlation operation as illustrated on the far right of Figure 2.6. Each cross-correlation

operation is performed on a limited time series of the sampled RF data. In the data sets used here, correlation is done with 1 ms of data in both in-phase and quadrature channels. The length of this coherent integration is limited primarily by the dynamics of the receiver motion relative to the reflecting surface and the GPS navigation message bit rate.

An incoherent summation of sequential coherent blocks is used to increase signal-to-noise ratio of the observations. The coherent in-phase and quadrature channels are squared and summed to form the incoherent integration. Incoherent integrations of 1 sec or more are recommended to provide sufficient time to average out the effects of speckle noise and yield a strong return [Zuffada and Zavorotny, 2001].

Once the GNSS-R DDM is obtained, the delay offset, amplitude, and shape of the correlation function can be related to geophysical parameters that describe the reflecting surface. The specular reflection delay is the primary observation metric utilized in this work for ocean altimetry. The construction of the specular delay measurement and its use to retrieve surface heights are discussed in Chapter 6. In Chapter 8 correlation power and shape are used as metrics to describe reflection coherence and surface conditions, allowing distinction between ice and water reflections.

## 2.3 Brief Review of GNSS-R Ocean and Sea Ice Remote Sensing

Martin-Neira [1993] proposed the first implementation of the GNSS-R concept, the Passive Reflectometry and Interferometry System (PARIS), to measure ocean surface height. Since 1993, the development of GNSS-R techniques have followed two primary paths. First are those based on the *conventional* design, and second, the *interferometric* design. Each refers to the fundamental operation of the GNSS-R receiver based either on correlation of an incident reflection with a locally generated GNSS signal model (conventional), or with the incident line-of-sight GNSS signal (interferometric). Both designs have shown merit and spawned development of GNSS-R techniques and research into a variety of remote sensing applications.

Interferometric measurements can be made from ground-based instruments with a single receiving antenna, or from air and space-borne instruments with two antennas for separate direct and reflected channels. Single antenna systems measure interference with the direct signal, caused by multipath that originates from the surrounding environment. Characteristics of that interference can be used to estimate a range of surface properties such as the height of the receiving antenna above the reflecting surface, or the soil moisture concentration near the monument. Larson et al. [2008a,b, 2013], Chew et al. [2016], and others have introduced methods for observing tides, snow depth, soil moisture and more from ground-based platforms. Camps et al. [2017], Fabra et al. [2012], Rius et al. [2010], Semmling et al. [2012, 2013, 2014, 2016], and others have taken the interferometric concept to the air with the two-antenna design and have demonstrated altimetry over rivers, lakes, and the ocean.

The work presented in this dissertation makes use of the conventional GNSS-R design. Zavorotny and Voronovich [2000, 1999] and Garrison and Katzberg [2000] first developed the theoretical scattering models for the conventional concept with GPS which predict the signal scattering of GNSS transmissions from ocean surfaces. The Zavorotny and Voronovich model is covered in Chapter 5. These models pioneered the investigation into the sensitivity of GNSS-R to wind-driven ocean surface roughness [Garrison et al., 1998; Zavorotny and Voronovich, 1999]. Conventional GNSS-R has also been used to study land, snow, and ice surfaces in recent years. Masters [2004] first demonstrated the sensitivity to soil moisture from aircraft and tower based measurements. Lowe et al. [2002a] demonstrated the first clear observation of an ocean reflected GPS signal from space in 2002 with data from SIR-C. Komjathy et al. [2000], Gleason [2006], Belmonte-Rivas [2007], and others [Alonso-Arroyo et al., 2016; Fabra et al., 2012] demonstrated that GPS-R can also be used to detect and classify sea ice.

More specifically for altimetry, sea surface heights were first experimentally retrieved by Lowe et al. [2002b]. Theoretical developments describing GNSS-R altimetry were presented by Zuffada and Zavorotny [2001], and Hajj and Zuffada [2003]. Both code and phase tracking

methodologies for altimetry have since been demonstrated primarily from low flying aircraft [Cardellach et al., 2014; Mashburn et al., 2016; Semmling et al., 2013]. The UK-DMC [Unwin et al., 2003], and TechDemoSat-1 [Jales and Unwin, 2015] missions provided the community with space-based data allowing larger scale analyses of GNSS-R altimetry [Clarizia et al., 2016; Mashburn et al., 2018], despite these missions not being optimized for the altimetry application. Simulation work has also been done to demonstrate the potential performance of an optimized GNSS-R altimetry constellation [Li et al., 2016; Park et al., 2017].

## 2.4 GNSS-R Space Missions

Lowe et al. [2002a] demonstrated the first clear observation of an ocean reflected GPS signal from space in 2002 with data from the Space-borne Imaging Radar (SIR-C). With this demonstration, the possibility of spaceborne GNSS-R constellations was opened. Since then, several missions have been flown to demonstrate the technology and perform science retrievals.

The first space mission with an instrument dedicated to GNSS-R was a technology demonstration flown onboard the UK-DMC spacecraft launched in 2003 [Unwin et al., 2003]. Gleason [2006], and Unwin et al. [2003] were among the first to utilize the UK-DMC GNSS-R data to demonstrate sensitivity to ocean surface roughness and sea ice from space.

Following the success of UK-DMC, Surrey Satellite Technologies Ltd. began development of the GNSS-R instrument flown on TechDemoSat-1 (TDS-1) in 2014 - the SGR-ReSI [Jales and Unwin, 2015; Unwin et al., 2010]. The SGR-ReSI is the first space-borne GNSS-R instrument to generate the DDM onboard in real time. Today, TDS-1 is still operating and collecting GNSS-R data. Flying in a high-inclination, sun-synchronous orbit, TDS-1 has been a valuable resource for the advancement of many GNSS-R applications across many surface types.

The Cyclone GNSS (CYGNSS) mission is the first GNSS-R science mission made up of a constellation of eight spacecraft launched in 2016. CYGNSS also carries the SGR-ReSI

instrument [Ruf et al., 2016]. The primary mission of CYGNSS is to measure ocean surface wind speeds inside of tropical cyclones. The constellation of small satellites orbit at a low inclination ( $\sim 35$  deg) to cover the tropical latitudes, providing dense global coverage within 24 hours.

Other GNSS-R missions, like <sup>3</sup>CAT-2 [Carreno-Luengo et al., 2016], PARIS-IOD [Martin-Neira et al., 2011], and GEROS-ISS [Wickert et al., 2016], have been proposed in recent years. These proposals boast dual-frequency, GPS P(Y) and C/A code tracking, precise orbit determination, and high gain receiving antenna capabilities. Each promises an opportunity to improve the performance and dramatically expand the field of GNSS-R for ocean, land, and ice applications.

## Chapter 3

### An Assessment of the Precision and Accuracy of Altimetry Retrievals for a Monterey Bay GNSS-R Experiment

Journal version<sup>1 2</sup> :

[Mashburn et al., 2016] J. Mashburn, P. Axelrad, S. T. Lowe, and K. M. Larson. An Assessment of the Precision and Accuracy of Altimetry Retrievals for a Monterey Bay GNSS-R Experiment. IEEE Journal of Selected Topics in Applied Earth Observations and Remote Sensing, 9(10):4660–4668, Oct. 2016. doi:10.1109/JSTARS.2016.2537698

#### Abstract

Global Navigation Satellite Systems provide signals of opportunity for bi-static radar remote sensing, called GNSS reflectometry (GNSS-R), that have potential to be used for ocean altimetry. These signals have advantages over traditional mono-static radar that include reduced cost, high density of measurements in time and space, and an inherent reference to a highly accurate time-space frame. Here we examine GNSS-R data collected from an aircraft flying over Monterey Bay, California. A downward-looking dual-frequency left-hand circularly polarized patch antenna recorded reflected signals. An upward-looking commercial antenna recorded the direct signals. Dual frequency carrier phase data from this antenna were also used to produce precise coordinates for the aircraft. The L1 P-code GPS

---

<sup>1</sup> Some formatting changes have been made to accommodate different citation and print styles.

<sup>2</sup> The re-tracking method referred to here as HALF was renamed P70 after this publication was printed.

data were collected over four days with two flights per day and consist of nine transects covering a  $1 \text{ deg} \times 1 \text{ deg}$  grid.

The performance of three timing retrieval algorithms has been evaluated based on measurement precision. From the observed cross-correlation waveform, the specular reflection timing was derived from the delay of the 70% peak correlation power (HALF method), the waveform leading edge peak first derivative (DER method), or the delay associated with a best fit function approximating the nominal waveform shape (PARA3 method). It was found the HALF method produced the most precise measurements for a 5 second integration time with a standard deviation of  $\sigma = 0.6$  meters.

The measurement accuracy is characterized by comparison with well established models including neutral atmospheric delay, mean sea surface height, and ocean and solid Earth tides. Biases on the order of  $1 - 4$  meters are observed with respect to a modeled mean sea surface and between each flight. However, the measurements are shown to track changes in sea surface height along the ground track to within 0.6 meters.

### 3.1 Introduction

The transmissions from satellites of Global Navigation Satellite Systems (GNSS) represent signals of opportunity for passive bi-static radar remote sensing. The use of these signals and their reflections for remote sensing is commonly called GNSS Reflectometry (GNSS-R). Measurements of sea surface height, sea ice state, and soil moisture fluctuations using these signals have been explored from various static and dynamic platforms [Fabra et al., 2012; Larson et al., 2008b; Lowe et al., 2000]. Specifically for sea surface altimetry, GNSS-R offers several advantages over mono-static radar systems including reduced cost, multiple measurements over a large area, and an inherent reference to a highly accurate time-space frame. Disadvantages relate to the fact that GNSS signals are not optimized for remote sensing applications and thus have limited bandwidth, lower signal power and therefore lower altimetric precision compared to active altimeters.

The application of GNSS-R or sea surface altimetry has been demonstrated from airborne platforms in several campaigns [Cardellach et al., 2014; Carreno-Luengo et al., 2013; Lowe et al., 2000; Masters et al., 2001; Semmling et al., 2013, 2014]. The precision of the GNSS-R measurements is heavily dependent on signal to noise ratio, the specular timing retrieval from the reflected waveform, and several other variables. The measurement accuracy is limited by uncalibrated instrument biases and errors in propagation models. To date, a few timing algorithms have been investigated and their precision characterized [Cardellach et al., 2014; D’Addio et al., 2011; Lowe et al., 2002b; Semmling et al., 2013] though altimetric accuracy of code based measurements has not been sufficiently explored. Carrier phase observations have been used in some cases to produce precise and accurate results [Semmling et al., 2013, 2014]. Code based measurements have thus far resulted in either imprecise or biased height retrievals [Carreno-Luengo et al., 2013].

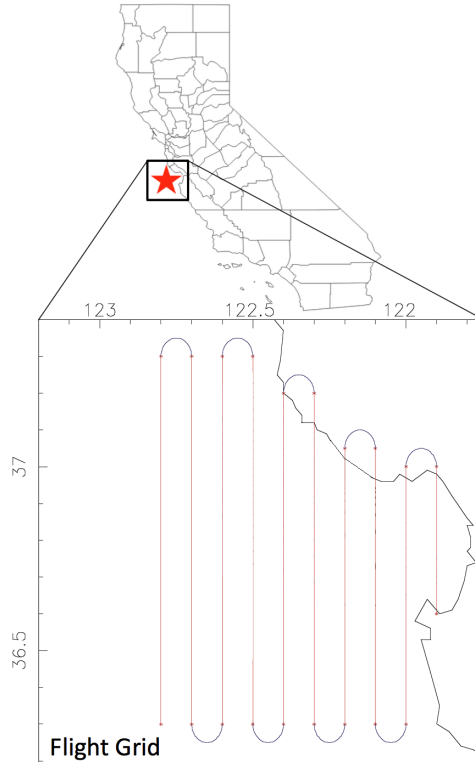


Figure 3.1: Planned flight pattern over Monterey Bay, California, USA.



This paper further investigates these issues based on an airborne experiment conducted in Monterey Bay, California. We first compare the measurement precision of three timing algorithms, similar in aim to Cardellach et al. [2014], to explore the sensitivity of certain points along the correlation waveform and establish a performance baseline for a new method. Then we examine the altimetry measurement accuracy through the implementation of models and altimetric error corrections that rely on scenario geometry, mean and time variant topography, and atmospheric conditions as described by accepted models.

### **3.2 Experimental Campaign and Data Set**

The following sections provide a description of the 2003 Monterey Bay data collection campaign, the GNSS-R instrument, and an overview of the data set obtained.

#### **3.2.1 Data Collection Campaign**

In August of 2003 a Cessna 310 was chartered to fly over Monterey Bay along the coast of California. A North-South oriented flight pattern at 0.1 deg longitude intervals was executed as seen in Fig. 3.1. The pattern extends nearly 1 deg in latitude and longitude and reaches over 60 km from the coastline at its South-West corner. This pattern was flown at a speed of about 90 m/s and an altitude of approximately 3 km. Two flights were conducted each day for several days with one in the morning and a second in the afternoon both lasting about 4 hours. The data examined here were taken from flights completed on the afternoon of August 13 and morning and afternoon of August 15, August 18, and August 19, 2003. The flight on August 13 is denoted as MB4 PM, flights on August 15 as MB5 AM/PM, August 18 as MB6 AM/PM, and August 19 as MB7 AM/PM.

#### **3.2.2 GNSS-R Instrument**

A conventional GPS receiver and a delay/Doppler mapping receiver designed by JPL were used to perform this experiment [Lowe et al., 2002c]. The delay/Doppler mapping

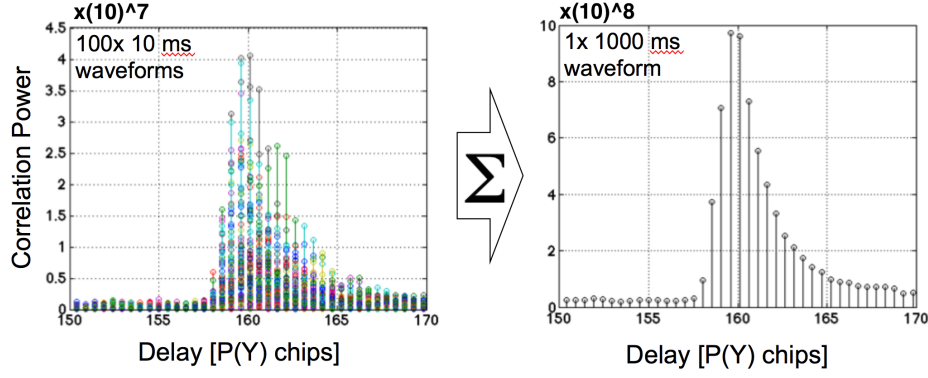


Figure 3.2: A one-second incoherently integrated waveform is created by summing one hundred, 10 ms coherently integrated waveforms.

receiver included a data recorder on the flight and a separate software defined receiver for post processing. The software receiver employs a clean replica method where a direct signal is tracked and used to drive a replica PRN code that is correlated with the reflected signal. To analyze P(Y) code signals without resorting to codeless or cross-correlating techniques, the replica codes were obtained after the fact and the correlations were done in post processing. The data recorder supports two input channels connected to up-looking and down-looking antennas of right and left handed circular polarization, respectively. These were small patch type antennas with peak gain near 3 dBi. The software receiver was capable of extracting C/A code and P(Y) code waveforms on both L1 and L2 frequencies. For the Monterey Bay experiments the digitally sampled L1 P(Y) signals were correlated and coherently integrated for 10 ms at lags spaced 50 ns apart. A series of 10 ms integrated waveforms were then summed to produce each incoherently integrated waveform as illustrated in Fig. 3.2. It was with these incoherently integrated waveforms that timing measurements were taken.

### 3.2.3 Data Set

GPS-R measurements on the L1 frequency and conventional GPS receiver measurements were recorded on board the aircraft platform. At any given time within the data set, as many as four GPS transmitters visible above 45 deg elevation produce strong reflections.

Each flight yielded nearly continuous 20 MHz sampling on both  $I$  and  $Q$  channels producing a large data set. A carrier-phase based point solution was computed for the aircraft position with the NASA JPL GIPSY-OASIS 2 (GOA-2) software. The receiver position solution has an estimated precision of 0.3 meters [Bruce Haines, personal communication, 1/18/2016].

Concurrent data from **in situ** buoys measuring wind speed, atmospheric pressure, temperature, and humidity are available from the NOAA National Data Buoy Center [NOAA, 2015] to be used in the delay model described later. Unfortunately, measurements of the aircraft attitude and atmospheric conditions aloft were not recorded during the experiment. Thus, for this analysis the aircraft attitude has been assumed constant when flying straight and level and data from turns are not considered. Atmospheric conditions are taken from the NOAA NCEP Reanalysis data provided by the NOAA/OAR/ESRL PSD, Boulder, Colorado, USA [Mesinger et al., 2006].

### 3.3 Methodology

The algorithms and models used in this research are now described. First, the tracking methods used to characterize precision are presented, followed by the components of the delay model used to characterize the accuracy.

#### 3.3.1 Specular Delay Tracking Algorithms

Several specular timing retrieval algorithms were considered to estimate the time of arrival difference between direct and reflected GPS signals. Each algorithm is applied to a series of waveforms that have been incoherently integrated for  $T_{in} = 0.5 - 10$  seconds. All three tracking methods model the waveforms with (3.1) which allows the band limited signals to be interpolated.

$$x(t) = \sum_{n=-\infty}^{\infty} x[n] \cdot \text{sinc}\left(\frac{t - nT}{T}\right) \quad (3.1)$$

Here  $x[n]$  represents the series of discrete correlation waveform samples,  $t$  is delay, and  $T$  is the sampling period set to be 0.5 P-code chips.

The datum from which the specular timing is measured in these algorithms is the direct signal time of arrival. This “zero” delay is taken to be at the direct signal waveform peak. The true waveform peak is found via interpolation which has the benefit of estimating and removing any DLL tracking errors.

#### **3.3.1.1 HALF**

The HALF method has been derived from traditional mono-static radar techniques taking the specular reflection delay at a given fraction of the peak correlation power [Cardellach et al., 2014; Masters et al., 2001]. Here the specular point is assumed to lie at the 70% peak power delay. This point was chosen based on the findings of Cardellach et al. [2014] that showed tracking the 70% point is similar to the theoretically ideal peak derivative point. The HALF delay is found by using a Newton’s method iteration scheme.

#### **3.3.1.2 DER**

The second algorithm, the DER method, derives the specular delay from the maximum first derivative on the waveform leading edge, as would be for the ideal case [Hajj and Zuffada, 2003]. The waveform derivative is calculated numerically as a function of delay and the location of the maximum is found by a golden section search method [Heath, 1996]. As with the HALF method, the timing of the direct signal waveform peak is found by a DLL allowing the difference in time of arrival to be computed.

#### **3.3.1.3 PARA3**

The third algorithm, a three parameter function fitting method, proposes a new empirical waveform model. The model of the GPS-R waveform is created through the convolution of a simulated squared, band limited auto-correlation function and the function  $f(t | \tau, A, \alpha)$

given by (3.2). The function  $f(t | \tau, A, \alpha)$  is a representation of the correlation waveform in the case of infinite bandwidth and chipping rate. The specular reflection takes the shortest possible reflection path to arrive at time  $\tau$  where the signal return instantaneously rises to amplitude  $A$  and decays exponentially in delay with decay rate  $\alpha$ . Fig. 3.3 illustrates the auto-correlation function,  $f(t | \tau, A, \alpha)$ , and the resultant waveform model.

$$f(t | \tau, A, \alpha) = \begin{cases} 0 & t < \tau \\ A \cdot e^{-(t-\tau)/\alpha} & t \geq \tau \end{cases} \quad (3.2)$$

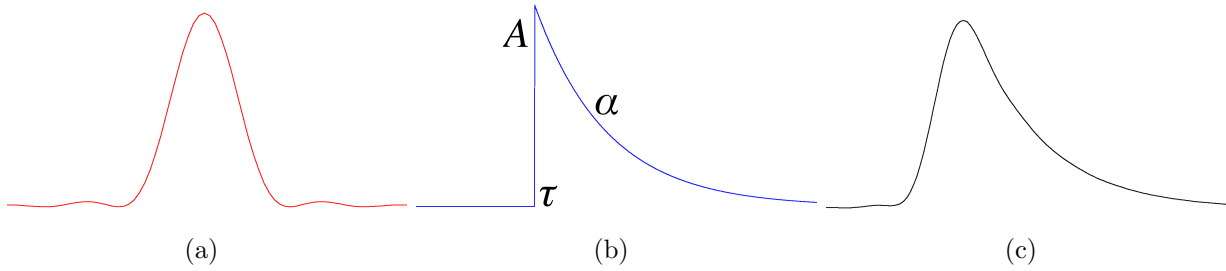


Figure 3.3: Components of the PARA3 waveform model. The (a) band limited auto-correlation function is convolved with (b) a three parameter function  $f(t | \tau, A, \alpha)$  to yield the (c) waveform model. The least squares best fit combination  $\tau^*$ ,  $A^*$ , and  $\alpha^*$  is found and  $\tau^*$  is taken as the specular reflection time delay.

The parameters  $\tau$ ,  $A$ , and  $\alpha$  are tuned to achieve a least squares best fit between the model and data. The best fit set of parameters is denoted with a star and  $\tau^*$  is taken to be the specular delay measurement. The problem of finding the least squares best fit model to the measured waveform is very non-linear with many local extrema in the parameter state space. A cost function equal to the sum of the squared residuals over the waveform from the peak delay - 2 code chips to the peak + 0.5 code chips is used to evaluate the fit of each model realization. Fitting over this range was found to produce the most precise timing measurements. The global minimum cost is found by first performing a coarse brute force search over a reasonable section of the state space. The coarse best fit solution becomes the initial condition to a steepest descent search that approaches the nearest minimum by following the steepest negative gradient.

It will be seen in Section 3.4 that the PARA3 algorithm did not perform as well as was hoped. Some potential improvements to this method are suggested in Section 3.5.

### **3.3.2 Delay Model**

A comprehensive model to predict the path delay of a reflected GPS signal as seen by an airborne receiver has been constructed and used to assess the precision and absolute accuracy of the Monterey Bay GPS-R measurements. Included are a reference surface, ocean tides, solid Earth tides, tropospheric delay, and the zenith-nadir antenna baseline. Missing from this model is the aircraft attitude as that data are not available.

#### **3.3.2.1 Reference Surface**

In order to predict the reflected signal path delay, a model of the reflecting surface and the relative receiver-transmitter geometry are taken into account. Here we include the capability to simulate specular reflections from either the WGS84 ellipsoid or the DTU13 mean sea surface [Andersen et al., 2015] with the option to superimpose ocean and solid Earth tide corrections. An iterative approach is used to find the specular reflection location on the surface [Wu et al., 1997] such that the incident and reflecting angles with respect to the surface normal are equal. The additional path delay of the reflected signal is found by subtracting the line of sight range from receiver to transmitter from the bistatic range.

#### **3.3.2.2 Ocean and Body Tides**

Ocean and solid Earth tide corrections may be superimposed onto the reference surface. Tidal corrections have been generated by the GOT4.8 model to cover the extent of the flight path over the experiment times [Richard Ray, personal communication, 2/8/2015]. The model is a summation of short period, long period, load, solid body, and pole tides. A 0.5 deg grid was evaluated at 10 minute intervals throughout the duration of the experiment. At a given location and point in time the modeled tide corrections are interpolated and imposed

upon the reference surface. In Monterey Bay the GOT4.8 model estimates the tides to be on the order of  $\pm 1$  meter.

### 3.3.2.3 Tropospheric Path Delay

The excess signal path delay due to the tropospheric effect is accounted for using the modified Saastamoinen model given by (3.3) with both “wet” and “dry” components [Hofmann Wellenhof et al., 1997]. Atmospheric pressure (P), temperature (T), and water vapor pressure (e) are taken from NOAA NCEP Reanalysis data. This modified version of the traditional Saastamoinen model accounts for the receiver altitude through correction terms B and R that depend on height and incidence angle.

$$\delta_T = \frac{0.002277}{\sin(\theta)} \left[ P + \left( \frac{1255}{T} + 0.05 \right) e - B \cdot \tan^2(\theta) \right] + R \quad (3.3)$$

### 3.3.2.4 Antenna Baseline

In the Monterey Bay experiments, the zenith pointed antenna was mounted on top of the aircraft fuselage while the nadir pointed antenna was mounted beneath the fuselage. Physical measurement of the installation indicated that the nadir pointed antenna was 10 cm left, 10 cm behind, and 125 cm below the zenith antenna in the aircraft body frame (starboard, forward, up). The location of the zenith looking antenna in the WGS84 frame is estimated in the aircraft position solution. The location of the nadir looking antenna in the WGS84 frame was found by transforming the known body frame vector into a local level frame (East-North-Up) with an assumed aircraft attitude and heading and then into the Earth fixed frame. When predicting the specular reflection delay from a model surface the WGS84 frame coordinates of the nadir pointed antenna are used as the receiving point.

Without knowledge of the true aircraft attitude a “straight and level” orientation was assumed (yaw, pitch, and roll are 0 deg). A model to estimate the delay effect of a baseline offset between zenith and nadir antennas is given in (3.4)

$$\delta_B = (\mathbf{R} \vec{b}) \cdot \hat{e} \quad (3.4)$$

where  $\delta_B$  is the delay effect,  $\vec{b}$  is the baseline vector in the body frame,  $\mathbf{R}$  is the rotation matrix to transform from the body frame to a local level frame via yaw, pitch, roll, and heading angles, and  $\hat{e}$  is the receiver-transmitter line of sight unit vector in the local level frame. It can be seen that the delay effect depends on the projection of the baseline vector onto the line of sight direction.

### 3.3.3 Surface Height Retrieval

To retrieve surface height from the bistatic delay measurement the specular delay can be approximately related to the receiver height by (3.5).

$$\delta^m \approx 2 \cdot h_{RX} \cdot \sin(\theta) \quad (3.5)$$

Here  $\delta^m$  is the measured specular delay in units of length,  $h_{RX}$  is the receiver height, and  $\theta$  is the GPS elevation angle at the specular point. Since the receiver location is known in the WGS84 frame the reflecting surface can then be positioned in that same frame. However, this model assumes a locally flat Earth and therefore may be in error by several meters at a 3 km receiver altitude. Instead we compute an estimate of the surface height ( $h^{surf}$ ) relative to a reference surface by comparing measured and predicted path delays. The measured path delay ( $\delta^m$ ) is subtracted from the predicted delay ( $\delta_{REF}^p$ ), computed iteratively as described in Section 3.3.2 above, and scaled by twice the sine of the elevation angle ( $\theta$ ) as seen in (3.6). Using a differential delay between a measurement and prediction brings the problem into the linear regime where the flat Earth approximation may be used. The measured relative surface heights were then assembled into a map to illustrate the measured deviation from the chosen reference. In (3.6) either the WGS84 ellipsoid or the DTU13 model may be used as the reference.



$$h^{surf} = \frac{\delta_{REF}^p - \delta^m}{2 \cdot \sin(\theta)} \quad (3.6)$$

### 3.3.4 Measurement Precision Calculation

A series of altitude measurements from two passes over Monterey Bay were then used to assess the measurement precision. Measured receiver heights compared to the known aircraft heights above the WGS84 reference ellipsoid are shown in Fig. 3.4(a). Surface heights relative to the WGS84 ellipsoid were retrieved with (3.6) and are shown in Fig. 3.4(b). In this case the predicted delay was made to account for the WGS84 ellipsoid, troposphere delay, and the antenna baseline effects. The resulting measured surface height has a mean offset and a systematic slope and curvature. The solid red curve represents a least squares quadratic curve fit to emphasize the systematic effects. The quadratic fit was subtracted out to form zero mean, near white noise residuals, Fig. 3.4(c). A quadratic fit rather than a geoid model was used to avoid the influence of any model errors. The standard deviation of the residuals is computed and reported as the measurement precision. Average standard deviation values over two legs of the flight furthest from shore with three visible transmitters each and for several incoherent integration times are reported in Table 3.1. The precision was computed for each delay tracking algorithm. The best performing algorithm was used to then characterize accuracy.

## 3.4 Results

### 3.4.1 Precision

The metric by which performance of each timing algorithm has been graded is the standard deviation of the altitude measurement residuals. Table 3.1 shows the standard deviation of the residuals for each algorithm for various incoherent integration times. It can be seen that the HALF algorithm outperforms both PARA3 and DER in all cases. The

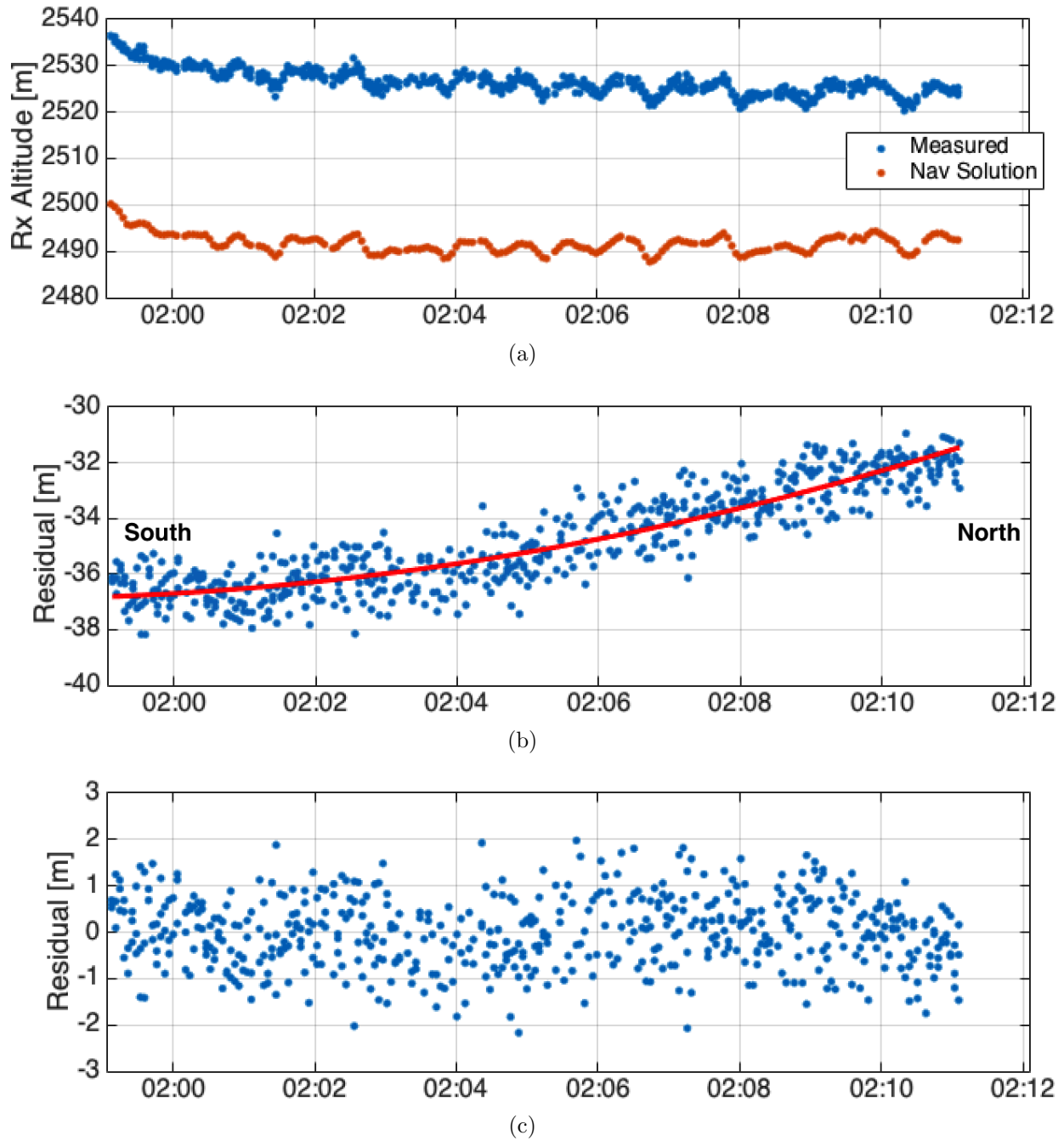


Figure 3.4: Measured aircraft heights and the residual from the ellipsoid height. (a) The measured aircraft heights show a persistent bias away from the WGS84 ellipsoidal heights derived from the aircraft navigation solution. This bias is consistent with the known mean sea surface in Monterey Bay. (b) The measured surface heights relative to the WGS84 ellipsoid show a bias and systematic slope and curvature. (c) Once the first and second order systematic trends are removed, the residuals are zero mean, near white noise.

PARA3 algorithm performs second best for integration times 0.5 sec, 1 sec, and 2 sec. This result indicates that the HALF algorithm is the most precise.

The HALF method outperforming DER is an expected result. First, the DER method is tied to a noisy measurement point. The correlation waveform samples have noise on them and therefore the derivative, which is being computed numerically, is expected to have even more noise. Second, the DER method tracks a rounded peak which is difficult to find precisely with numerical methods. In contrast, HALF tracks a zero crossing which is a more precise, well defined point.

It can be seen in Table 3.1 that the PARA3 algorithm does not perform as well as the other methods as the integration time is increased. The standard deviations from the HALF and DER methods decrease by a factor of  $\sqrt{T_{in}}$  as the integration time is increased. The PARA3 standard deviations do not. For example, there is a factor of four increase in integration time from 0.5 sec to 2 sec. It is expected that the standard deviation of the measurement residual would be reduced by a factor of two as the incoherent noise is averaged down. For the HALF and DER algorithms this is the case (HALF  $\sigma_{0.5s}/\sigma_{2s} = 1.9$  and DER  $\sigma_{0.5s}/\sigma_{2s} = 2.0$ ) but the PARA3  $\sigma$  values only reduce by a factor of 1.5.

Table 3.1: Standard deviation of altitude measurement residuals for each of the three timing algorithms over various incoherent integration times.

| $T_{in}[\text{s}]$ | <b>HALF</b> $\sigma$ [m] | <b>PARA3</b> $\sigma$ [m] | <b>DER</b> $\sigma$ [m] |
|--------------------|--------------------------|---------------------------|-------------------------|
| 0.5                | 1.7                      | 1.8                       | 2.8                     |
| 1                  | 1.2                      | 1.4                       | 2.0                     |
| 2                  | 0.9                      | 1.2                       | 1.3                     |
| 5                  | 0.6                      | 1.0                       | 0.9                     |
| 10                 | 0.5                      | 0.9                       | 0.7                     |

A chi squared ( $\chi^2$ ) test for goodness of fit has been performed to analyze the quality of the PARA3 waveform model fit. As an example the  $\chi^2$  per degree of freedom was calculated for each waveform in a set of 5 sec incoherently integrated waveforms (17 waveforms). If the model were in good agreement with the measured data, the  $\chi^2$  value would be near a

value of 1,  $\chi^2 \approx 1$ . In this case the  $\chi^2$  values range from 15 to 55 with a mean of  $\chi^2 = 34$  indicating poor agreement between the model and data.

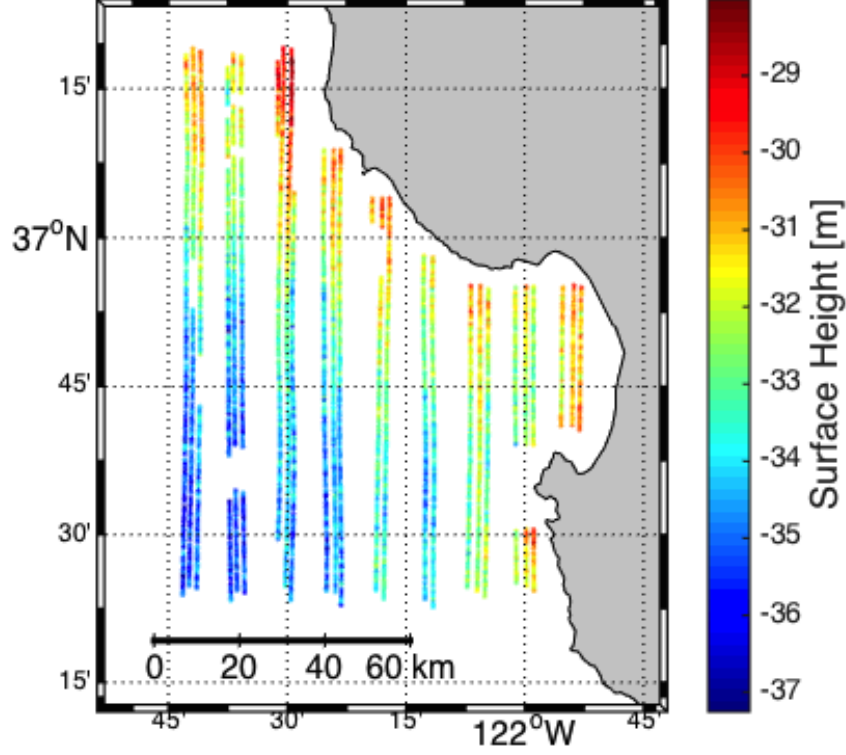


Figure 3.5: Surface height retrievals in Monterey Bay from 5 sec observations. Individual measurements of Monterey Bay surface as derived from 5s incoherently integrated waveforms recorded during the afternoon flight of August 13, 2003. Each height measurement has been corrected for tropospheric delays, tides, aircraft motion, and the antenna baseline.

Use of the direct signal correlation waveform instead of a simulated auto-correlation function may improve fitting in future work. It may be that there are scattering effects that are not being taken into account with this model. In the presence of ocean waves with sufficient height the instantaneous rise in the function  $f(t | \tau, A, \alpha)$  would more correctly have some finite slope as reflections from a wave crest arrive at the receiver earlier than those from a wave trough. Perhaps also the exponential decay of  $f(t | \tau, A, \alpha)$  with rate  $\alpha$  is not representative of the true scattering fall off.

Cardellach et al. [2014] presented a similar study where they compared the precision

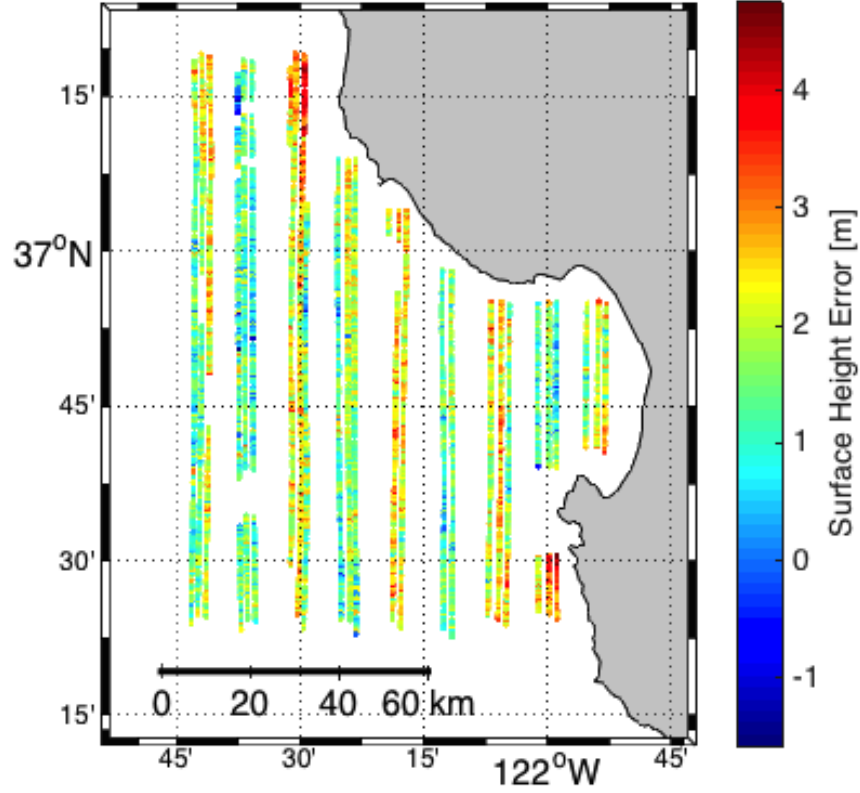


Figure 3.6: Height anomaly in Monterey Bay with 5 sec observations. The difference between each 5s integrated surface height measurement (Fig. 3.5) and the DTU13 mean sea surface model.

of three timing retrieval algorithms using GPS C/A code measurements. Their results, also obtained with the HALF and DER methods were better than those shown in Table 3.1. For example, Cardellach found that for an integration time of  $T_{in} = 10$  sec the DER method surface height measurement precision is  $\sigma = 0.36$  meters versus our  $\sigma = 0.7$  meters. At first this may seem counterintuitive, because our results were obtained using the P(Y) signal with ten times more bandwidth than their C/A code results. However, there are three factors that contribute to our signals being received at substantially lower signal to noise ratio (SNR) than Cardellach et al. [2014]. The GPS satellites transmit P(Y) modulated signals at 3dB lower power than C/A code modulated signals. Second, because of the higher chipping rate, the code-limited region on the ocean surface is smaller for P(Y) than C/A

code signals. Perhaps most importantly, the experiment described in Cardellach et al. [2014] used antennas with 15 dBi gain, whereas the small patch antennas used in the Monterey Bay experiments were no more than 3 dBi. The lower overall SNR in the experiment considered here, produces a corresponding degradation in tracking performance. While this affects the precision of the measurements and altimetry estimates obtained, it is not so severe as to preclude our analysis of the achievable accuracy.

### 3.4.2 Accuracy

In the assessment of the measurement accuracy, 5 sec incoherently averaged waveforms and the HALF timing algorithm were used. Corrected measured surface heights were compared against both the WGS84 ellipsoid and the DTU13 mean sea surface. Fig. 3.5 shows each measured surface height with respect to the WGS84 ellipsoid as retrieved from a 5 sec waveform observed during the afternoon flight of August 13, 2003, MB4 PM. Here the surface height measurements have been corrected for tropospheric delays, tides, aircraft motion, and the antenna baseline as described above. It can be seen that the surface is approximately 30 m below the ellipsoid and is sloping down into the South and West. From North to South the surface appears sloped downward by about 7 meters over 100 km (0.9 degrees latitude).

The measurements were also compared to the modeled delays predicted using the DTU13 mean sea surface. Fig. 3.6 illustrates this deviation between the measurements and the mean sea surface model. A positive error indicates that the measured surface is above the reference. It can be seen that there is a meter level positive bias. A similar bias is seen in the other flights as well. This bias is most likely the result of an uncalibrated instrument and the somewhat arbitrary tracking point used in the HALF timing algorithm. Aside from the over all bias, the estimates along the Northern and South-Eastern borders show the largest deviation from the DTU 13 reference surface. While these measurements are taken relatively close to land, they are limited to 2 km offshore to prevent contamination from land reflections. In these coastal areas the mean sea surface and tidal models are known to

be less accurate, but not at the level of the observed discrepancy. The mean sea surface and ocean tide models are quoted to be accurate at the 10 cm level in coastal regions [Stammer et al., 2014].

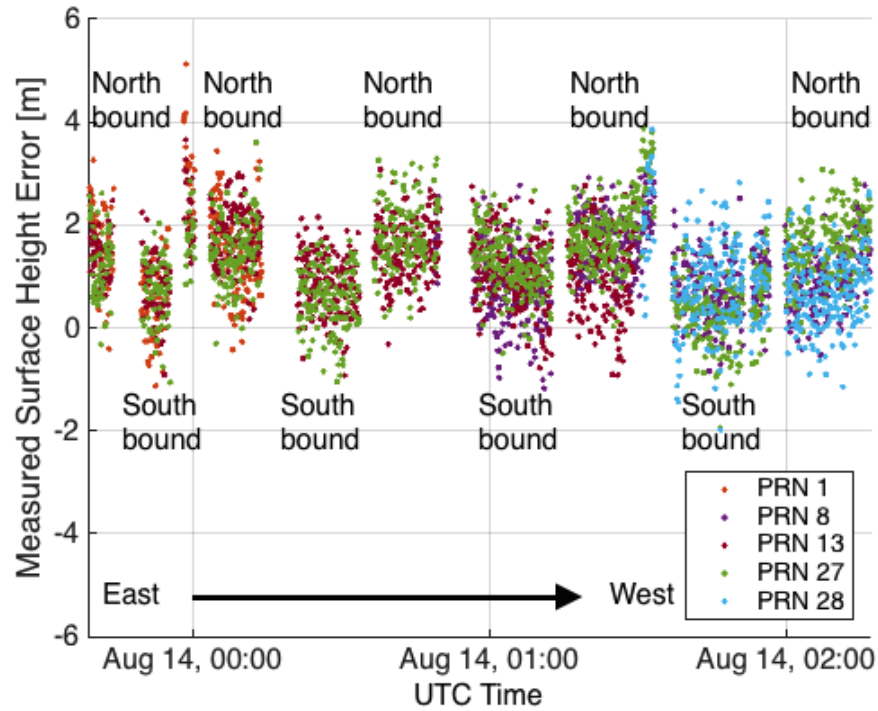


Figure 3.7: TMB4 height anomaly plotted against time. The difference between the measured surface retrieval and the DTU13 mean sea surface corrected for ocean and body tides plotted against time during the afternoon flight on August 13, 2003.

Looking closely at Fig. 3.6 a striped pattern that is oriented North-South along the flight transects can be observed. Alternating transects appear more red/yellow while those in between appear more blue/green. This pattern can be seen more clearly when the same data are plotted against time in Fig. 3.7. It can be seen that with respect to the DTU13 mean sea surface the measurements appear to oscillate up and down about a mean bias from one flight leg to the next. Measurements from all visible satellites follow the same pattern as the colored clouds of data corresponding to specific PRNs move together. It appears that this effect may be a function of the aircraft direction of travel (ie. North-bound or South-bound). Or there may be some dependence on transmitter azimuth with respect to

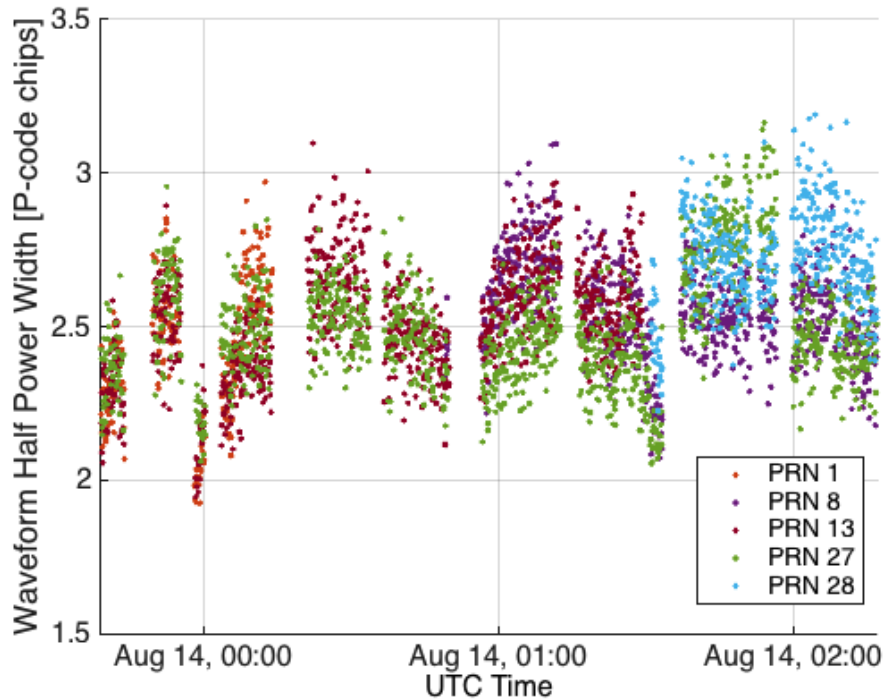


Figure 3.8: MB4 correlation waveform width plotted against time. Correlation waveform width measured at the 50% power point shown as a function of time during the afternoon flight on August 13, 2003, MB4 PM.

the aircraft body frame.

We considered the possibility that the level shift from one direction to the other could be due to an error related to the satellite azimuth, for example an antenna effect. It is known that the nadir pointed antenna gain pattern is skewed to the starboard direction resulting in stronger signal returns from starboard reflections. However, the fact that all of the measurements regardless of their azimuth exhibit similar behavior in Fig. 3.7 indicates that the measurement is insensitive to antenna gain differences.

Timing errors between the receiver location and delay measurements could also produce an effect similar to what is observed. We investigated this as well, and found that introducing a range of potential timing offsets significantly degraded the results by misaligning the actual aircraft height variations used in computing the predicted ranges from the corresponding measurements. Therefore, if a timing error were present the receiver motion would not be



canceled correctly and even larger systematic trends would be present.

The influence of aircraft attitude rotating the antenna baseline would give an effect that is dependent on the direction of travel but the baseline vector in this experiment is simply too small to produce the observed discrepancies between legs. If a reasonable 5 deg angle of attack is assumed, the delay effect associated with the baseline vector in a 180 deg turn is only 0.25 meters for a 55 deg GPS elevation angle. Mapped to height the effect becomes 0.15 meters, much smaller than the observed meter level jumps.

The sea surface oscillations that our retrievals seem to show are not consistent with accepted models of this region, and we can only assume at this point that they reflect remaining discrepancies. The model surface shows a relatively smooth, steady negative slope from North-East to South-West. In contrast the measured surface shows a rippled pattern oriented North to South on the surface. We speculate that these biases may be due in part to phase windup in the aircraft position solution, or there may be some aircraft speed dependence. It has been found that the aircraft persistently flew 10 – 15 m/s faster when traveling North-bound.

Another effect that can be seen in Fig. 3.7 is a slope in the height error as a function of latitude. In several flight transects the height error appears to be lower at the South than at the North. It has been found via **in situ** buoy measurements that the wind speed is different by several meters per second at the North and South ends of the flight grid [NOAA, 2015]. It is believed this has caused a difference in surface roughness from North to South and therefore a difference in the signal scattering. Rougher waters will yield more diffuse reflections and therefore alter the shape of the correlation waveform.

One can use the width of each correlation waveform at the 50% power point as a metric to see the roughness effect on waveform shape. Fig. 3.8 shows that the correlation waveforms are wider in the South and more narrow in the North as expected. As the wind is stronger in the South there is a rougher surface and therefore a more diffuse reflection and wider waveform. The HALF timing algorithm appears to be sensitive to this change in waveform

shape resulting in a timing bias. A roughness dependent timing error would produce the sloped effect seen in the height errors of Fig. 3.7.

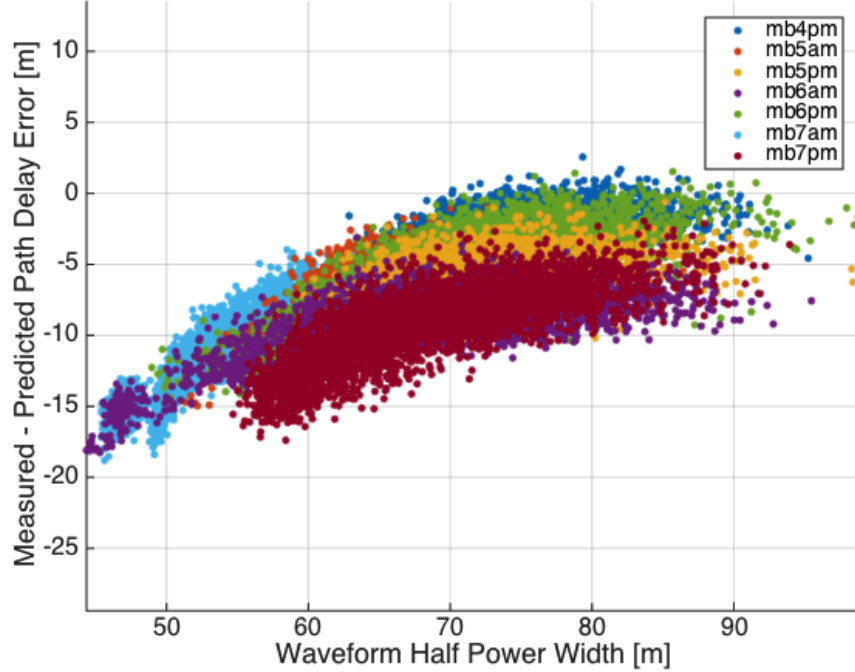


Figure 3.9: Monterey Bay delay anomaly plotted versus waveform width. Measured - predicted delay error versus correlation waveform width measured at the 50% power point. The dependence on waveform width illustrates the need for a roughness dependent delay tracking method.

Fig. 3.9 shows measured - predicted path delay error against waveform half power width for all of the flights studied here. There is an obvious dependence on width (believed to be a proxy for roughness) in the delay error. A remaining bias between flights prevents development of a width dependent empirical delay correction. For example flight MB7 PM is biased with respect to flight MB6 PM by about  $-5$  meters. The source of this inter-flight bias remains unknown. If the measured reflection is purely specular the observed waveform should be an attenuated and delayed version of the direct signal waveform, rather than a spread signal. The correct tracking point would be the waveform peak. For the given receiver bandwidth of this data set the mean delay offset between the HALF 70% tracking point and the waveform peak is about 15 meters as measured from the direct signal waveforms. In

Fig. 3.9 as the waveform width narrows, approaching a purely specular reflection, the delay error of the HALF tracking point approaches -15 meters. When the measured reflection has a strong diffuse component the true tracking point moves down the waveform leading edge approaching the maximum derivative tracking point (or similarly the HALF point). Fig. 3.9 illustrates this behavior as the waveform width is widened from 50 meters (largely specular) to 90 meters (largely diffuse) and the delay error approaches zero.

Results shown thus far in Fig. 3.5 - 3.8 are from the flight conducted on the afternoon of August 13, 2003, MB4 PM. The other flights can be described by the same patterns though there is a different meter level bias in the measured surface height between each of them that is attributed to instrument error and the HALF method measurement bias. Aside from the inter-flight biases, the structure of each measurement set is consistent. The North-bound to South-bound discrepancies are present and repeated in all flights and the topography measured along each flight leg is repeated between flights. For example three passes along the Westernmost leg (leg #9) can be compared from flights MB4 PM, MB5 AM, and MB5 PM. After applying all corrections, the measurements of each flight are biased from the DTU13 mean sea surface by 1 – 4 meters. Each flight has been shifted to align with the DTU13 model such that they have zero mean residuals. Doing this illustrates the measurement repeatability as seen in Fig. 3.10(a). Each flight has measured the same surface topography, the mean sea surface. To quantify the consistency in shape a single polynomial was fit to all three repeats of leg #9.

Each flight was compared to that polynomial individually. Plotted against latitude the residuals with respect to the polynomial appear flat, near zero mean, and near white noise, Fig. 3.10(b). Histograms shown in Fig. 3.10(c) illustrate the residual distribution which looks nearly Gaussian. A chi-squared test for goodness of fit reveals that the polynomial fit to all three passes at once is an excellent representation of each repeat individually and therefore quantitatively shows each flight yields a consistent form. The chi-squared per degree of freedom value is  $\chi^2 = 0.99$  for all flights over leg #9. Some systematic errors on

the order of 0.5 m with respect to the DTU13 mean sea surface remain.

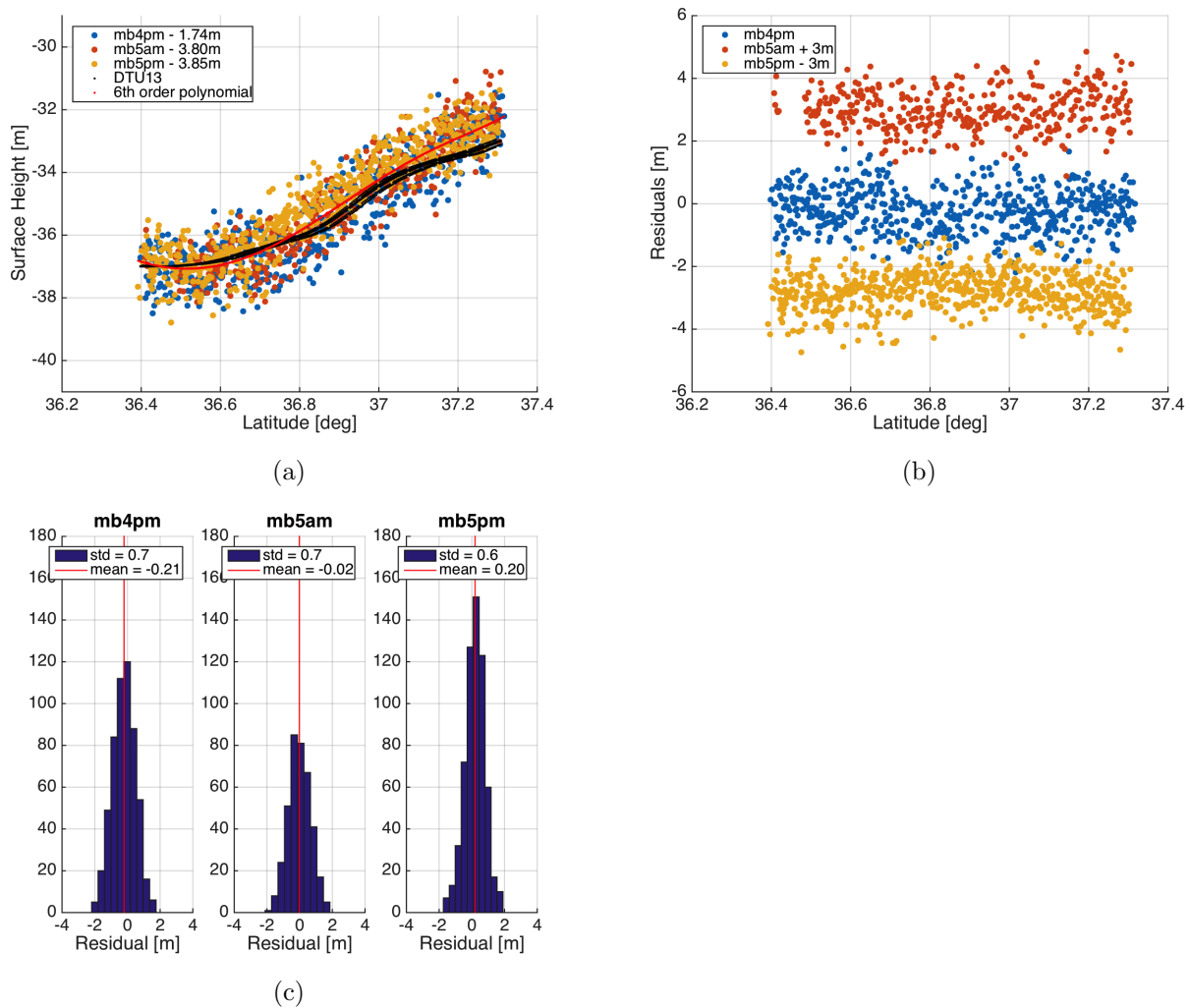


Figure 3.10: Leg 9 surface heights, height anomalies, and residual distributions from MB4PM, MB5AM, and MB5PM. (a) The measured surface heights from three flights over leg #9 biased to have zero mean residuals from the DTU13 mean sea surface (black). A 6th order polynomial is fit to the data from all four flights and shown in red. The residuals of each flight over leg #9 from a 6th order polynomial fit shown against (b) latitude and (c) in histograms.

### 3.5 Conclusions and Future Work

Out of the three timing retrieval methods investigated here it has been shown that the HALF algorithm yields the most precise results. However, there is one drawback in that

the method tracks an arbitrary point on the correlation waveform. In this case 70% of the peak power was chosen. Tracking the 60% power point would be equally justifiable. Such an arbitrary point leads to measurement biases that in the future will need to be calibrated.

The PARA3 method did not meet expectations and the implementation stands to be improved. However, whether this method has the potential to match or surpass HALF is unknown. In future work the following improvements should be considered for the PARA3 method.

- (1) Use a measured direct signal waveform in place of the simulated auto-correlation function when constructing the PARA3 waveform model.
- (2) Add a 4<sup>th</sup> parameter to the function  $f(t | \tau, A, \alpha)$  that will describe a finite leading edge slope from zero to amplitude A.
- (3) Explore a non-exponential decay of the function  $f(t | \tau, A, \alpha)$ .

There are some improvements and future work to be done in regards to the measurement accuracy assessment as well. There are mean biases, and systematic trends in the height measurement error with respect to the DTU13 mean sea surface that have been left uncorrected. The following steps should be taken.

- (1) Include a full scattering model to simulate waveforms and track delays.
- (2) Develop a roughness (or waveform width) dependent “simple” tracking algorithm.
- (3) Incorporate localized mean surface and tidal models.

Despite some systematic errors, a simple bias correction to each flight shows that this data set is consistent and repeatable. After applying corrections for tides, tropospheric delays, aircraft motion and the antenna baseline the repeated measurements of the surface are repeatable and consistent with the others. This result gives confidence that the time and geometry dependent corrections are valid and have been applied correctly.

A foundation for GNSS-R altimetry has been built here that can be adapted to the spaceborne case. These models and altimetry corrections will be adapted and used with publicly released data from TechDemoSat-1 of Surrey Satellite Technologies. Beyond adapting these existing models, models for ionospheric delays and adjustments for spacecraft motion will need to be implemented.

### **Acknowledgment**

This research was supported by the National Aeronautics and Space Administration Jet Propulsion Laboratory. The authors would like to thank Victor Zlotnicki, Richard Ray, Bruce Haines, and Dallas Masters for their valuable contributions.

## Chapter 4

### Global Ocean Altimetry With GNSS Reflections From TechDemoSat-1

Journal version<sup>1 2 3</sup> :

[Mashburn et al., 2018] J. Mashburn, P. Axelrad, S. T. Lowe and K. M. Larson, “Global Ocean Altimetry With GNSS Reflections From TechDemoSat-1,” in IEEE Transactions on Geoscience and Remote Sensing, vol. 56, no. 7, pp. 4088-4097, July 2018. doi:10.1109/TGRS.2018.2823316

#### Abstract

TechDemoSat-1 (TDS-1) is an experimental GNSS Reflections (GNSS-R) satellite deployed in 2014. The GNSS-R receiver onboard performs real-time navigation and generates delay-Doppler correlation maps for Earth-reflected GPS L1 C/A ranging signals. This research investigates the performance of the TDS-1 data for ocean surface altimetry retrievals. The analysis includes consideration of the transmitter and receiver orbits, time tag corrections, models for ionospheric and tropospheric delays, zenith to nadir antenna baseline offsets, ocean and solid Earth tides, and a comparison with mean sea surface topography. An error budget is compiled to account for each error source and compared to the experimentally derived surface height retrievals. By analyzing data sets covering global ocean surfaces over +/- 60 deg latitude, the current performance of spaceborne GNSS-R altimetry

---

<sup>1</sup> Some formatting changes have been made to accommodate different citation and print styles.

<sup>2</sup> The re-tracking method referred to here as HALF was renamed P70 after this publication was printed.

<sup>3</sup> Equation (4.12) has been corrected from the IEEE TGRS print version.

with the TDS-1 data set is experimentally established. In comparison with mean sea surface topography, the surface height residuals are found to be 6.4 m,  $1\sigma$  with a 1 sec integration time. A discussion of the factors limiting this performance is presented, with implications for future GNSS-R altimetry missions designed for observation of mesoscale ocean circulation.

## 4.1 Introduction

Analysis and flight experiments have demonstrated that transmissions from Global Navigation Satellite System (GNSS) satellites can be used as opportunistic signals for multi-static remote sensing of ocean, land, and ice surfaces around the globe. The application of GNSS Reflectometry (GNSS-R) to ocean altimetry was initially proposed by Martin-Neira [1993] almost twenty-five years ago, with more recent studies advancing the analysis of system requirements and expected performance [Cardellach et al., 2014; D’Addio et al., 2011; Li et al., 2016; Lowe et al., 2002c; Martin-Neira et al., 2011; Masters et al., 2001; Semmling et al., 2016; Zavorotny and Voronovich, 2000]. These studies explore the advantages of multi-static GNSS-R over active monostatic spaceborne altimetry. Specifically, they identify reductions in onboard power requirements, system complexity, and cost for a non-transmitting GNSS receiver as compared to an active radar instrument; and increases in coverage made possible by simultaneous tracking of reflected signals from multiple GNSS satellites. It has been shown in recent simulations by Li et al. [2016], that an optimized spaceborne GNSS-R altimetry platform could produce scientifically valuable results for mesoscale oceanography. This requires spatial resolution on the order of tens of kilometers, with sub-meter height resolution [Li et al., 2016; Rapley et al., 1990].

Past GNSS-R experiments have largely focused on land-based and airborne receiver experiments demonstrating novel methodologies for applications such as altimetry, tide monitoring, soil moisture, sea surface roughness and wind speed [Cardellach et al., 2011, 2014; Chew et al., 2016; Larson et al., 2013; Mashburn et al., 2016; Zavorotny and Voronovich, 2000]. Space-based experimentation has been limited to fortuitous circumstances [Lowe



et al., 2002a] and a few technology demonstration missions [Clarizia et al., 2016; Ruf et al., 2016; Unwin et al., 2003, 2010, 2011]. With the December 2016 launch of the 8-satellite CYGNSS constellation, a GNSS-R science mission designed to measure ocean surface wind speeds, there is also growing interest in assessing the capability of reflected GNSS signals for ocean altimetry from space. While dedicated experiments to demonstrate space-based GNSS-R altimetry are actively being planned [Martin-Neira et al., 2011; Wickert et al., 2016], such a platform does not currently exist. Further, performance analysis of code-based altimetry from space, especially with flight data, has been very limited in geographic scope, completeness of the path delay model, and re-tracking methods. One recent example is an early analysis of TechDemoSat data for use in GNSS-R altimetry by Clarizia et al. [2016].

Our objective is to more fully establish the current level of spaceborne GNSS-R altimetry performance based on flight data from a GNSS-R technology demonstration not specifically designed for this purpose. We use data from TechDemoSet-1 (TDS-1) to examine open ocean measurements from around the globe at all times of day, and incorporate corrections for common propagation effects and dynamic surface topography. This methodology maximizes the amount of data used from each collection period, generalizes the retrieval of surface height measurements to all open ocean points, and yields the most precise experimental retrievals to date.

Taking advantage of publicly available GNSS-R data sets from the TechDemoSat-1 mission, a pre-cursor to CYGNSS also developed by Surrey Satellite Technology Ltd [Unwin et al., 2010, 2011], we characterize the performance of GNSS-R ocean altimetry using GPS L1 C/A code measurements. An error budget detailing the known error sources is compiled and compared with experimentally derived results. In doing so, we present the first global analysis of spaceborne GNSS-R ocean altimetry and describe practical techniques for correcting the effects of ionospheric and tropospheric delays, receiver/transmitter orbital motion, and the receiving antenna geometry. The following sections describe the TDS-1 mission, instrumentation, data sets, and results from sea surface height retrievals compared

to models accounting for geoid topography, ionospheric and tropospheric delays, and precise reflection geometries. The limitations and issues encountered with these data are discussed, along with recommendations for future altimetry specific GNSS-R work.

## 4.2 Spaceborne GNSS-R with TechDemoSat-1

The Surrey Satellite Technology Ltd (SSTL) TDS-1 spacecraft, carrying an SGR-ReSI instrument, was launched into a sun-synchronous orbit with 650 km altitude in July 2014 [Unwin et al., 2010]. From this vantage point, TDS-1 can view the entire globe, pole to pole, while remaining continuously within view of the medium Earth orbit (MEO) GNSS constellations. As TDS-1 orbits below the GPS constellation, specular reflection ray paths connecting the transmitter, surface, and receiver, track along the surface. Fig. 4.1 illustrates the spaceborne reflection geometry and the observed reflection ground-track coverage of TDS-1 for the data sets used in this analysis. All of the reflection data analyzed here are taken from the MERRByS portal, [www.merrbys.co.uk](http://www.merrbys.co.uk), where SSTL has made the TDS-1 measurements freely available to the international community [Unwin et al., 2011].

The SGR-ReSI receiver was chosen to fly on TDS-1 as a technology demonstration in preparation for its use as the primary instrument for observation of ocean wind speeds on the CYGNSS mission [Ruf et al., 2016]. Thus, the GNSS-R receiver system on TDS-1 has been optimized for ocean surface wind speed retrieval rather than altimetry. The resulting limitations and issues for altimetry include a relatively low-gain nadir pointing antenna; imprecise onboard positioning and timing with no recorded carrier phase data; tracking of only single-frequency, low-bandwidth signals, and uncertainty in the onboard reflection tracking point that inhibits accurate retracking in post-processing. Despite these issues, which are discussed in detail in the following sections, the TDS-1 experiment does provide the most extensive spaceborne GNSS-R data set gathered to date, allowing a realistic, global assessment of GNSS-R altimetry performance to be carried out.

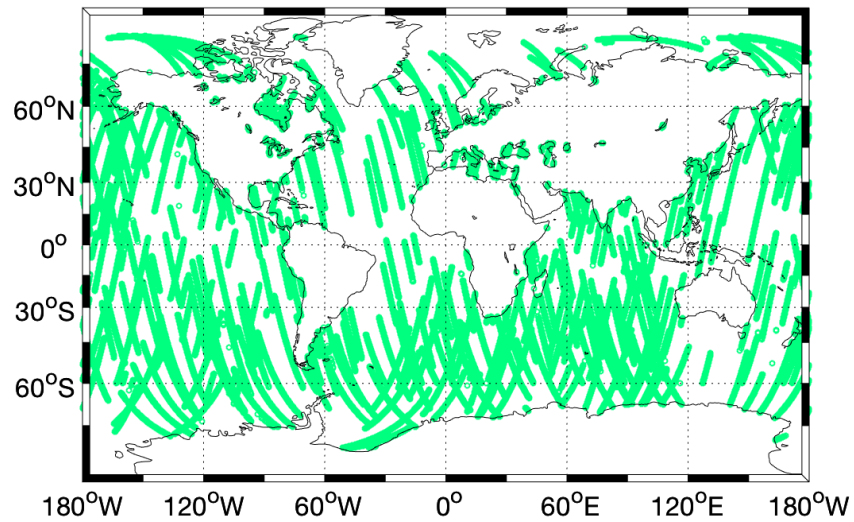
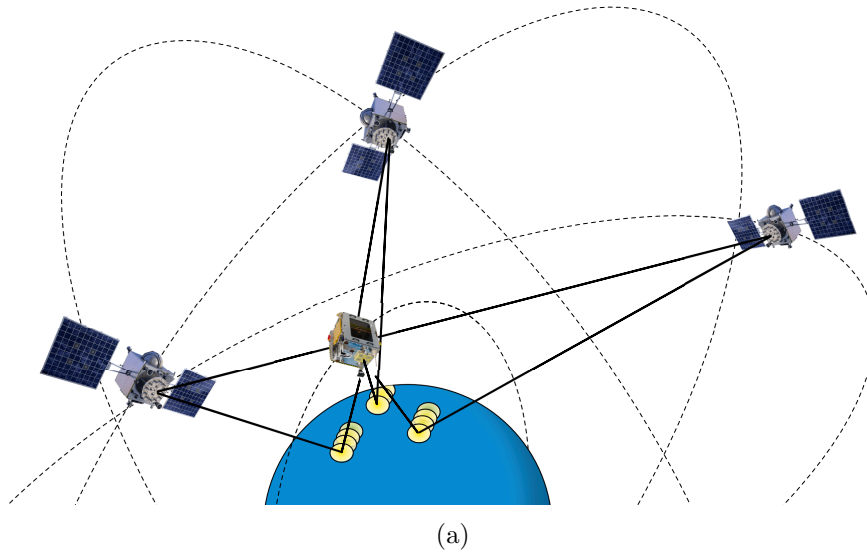


Figure 4.1: Spacebased GNSS-R and the TDS-1 global coverage in 4 days. (a) Cartoon of the GNSS-R event geometry. As the transmitter (GPS) and receiver (TDS-1) orbit, the specular reflection points track along the surface. Multiple reflection events may occur simultaneously originating from different transmitters. (b) Global reflection ground track coverage from TDS-1 over four days from datasets RD17 and RD18 (available at [www.merrbys.co.uk](http://www.merrbys.co.uk)). About 100,000 reflection events are observed here. The data are masked to exclude land reflections.

For the analysis presented in this paper, data from two collection periods, RD17 and RD18, spanning four days and more than 100,000 reflection events in February 2015 are selected. Reflection retrievals from these data sets demonstrate consistently strong signal-to-noise ratios, with reflected signal path delays from which systematic effects can be effectively calibrated. The available data include measured delay-Doppler maps (DDMs) [Garrison and Katzberg, 2000; Lowe et al., 2002c; Unwin et al., 2010] and synchronized metadata describing the reflection time, receiver clock corrections, and the computed receiver, transmitter, and reflection locations [Jales, 2016].

Unwin et al. describe the SGR-ReSI receiver and its implementation on TDS-1 [Unwin et al., 2010, 2011]. GNSS tracking on TDS-1 is limited to only the GPS L1 C/A signal for both positioning and reflection tracking. The satellite carries a standard  $\sim 4$  dBi zenith-pointing RHCP antenna for direct signal tracking and a 13 dBi nadir-pointing LHCP antenna for reflection tracking. The SGR-ReSI has 28 tracking channels, with the ability to track 24 direct and 4 indirect signals [Unwin et al., 2011].

Direct signals are tracked using a standard early-minus-late delay lock loop, from which pseudorange measurements are derived [Misra and Enge, 2006]. An onboard navigation processor forms point position and clock solutions from these observations every second. Based on the direct position solution and the broadcast GPS satellite ephemerides, a computationally efficient geometric model is implemented onboard to predict the location and delay for a reflected signal from the Earth surface. An open-loop tracking algorithm is applied to the reflected signal, in which the signal received by TDS-1 nadir-pointed antenna is correlated against a locally generated model of the direct line-of-sight signal, offset by the expected delay and Doppler. The resulting correlation power is sampled in delay and Doppler space to form a DDM as described in [Garrison and Katzberg, 2000; Lowe et al., 2002c; Unwin et al., 2010]. DDMs for highly specular reflections appear as simply attenuated and delayed versions of the direct signal. DDMs for reflections from a rough ocean surface exhibit the characteristic horseshoe shape shown in Fig. 4.2, [Garrison and Katzberg, 2000].

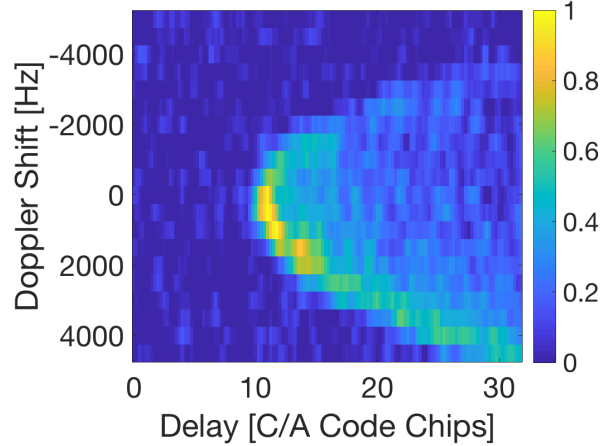


Figure 4.2: Example TDS-1 ocean reflection DDM. An example delay-Doppler map generated from tracking an ocean reflected signal. Correlation power is sub-divided into delay and Doppler bins to produce a DDM.

### 4.3 Ocean Altimetry Retrieval Methods

The three key features of the DDM are its shape, amplitude, and time delay (or path delay when multiplied by the speed of light) relative to the direct signal. The observed shape and amplitude of the DDM correlation function are highly dependent on the reflecting surface roughness that determines the scattering area and thus spread of the waveform in delay; and the dielectric constant that determines the scattered power. Determining the time delay of the specular reflected signal with respect to the direct, allows retrieval of a relative surface height [Garrison and Katzberg, 2000]. That excess path delay of the specular reflection ray with respect to the direct ray is determined by re-tracking the delay of the correlation function recorded in the DDM [Cardellach et al., 2014]. The specular point delay is used as the track point, because it can be readily modeled and is less sensitive to roughness than the delay of the peak power or other possible track points on the waveform.

To assess the accuracy of GNSS-R we compare the re-tracked/measured delay with a precise delay model. We define the measured delay anomaly as the difference between the observation and model as given by

$$\Delta\delta = \delta_{measured} - \delta_{modeled}. \quad (4.1)$$

Delay anomaly (here in units of distance) is mapped into height anomaly from the modeled surface by

$$\Delta h = \frac{\Delta\delta}{2 \cdot \cos(\theta)} \quad (4.2)$$

where  $\theta$  is the reflection incidence angle. This trigonometric relation is derived from assuming that (a) the transmitter is far enough away that the incoming ray paths can be considered parallel, and (b) the reflecting surface is flat. While neither assumption is completely valid when considering the total excess path delay to a receiver in low Earth orbit, for the purpose of mapping range **anomalies** to height **anomalies**, the simplified mapping function is quite sufficient, introducing errors  $\leq 1$  mm in height. This error bound has been established based on comparisons with precisely iterated solutions as presented by Wu et al. [1997].

Excess path delays are estimated across the entire globe using precise spacecraft orbits, mean sea surface topography, modeled atmospheric delays, and knowledge of TDS-1 antenna configuration. The following sub-sections detail the high-fidelity reflection model, the operation of the TDS-1 SGR-ReSI open loop reflection tracking, the approach we used for waveform re-tracking, and the calibrations we performed with the TDS-1 data set.

#### 4.3.1 Reflection Modeling

A high-fidelity model was assembled to simulate the true reflection geometry and signal propagation errors as accurately and precisely as possible. Each component of the model, the information source, and the estimated uncorrected and residual errors of that model component are listed in Table 4.1. The high-fidelity model estimates the delay of the reflected signal using the receiver coordinates from the metadata with corrections for the antenna baseline,

transmitter coordinates from the International GNSS Service (IGS) final orbits corrected for direct and reflected signal flight times [Dow et al., 2009], specular point coordinates computed on the DTU10 mean sea surface model from the Technical University of Denmark (DTU) [Andersen, 2010] with ocean and solid body tidal corrections [McCarthy and Petit, 2004; Ray, 1999; Stammer et al., 2014], and modeled ionospheric [Bilitza, 2015; Komjathy, 1997; Montenbruck and Gill, 2002] and tropospheric [Leandro et al., 2006] delays. Electromagnetic bias is not included in the model at this point because the magnitude, estimated to be  $10 - 20$  cm [Camps et al., 2017; Ghavidel et al., 2016], is well below other current limitations of the observations and models.

Table 4.1: Model components with expected RMS error if left uncorrected and residual errors after correction.

| Name                  | Source                                    | Uncorrected         | Residual Error                |
|-----------------------|---|---------------------|-------------------------------|
|                       |   | Magnitude           |                               |
| TDS-1 orbit error     | Metadata                                  | 2.6 m position      | 2.6 m position ( $1\sigma$ )  |
| GPS orbit error       | [Dow et al., 2009; IGS]                   | 1 m position        | 0.03 m position ( $1\sigma$ ) |
| DTU10 MSS topography  | [Andersen, 2010]                          | 100 m height        | 0.1 m height ( $1\sigma$ )    |
| Quasi-spherical Earth | [Jales, 2016]                             | 15 m delay          | 0 m delay                     |
| Ocean/Body Tides      | [McCarthy and Petit, 2004; Ray, 1999]     | 2 m height          | 0.1 m height ( $1\sigma$ )    |
|                       | [Stammer et al., 2014]                    |                     |                               |
| Ionosphere delay      | [Bilitza, 2015; Komjathy, 1997]           | < 15 m delay (day)  | < 5.2 m delay (day)           |
|                       | [Kumar, 2016; Montenbruck and Gill, 2002] | < 7 m delay (night) | < 2.5 m delay (night)         |
| Troposphere delay     | [Leandro et al., 2006]                    | 6 m delay           | 0.05 m delay ( $1\sigma$ )    |
| Antenna Baseline      | Metadata                                  | 1 m delay           | 0.001 m delay ( $1\sigma$ )   |



TechDemoSat-1 uses GPS L1 C/A code pseudoranges for real-time positioning. A navigation solution is calculated at 1 Hz, then decimated onboard and down-linked at 0.1 Hz. The 0.1 Hz points are interpolated in ground-processing back to the DDM measurement times [Jales, 2016]. There are, of course, limitations in the real-time navigation such as the broadcast ephemeris, clock errors, ranging noise, uncorrected ionospheric delays, as well as interpolation artifacts in the published metadata. High-pass filtering the receiver orbit positions to remove long period systematic behavior reveals that the point solution variability is  $\sim 2.6$  m in 3D position. The orbit reported in the metadata for TDS-1 has been used in the high-fidelity reflection model - this is the best option since we do not have knowledge of the exact onboard solution used for positioning the reflection tracking delay offset, or high-quality, raw pseudorange and phase observations that could be used to construct a more precise post-processed orbit solution for TDS-1.

The high-precision, final GPS satellite orbit and clock products, estimated by the IGS [Dow et al., 2009] are used in computing the high-fidelity model. The broadcast ephemerides, which are used in the onboard real-time navigation of TDS-1, are estimated to be accurate to  $\sim 1$  m while the final orbits are estimated to be accurate to  $\sim 3$  cm in position [IGS]. Corrections to the location of the transmitter for both the direct and reflected signals' time of flight are accounted for, in order to accurately estimate the geometry of the observation. The signal time of flight correction is  $\leq 20$  cm in the reflection path delay.

The reference used for the reflecting surface is the DTU10 mean sea surface, a 2 arc-minute resolution gridded mean ocean topography map from the Danish Technical University [Andersen, 2010]. Ocean tide corrections from the Global Ocean Tide 4.10 (**GOT4.10**) model and solid body tides<sup>4</sup> are superimposed on the reference surface. Residual height errors from the tidal models are estimated to be about 0.1 m [Stammer et al., 2014]. The **GOT4.10** model as it was used here includes ocean tides, and load tides. Solid body tides

---

<sup>4</sup> The solid body codes are available from Dennis Milbert at <http://geodesyworld.github.io/SOFTS/solid.htm>.

are estimated from McCarthy and Petit [2004].

Given this surface, and the time history of positions of the TDS-1 receiver and GPS transmitters, we implement an iterative approach developed by Wu, et al. (1997) to compute the expected location of the specular reflection point on the surface [Wu et al., 1997]. The iteration adjusts the reflection point until the incident and reflecting angles agree to within 0.001 deg tolerance.

In real time, TDS-1 predicts the delay and Doppler offsets of the specular point with a computationally efficient quasi-spherical Earth model that approximates the WGS84 reference ellipsoid [Jales, 2016]. This onboard model yields a reflection position that correctly predicts delay to within 15 m, and Doppler to within 250 Hz of the WGS84 ellipsoid solution. The quasi-spherical Earth solution delay error, with respect to the WGS84 solution, for a given geometry is known and completely accounted for in our model. Compensation for the Doppler error in the onboard model is not necessary, because for the elevation angle of reflections considered here the error is always much less than the 250 Hz model error upper limit and much less than the Doppler resolution of the DDM measurements. Therefore, the targeted Doppler bin of the DDM is used for re-tracking as described in Section 4.3.2.

Corrections for ionospheric and tropospheric delays are also required. High-precision orbit determination and scientific observations with GNSS rely on dual-frequency (L1 and L2) measurements to directly measure and remove ionospheric effects [Brunner, 1991]. Unfortunately, TDS-1 and other low cost missions, tend to forgo the dual-frequency capability, relying solely on single-frequency L1 measurements. Ionospheric models and mapping algorithms have been developed to support such missions. We use the International Reference Ionosphere 2012 (IRI2012) [Bilitza, 2015] to model the vertical total electron content ( $vTEC$ ) values at ionospheric pierce points associated with each of the three ray paths illustrated in Fig. 4.3, namely, the rays from the GPS transmitter to TDS-1 ( $vTEC_3$ ), the GPS transmitter to the ground reflection point ( $vTEC_1$ ), and the reflection point to the TDS-1 ( $vTEC_2$ ). The literature on ionospheric delay modeling suggests that the International Reference Iono-

sphere 2012 (IRI-2012) model may have an error up to about 35% in estimation of TEC [Kumar, 2016].

The vTEC values estimated for the two pierce points on the reflected path are mapped to slant path delays with the mapping function

$$M_{1,2}(E) = \frac{1}{\sqrt{1 - \left( \cos(E) \cdot \frac{R_E}{R_E + h} \right)^2}} \quad (4.3)$$

given by Equation 4.20 in Komjathy [1997], where  $E$  is the elevation angle at the reflection point,  $R_E$  is the Earth's radius, and  $h$  is the ionospheric shell height chosen to be 400 km.

Correction of ionospheric delay on the direct signal from the GPS to the TDS-1 is performed using a method developed by Montenbruck and Gill [2002]. The TEC column value,  $vTEC_3$  in Fig. 4.3, is computed from IRI2012 extending to its uppermost altitude limit of 2000 km. Then the mapping function given by Montenbruck and Gill [2002], specifically formulated to compute slant path delays for low Earth orbiting spacecraft, is given by,

$$M_3(E_{IP}) = \frac{\alpha}{\sin(E_{IP})} \quad (4.4)$$

where  $E_{IP}$  is the elevation angle of the line of sight path through the ionospheric pierce point, and  $\alpha$ ,

$$\alpha = \frac{e - \exp(1 - \exp(-z_{IP}))}{e - \exp(1 - \exp(h_0/H))}, \quad (4.5)$$

is a scaling factor for the ionospheric density above the receiver altitude, which depends on the receiver altitude,  $h_s$ , the shell height,  $h_0$ , and a scale height,  $H$ . The scaled height of the ionospheric pierce point,  $z_{IP}$ , is solved for from

$$\begin{aligned} \exp(1 - \exp(-z_{IP})) &= \frac{1}{2}(e + \exp(1 - \exp(-z_s))); \\ z_s &= (h_s - h_0)/H. \end{aligned} \quad (4.6)$$

The total group delay along the reflected and direct ray paths is then estimated from those slant TEC values by

$$\delta_{1,2,3} = M_{1,2,3} \cdot \frac{40.3 \times 10^{16} \cdot vTEC}{f_{L1}^2} \quad (4.7)$$

and the excess delay on the reflected signal due to the ionosphere is modeled by

$$\delta_{iono} = (\delta_1 + \delta_2) - \delta_3. \quad (4.8)$$

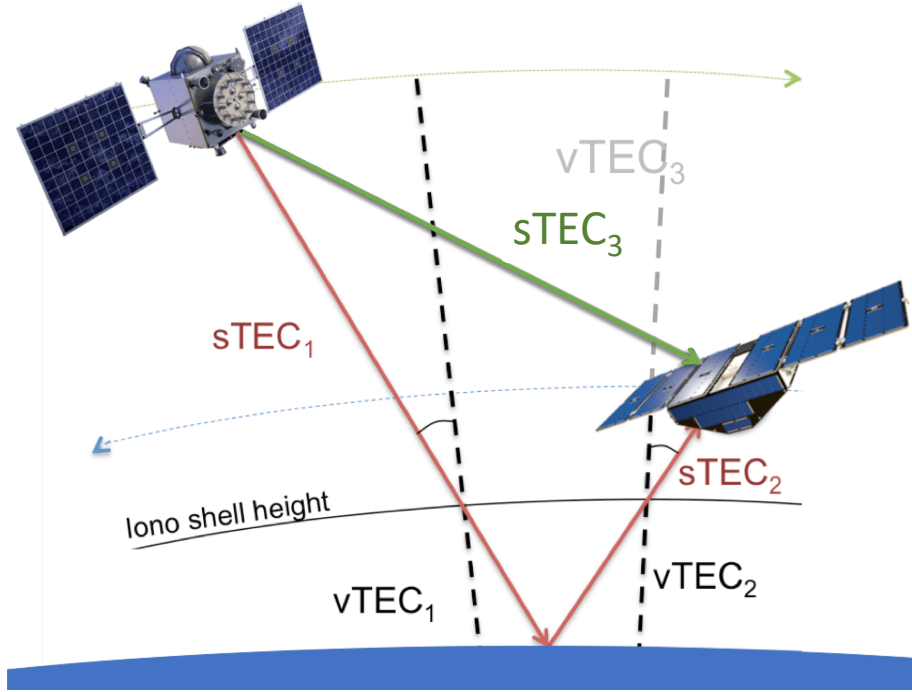


Figure 4.3: Ionospheric delay model. The ionospheric delay effect is estimated on the reflected signal ray path. Vertical TEC ( $vTEC$ ) columns at the up and down-traveling pierce points are evaluated from the IRI2012 model and mapped to slant angles. The summed slant TEC is used to estimate the excess delay effect.

Tropospheric delays are accounted for using the UNB3m model from the University of New Brunswick [Leandro et al., 2006]. UNB3m uses empirically derived average atmospheric parameters computed for a grid of latitudes and seasons, Saastamoinen zenith delays [Davis

et al., 1985], and Niell mapping functions [Niell, 1996] to estimate delays. Leandro, et al. estimate a residual delay error of  $\sim 5$  cm [Leandro et al., 2006] as compared to radiosonde measurements. Tropospheric corrections are only applied to the downward and upward reflected signal paths below the receiver altitude. No tropospheric correction is required for the direct signal path to the spaceborne receiver, because the tropospheric effects are highly concentrated below an altitude of 10 km, and we are considering only transmitting satellites at elevation angles above 60 deg. The UNB3m model is evaluated at the specular point latitude and doubled to account for the down and up-traveling paths. As modeled by UNB3m, the latitudinal change of the tropospheric propagation delay is less than 0.5 cm/deg, and the pierce points of each reflection path through the troposphere are approximately 10 km apart. Therefore, evaluating the model at two separate pierce points is deemed unnecessary.

When constructing the expected excess path delay for the reflected signal, one must also take into account the baseline offset between the zenith antenna used to track direct signals, and the nadir pointed antenna used to track reflections. To make this correction precisely, one would need information on the antenna installations, the effective phase centers of the two antennas, and the attitude or orientation of the satellite in its orbit. For TDS-1, we are given the coordinates of the antenna internal center on the face where it is mounted to the spacecraft body and we know that the spacecraft is controlled such that the body frame is aligned with the orbit local-level, local-horizontal (LVLH) frame [Jales, 2016; Jales and Unwin, 2015]. The body frame x-axis is aligned in the velocity direction, the body frame z-axis is aligned in the orbit radial (local vertical) direction, and the body y-axis completes the right handed coordinate system. Thus, the antenna baseline vector,  $\vec{b} = [-264.1, 399.1, -910.8]^T$  mm, given in the body frame is used to model the delay effect for a given incident signal by

$$\delta_{baseline} = (\mathbf{R} \vec{b}) \cdot \hat{e} \quad (4.9)$$

where  $\mathbf{R}$  is the rotation matrix from the LVLH frame to the earth-centered, earth-fixed (ECEF) frame,  $\vec{b}$  is the antenna baseline vector expressed in the body frame, and  $\hat{e}$  is the line of sight direction to the GPS transmitter expressed in the ECEF frame. The rotation matrix  $\mathbf{R}$  is computed from the basis vectors of the LVLH frame by

$$\mathbf{R} = \begin{bmatrix} \hat{v}_1 & \hat{c}_1 & \hat{r}_1 \\ \hat{v}_2 & \hat{c}_2 & \hat{r}_2 \\ \hat{v}_3 & \hat{c}_3 & \hat{r}_3 \end{bmatrix} \quad (4.10)$$

where  $\hat{v}$  is the spacecraft velocity direction (in-track),  $\hat{r}$  is the orbit radial (local vertical) direction, and  $\hat{c}$  completes the set in the cross-track direction, each written in the ECEF frame.

After accounting for each of the systematic delay effects described above, a bias of 8.8 m is observed between the measured excess delay and the high-fidelity model. We attribute this bias to a combination of the re-tracking measurement bias and uncalibrated receiver hardware biases. It was found to be constant across all of the data sets analyzed here, thus, in the remaining results this fixed delay bias has been removed.

Finally, the statistics of the signal tracking errors due to noise were investigated through a Monte Carlo analysis. A subset of data ( $N \approx 64,000$  waveforms) was chosen for this analysis that spanned the full range of latitudes, longitudes, and observed signal-to-noise-ratios (SNR's). For each correlation waveform the random noise on the samples was estimated by taking the standard deviation of the amplitude of those samples at early delays, where no reflected signal power is present. Gaussian distributed random noise values with zero mean were generated and superimposed on the original waveform. This new realization of each measured waveform is made by

$$x_i[n] = x[n] + w[n] \quad (4.11)$$

where  $x[n]$  are the original samples,  $w[n]$  are the random noise values, and  $x_i[n]$  are the

samples that make up the  $i$ th waveform realization. This implementation ignores the effects of speckle noise on the waveform samples. For the vast majority of the observed waveforms, the contribution of speckle noise was estimated to be less than that of the sample noise that was calculated as described above. Therefore, we have determined that the addition of speckle noise on the waveform samples would not meaningfully alter the estimated tracking error results.

For each measurement, 100 realizations were created and then re-tracked as described in Section 4.3.2. The change in re-track delay as a function of SNR is shown in Fig. 4.8. Here we define SNR similarly to Lowe et al. [2002a] and Lowe [1999] as

$$SNR = \frac{P_{max} - P_{noise}}{\sigma_{noise}}, \quad (4.12)$$

where  $P_{max}$  is the peak measured correlation power,  $P_{noise}$  is the mean noise power, and  $\sigma_{noise}$  is the noise power standard deviation.

### 4.3.2 DDM Re-tracking

A specular delay measurement is made from each 1-second incoherently integrated DDM. A slice along the delay axis of the DDM correlation function at the targeted Doppler shift creates a one-dimensional waveform that is used to re-track the specular reflection delay, see Fig. 4.4. The HALF re-tracking algorithm has been implemented similarly to our previous work with the Monterey Bay GNSS-R data set [Mashburn et al., 2016]. A point on the leading edge of the correlation waveform at 70% of the maximum correlation power is chosen as the re-tracking point. This HALF method, derived from standard monostatic radar techniques, is simple, computationally efficient, and results in a more precise delay measurement than other point tracking techniques like the leading edge maximum derivative [Cardellach et al., 2014; Hajj and Zuffada, 2003; Mashburn et al., 2016]. The 8.8 m calibrated bias described in the previous section, compensates for the re-tracking delay offset of the 70% power point.

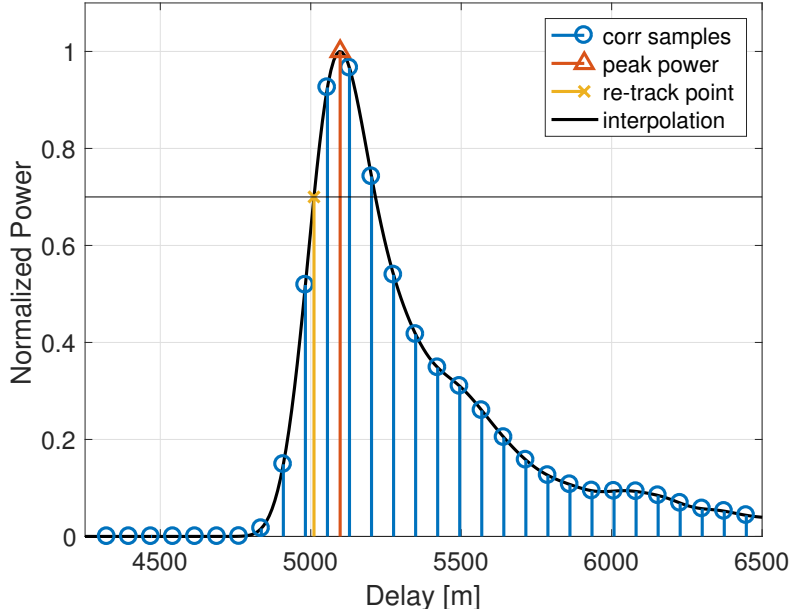


Figure 4.4: Example of P70 re-tracking on a measured correlation waveform. An example of the correlation function re-tracking. First, the noise floor is determined by the average correlation value of the first 20 samples (not shown) and removed. The correlation waveform is then normalized by the peak power and the 70% tracking point is determined.

Tracking a specific point on the correlation waveform requires interpolation between samples. To do this, the noise floor is first computed by averaging correlation values of the first 20 samples where no signal is expected to be present, and then subtracted from the correlation measurements. A Whittaker-Shannon interpolation of the adjusted correlation measurements is used to precisely determine the desired points, as follows,

$$x(\delta) = \sum_{n=-\infty}^{\infty} x[n] \cdot \text{sinc}\left(\frac{\delta - nd}{d}\right) \quad (4.13)$$

where  $x[n]$  are the normalized correlation samples after the noise floor has been removed,  $\delta$  is continuous delay, and  $d$  is the sampling period. Newton's method is used to first locate the peak power point on the waveform and then the 70% re-track point.



### 4.3.3 On-board Delay Calculation and DDM Correlator Positioning

The TDS-1 flight software employs open loop tracking to position a bank of correlators in delay and Doppler space to capture the surface reflected signal [Jales, 2016]. The open loop tracking process is based on the quasi-spherical Earth model described previously and uses the WGS84 Earth-fixed positions and velocities of the receiver (TDS-1) and transmitter (GPS) taken from the real-time 1 Hz navigation solution. Delay and Doppler offsets from the closed loop direct signal tracking are computed and used to position the DDM correlation window. The received signal is then correlated against a locally generated replica of the direct signal that comes out of the closed loop direct signal tracking used for navigation.

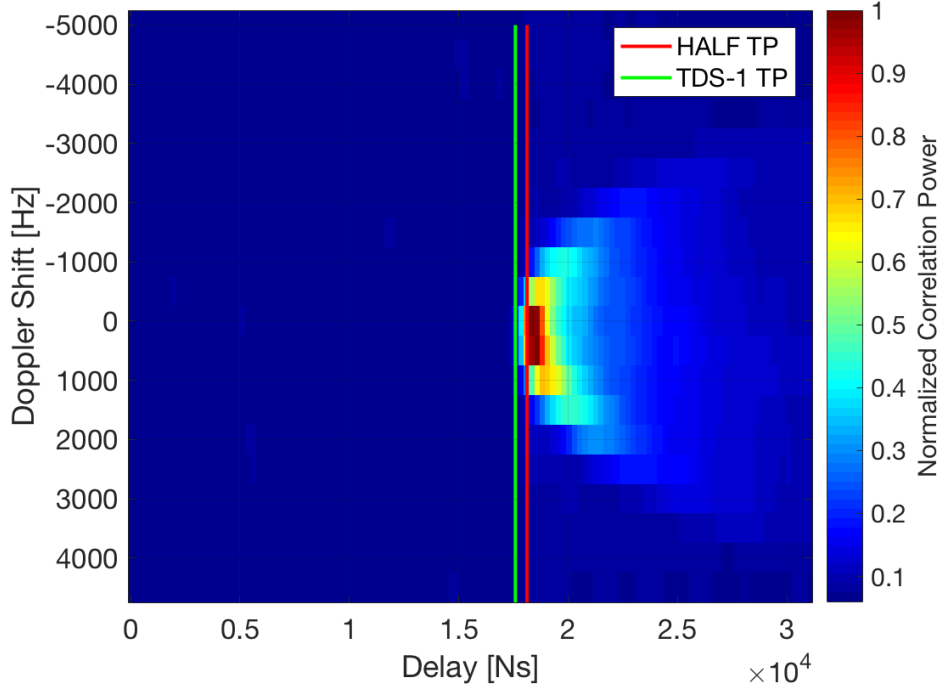


Figure 4.5: Delay retracking on a TDS-1 DDM. An example DDM is shown with the open loop tracking point ( $\delta_{TP}$  labeled TDS-1 TP) and re-track point ( $\delta_{re-track}$  labeled HALF TP) indicated. Note that the delay axis begins at zero delay at the front of the DDM window.

Each DDM spans a limited range of the delay and Doppler space and generally includes only the reflected signal correlation function. Within the DDM window, the on-board

reflection tracking point is specified by targeted delay ( $\delta_{TP}$ ) and Doppler ( $D_{TP}$ ) values. The tracking point ( $\delta_{TP}$ ,  $D_{TP}$ ) for a given DDM is referenced to the zero delay and zero Doppler of the correlation window (first row, center column of the DDM). Fig. 4.5 illustrates the measured re-tracking point and on-board predicted tracking point on an example DDM. The TDS documentation does not provide information about the direct signal tracking or the complete reflected signal delay-Doppler offsets. Because the DDM tracking point is provided as an offset from the target pixel, we must reconstruct the flight software reflection model in post processing to retrieve the full excess path delay. Therefore, the delay anomaly equation (4.1) is modified to become

$$\begin{aligned}\Delta\delta &= \Delta\delta_{measured} - \Delta\delta_{modeled} \\ &= (\delta_{re-track} - \delta_{TP}) \\ &\quad - (\delta_{HiFi} - \delta_{on-board} + \delta_{tropo} + \delta_{iono})\end{aligned}\tag{4.14}$$

where  $\delta_{re-track}$  is the measured delay on the DDM,  $\delta_{TP}$  is the on-board predicted delay on the DDM,  $\delta_{HiFi}$  and  $\delta_{on-board}$  represent the reflected signal excess path delays as computed by our high-fidelity geometric model and the reconstruction of the on-board calculations respectively, and  $\delta_{tropo}$  and  $\delta_{iono}$  are corrections for neutral and charged atmospheric delays.

#### 4.3.4 TDS-1 On-board Model Calibration

The altimetric observable quantity from the TDS-1 data set is the delay difference between the re-track point and the on-board predicted track point. This difference is the path delay error caused by the true surface topography, systematic signal delays (e.g. troposphere and ionosphere), and any errors in the TDS-1 data set. We have identified three issues with the TDS-1 metadata and the onboard reflection model, that are corrected or compensated for in our analysis by reconstructing and subtracting a  $\delta_{on-board}$  adjustment in (4.14). The observed on-board model implementation issues are as follows.

First, there is a leap second error between the given UTC and GPS time stamps in the

February 2015 metadata associated with each DDM. The UTC time stamps published in the metadata are computed on the ground by the SSTL analysis center, based on reported GPS times. An incorrect leap second adjustment has apparently been applied in the conversion. This error affects all of the time-dependent parameters published in the metadata (e.g. receiver orbits, transmitter orbits, specular point locations, etc.), because those parameters are interpolated or re-evaluated in ground processing based on the UTC time stamp. It has been determined that the published GPS time stamps are correct, based on clear correlations between sharp changes in reflection power and known landmarks on the surface such as rivers [personal communication, Clara Chew 05/2016]. In our analysis all of the UTC times and affected model components have been corrected. If left uncorrected, the leap second issued would produce delay errors in the range of  $\pm 2$  meters.

Second, the delay anomalies in our initial analysis showed a strong linear dependence on the reflected signal range rate, which can be indicative of an error in the reported measurement time tags. From this sensitivity to range rate, we have identified a consistent 0.1 second timing error between the TDS-1 open loop tracking model and the DDM measurements. A timing calibration correction has been applied in the high-fidelity model to account for this. If left uncorrected, the effect of this range rate dependent error would be quite large, on the order of  $\pm 100$  meters of delay ( $\pm 50$  meters height).

Finally, what appears to be a geolocation mis-tagging error has been observed. When attempting to reconstruct the on-board delay model,  $\delta_{on-board}$ , for a given epoch, we were advised to use the specular point coordinate from the following index as given in (4.15) below, see supplementary material S4 of Chew et al. [2016]. This result might indicate an indexing error in the TDS-1 onboard software used to predict the reflected signal delay. If uncorrected, the effect manifests itself in delay as a systematic latitude dependent error as if the predicted specular points are lagging. The effect of this error is large and a function of latitude, at  $\pm 50$  meters of delay.

$$\begin{aligned}
\delta_{onboard} = & \|GPS_{xyz}(i) - SPT_{xyz}(i+1)\| \\
& + \|TDS_{xyz}(i) - SPT_{xyz}(i+1)\| \\
& - \|GPS_{xyz}(i) - TDS_{xyz}(i)\|
\end{aligned} \tag{4.15}$$

#### 4.4 Results

Implementing the methods described in the previous section, we compared the GNSS-R retrieved sea surface heights with the DTU10 (2 arc-minute) mean sea surface using TDS-1 datasets RD17 and RD18. Each of the observed DDMs is processed to extract the reflection SNR as defined in (4.12). Measurements with SNR of at least 5 dB are considered candidates for altimetric retrievals. The mean observed SNR is 7 dB which has an expected tracking error of  $\sim 10$  m,  $1\sigma$ , as seen in Fig. 4.8(a). Observations are further limited to ocean regions where there is no possibility of ice coverage, specifically latitudes between N60 deg and S60 deg. These limits identified over 100,000 DDMs recorded in data sets RD17 and RD18, corresponding to 25% of the total collected, as viable for ocean altimetry. Further quality control filters removed any measurements with antenna gain  $< 5$  dB, delay residuals  $> 250$  m, and finally delay residual outliers greater than  $4\sigma$ . Ninety-seven percent of the high SNR ocean reflections in the RD17 and RD18 datasets passed this quality screening. Fig. 4.6 presents the height retrieval results, where it is clear that the measured surface topography and the DTU10 model match on a global scale.

Table 4.2: Residual delay and height anomalies from TDS-1 altimetry combining data sets RD17 and 18. The HALF re-tracking algorithm is used.

| Integration Times | $1\sigma$ Delay Anomaly | $1\sigma$ Height Anomaly |
|-------------------|-------------------------|--------------------------|
| 1 s               | 11.9 m                  | 6.4 m                    |
| 10 s              | 5.5 m                   | 2.9 m                    |
| 60 s              | 4.6 m                   | 2.6 m                    |

Quantitative results are given in Table 4.2 and Fig. 4.7 with standard deviations of the delay and surface height residuals presented for 1, 10, and 60-second along-track integration

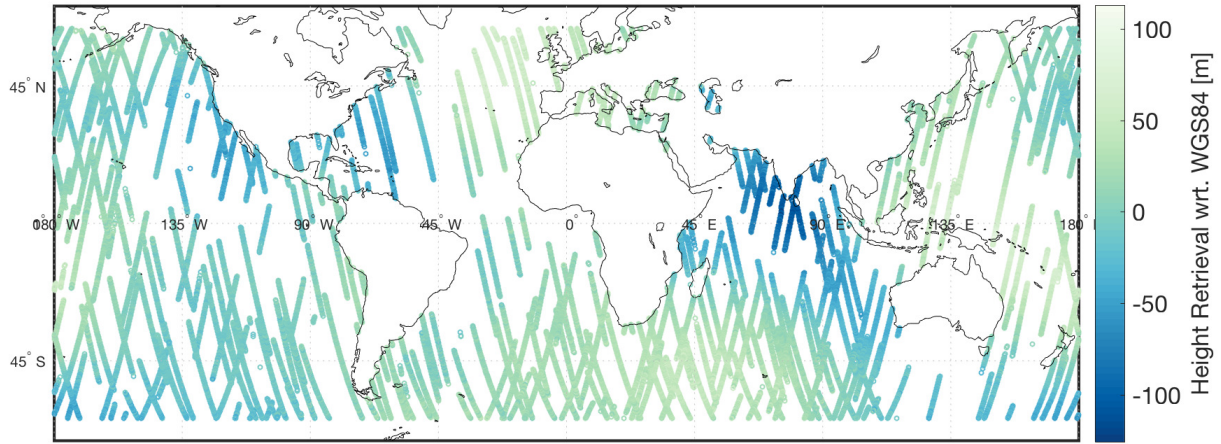
Table 4.3: Budget of residual measurement errors for a 1 second integration time.

| Error Source     | Residual Error                |
|------------------|-------------------------------|
| TDS-1 Orbit      | 2.6 m position ( $1\sigma$ )  |
| GPS Orbit        | 0.03 m position ( $1\sigma$ ) |
| Tides            | 0.1 m height ( $1\sigma$ )    |
| Ionosphere       | 4 m delay (day, RMS)          |
|                  | 2.2 m delay (night, RMS)      |
| Troposphere      | 0.05 m delay ( $1\sigma$ )    |
| Antenna Baseline | 0.001 m delay ( $1\sigma$ )   |
| Tracking Error   | 10 m delay ( $1\sigma$ )      |
| <b>RSS</b>       | 11.1 m (day)                  |
|                  | 10.6 m (night)                |

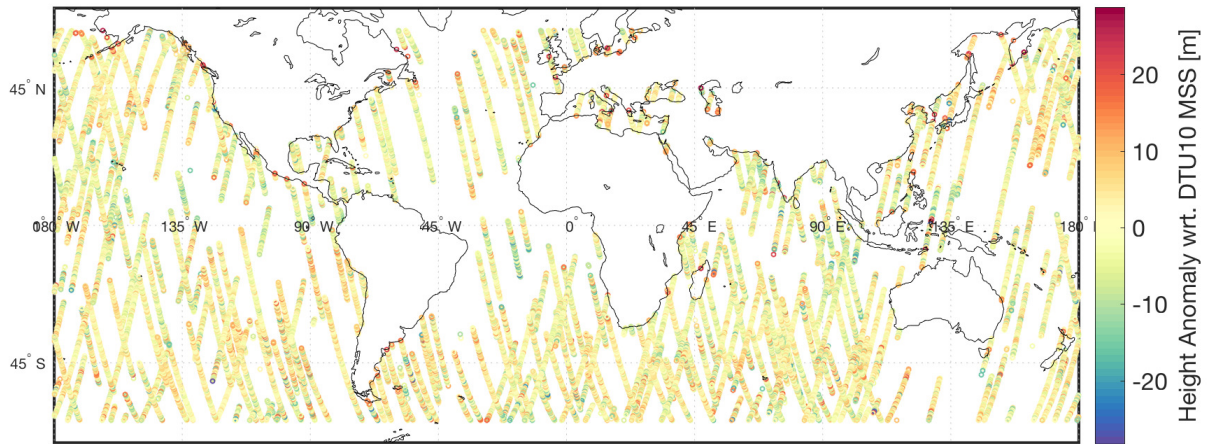
times. Noise in the retrievals can be reduced by incoherent integration of the measurements in time (along-track), or in spatial bins based on the reflection points. How best to perform these integrations must be informed by the type and scale of the surface features one is trying to observe. It should be noted that the delay and height anomaly standard deviations in our results do not reduce by a factor of  $\sqrt{N}$  as would be expected if the residuals were purely Gaussian white noise. The observed reduction indicates that there are some remaining systematic effects in our results on the order of 4.5 m, though they are clearly smaller than the noise observed in the 1 Hz measurements. It is likely that the residual delay errors from ionosphere and orbit errors presented in Table 4.3 are significant contributors to the residual systematic error as the reduction in delay anomaly is limited to around 4.5 m.

The 1-sec delay retrieval anomalies are seen to be well distributed in Fig. 4.7(a). Fig. 4.7(b) presents the delay anomalies plotted versus latitude, which shows no evidence of large geographic dependent effects visible in the residuals. For 1-second integrations the root-sum-square (RSS) of the tabulated residual errors (11.1 m (day) and 10.6 m (night), Table 4.3) matches well with the observed precision of the delay anomaly (11.9 m, Table 4.2).

Likely sources of underlying systematic biases and trends in the delay and height anomaly results are the receiver orbit solution, systematic tracking errors, and ionospheric mis-modeling. While the residual orbit error of the receiver (2.6 m) does not map directly into



(a)



(b)

Figure 4.6: Global measured surface heights and height anomalies from TDS-1 data. (a) Measured ocean surface topography with respect to the WGS84 reference ellipsoid. (b) Measured surface height anomaly with respect to the DTU10 mean sea surface.

the path delay, it is likely a significant source for the remaining systematic error effects. In the absence of a position error vector for each measurement, we assume a worst case scenario where the position error is included directly in the delay error budget, Table 4.3. With this assumption we have a conservative estimate of the contribution from orbit precision.

The reflected signal tracking error as a function of correlation SNR has been analyzed. Fig. 4.8 illustrates the estimated tracking error of the reflected signal and the distribution

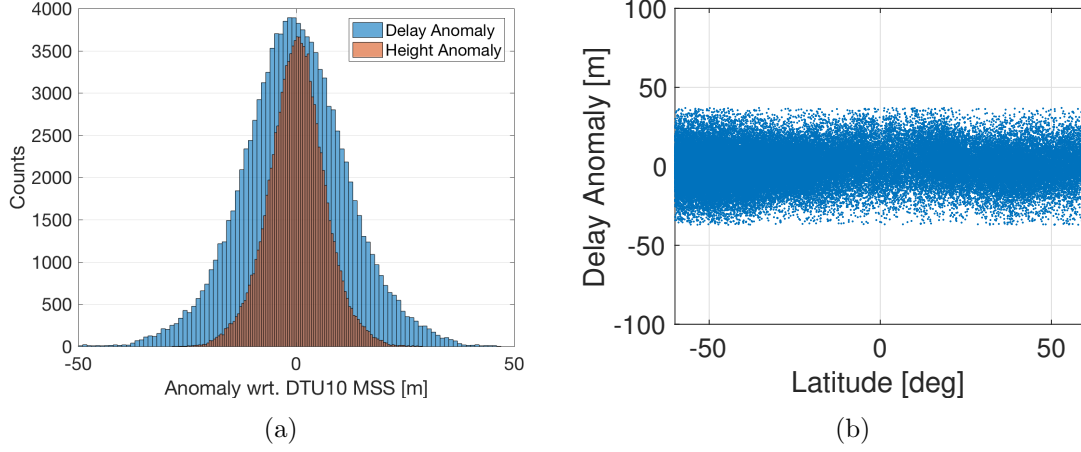


Figure 4.7: Delay anomaly distribution and residual. (a) Histogram of the 1 second average delay anomaly residuals with respect to the tide corrected DTU10 MSS. (b) Delay anomaly residuals from the tide corrected DTU10 MSS shown against latitude.

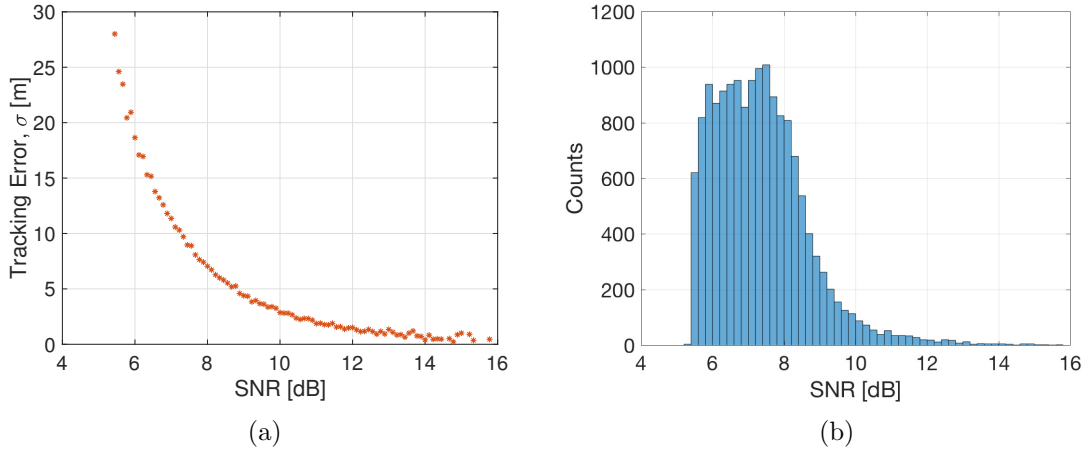


Figure 4.8: Estimated tracking error of the reflected signal as a function of SNR. (a) Estimated tracking error  $\sigma$  of the reflected signal as a function of signal to noise ratio. (b) A histogram of the observed signal to noise ratios of the reflected signals.

of observed correlation SNR values. Our estimate of the SNR dependent tracking error is calculated as described in Section 4.3.1. It can be seen that the mean observed SNR,  $\sim 7$  dB, corresponds to a tracking noise of  $\sim 10$  meter standard deviation. Additionally, some systematic effects may be present. We use the HALF tracking point here which relies on the assumption of having a strongly diffuse reflection from well developed seas. For any regions

of the ocean where this assumption is not valid, systematic errors will be introduced by using the HALF point tracking approach.

We also examined the potential impact of charged and neutral atmospheric effects. Because of the reliance on single-frequency observations, we expected some limitations in performance due to the ionospheric effects. However, in comparing residuals for daytime and nighttime tracks, we see essentially the same residual standard deviation ( $\sigma = \pm 12.8$  m) and a bias difference of only 0.3 m between them. A 35% error in the IRI TEC estimate results in 4 m delay RMS of residual error for daytime tracks and 2.2 m delay RMS of error for nighttime tracks. Tropospheric models have been estimated to perform very well as compared to radiosonde profiles with a residual delay error of  $\sim 5$  cm [Leandro et al., 2006].

Finally, the baseline offset between zenith and nadir looking antennas has been accounted for and the residual error is expected to be small. The typical attitude uncertainty of TDS-1 is approximately 1 degree about each axis. This uncertainty in attitude yields an uncertainty in delay of about 1 mm.

## 4.5 Summary and Conclusions

Our analysis of the TDS-1 data has established that spaceborne GNSS-R is capable of retrieving accurate global ocean altimetry, though as expected, the 1-sec measurement precision on this platform is not adequate for mesoscale oceanography. Based on the currently available data and models, the observed height retrieval precision is  $\sigma_H = 6.4$  meters for 1 second integrations. The results presented here are based on a set of data not originally intended for altimetry, which brings up several challenges in the hardware and software implementation that have been compensated for as comprehensively as possible. Improvements to signal tracking would certainly be obtained through the use of a higher gain antenna and wider signal bandwidth. The use of dual-frequency measurements would reduce the ionospheric error source to well below the required accuracy [Brunner, 1991].

Aside from the limitations imposed by the TDS-1 receiver configuration, there are sev-



eral propagation error model improvements that would yield much improved height retrieval precision. The most significant model improvements would come from better ionospheric corrections and precise receiver orbits. Improvements to these estimated orbits could likely be obtained in the future. Surrey Satellite Technology has indicated they may release the onboard orbit solutions or raw pseudorange measurements. One could then perform more precise orbit determination, directly improving the height retrievals. Finally, incorporating corrections for EM bias and other traditional ocean altimeter errors may give improvements on the order of 0.3 m [Camps et al., 2017; Ghavidel et al., 2016; Hajj and Zuffada, 2003; Li et al., 2016].

Even with an ideal GNSS-R configuration for altimetry, the achievable surface height precision is likely an order of magnitude larger than the current state-of-the-art nadir altimeters (e.g. JASON-2 [NOAA, 2011]). Li, et al. suggest that such a system would require high gain antennas and utilize wide-band ranging codes and dual-frequency signal tracking. Then the achievable height precision for a 1-sec GNSS-R measurement would be on the order of 1 meter. However with appropriate spatial and temporal averaging of measurements from a small constellation of receivers, mesoscale ocean features may still be observable [Li et al., 2016]. As more GNSS-R spacecraft become available (now TDS-1, CYGNSS [Ruf et al., 2016], and SMAP [Carreno-Luengo et al., 2017]) the individual receiving systems are becoming increasingly capable. Future studies should consider direct comparison with in-situ or traditional radar altimeter measurements for validation as GNSS-R data sets expand and the retrievals improve to more comparable levels. With a larger number of higher performance observing platforms, improvements to GNSS signal reflection models (ex. Voronovich and Zavorotny [2018]), and the incorporation of improved altimetric corrections the opportunities will grow for GNSS-R altimetry to provide useful oceanographic observations [Jin et al., 2011].

## Acknowledgment

The work presented here was supported under JPL award #1538217. The authors would like to thank Dr. Clara Chew, Dr. Philip Jales, Dr. Dallas Masters, and Dr. Victor Zlotnicki for their valuable contributions. Dr. Chew helped us identify the source of systematic errors encountered in the TDS-1 dataset. Dr. Jales was invaluable in initially understanding the TDS-1 operations and data sets. Dr. Masters provided us with specular point prediction code and tidal corrections to the mean sea surface. Finally, we would like to thank Dr. Zlotnicki for his helpful input. We appreciate Surrey Satellite Technologies Ltd. making their data from TechDemoSat-1 available to the public at [www.merrbys.co.uk](http://www.merrbys.co.uk).

## Chapter 5

### Modeling GNSS-R Reflections

GNSS-R gained momentum as a viable technique for Earth remote sensing in the late 1990's and early 2000's. Researchers including Clifford et al. [1998]; Garrison and Katzberg [1997, 2000]; Zavorotny and Voronovich [1999] developed instruments to observe and models to analyze the sensitivity of GNSS-R to sea state in the open ocean. In 2000, Zavorotny and Voronovich published one of the first models to describe the diffuse scattering of GNSS signals from the ocean surface. The Zavorotny and Voronovich model predicts the bistatic radar cross section under the assumption that strong diffuse scattering is dominant. They model a relatively rough surface described by wind-driven wave spectrum [Elfouhaily et al., 1997] that gives a large Raleigh parameter,  $R_a \gg 1$ , under which conditions the Kirchhoff approximation can be used.

In 2018, Voronovich and Zavorotny [2018] published an updated theoretical model that expands beyond these limiting assumptions to account for phase coherent scattered power as well. In fact, spaceborne ocean observations with GNSS-R sometimes do exhibit characteristics of weak diffuse scattering with a strong coherent component (Raleigh numbers,  $R_a \leq 1$ ). The following sections describe the Voronovich and Zavorotny [2018] GNSS-R scattering model including coherent and diffuse components, and the modifications made in my work to better represent spaceborne observations from the CYGNSS mission.

### 5.1 Modeling Coherent and Diffuse Scattering

Voronovich and Zavorotny [2018] model the scattered GNSS signal as a function of code delay  $\tau$ , and carrier Doppler shift  $f_D$ , both relative to the specular signal delay,

$$|\overline{Y(\tau, f_D)^2}| = |\overline{Y(\tau, f_D)_c^2}| + |\overline{Y(\tau, f_D)_{nc}^2}|. \quad (5.1)$$

Coherent and incoherent scattering are considered independent components that sum to form the aggregate signal. The overbars in (5.1) indicate an ensemble average. Practically, this is computed as an average over the observation time of a statistical representation of the surface roughness and a model for the transmitted pulses. The reflecting surface is modeled as a collection of angled facets at locations  $\vec{p}$ . The simulated reflection geometry, with vectors  $\vec{m}$  and  $\vec{n}$  connecting the transmitter and receiver to a reflecting element at  $\vec{p}$  on the surface, is illustrated in Figure 5.1. The coherent component in (5.1) is modeled as

$$|\overline{Y(\tau, f_D)_c^2}| = P_T |D_T D_R|^2 \times \langle |X(\tau, f_D)|^2 \rangle \frac{|\overline{V(\hat{n}_*, f_0)}|^2}{R_*^2} \quad (5.2)$$

where  $P_T$  is the transmitted power;  $D_T$  and  $D_R$  are the transmitter and receiver antenna directivities, respectively;  $X$  is the Woodward Ambiguity Function (WAF);  $|\overline{V}|$  is the average reflection coefficient; and  $R$  is the bistatic range between the transmitter and receiver. Parameters with the star subscript, such as  $R_*$ , correspond to the coherent or specular component. The reflection coefficient  $V$  is a function of the vector  $\hat{n}_*$ , the unit vector from the specular point toward the receiver, and the GNSS carrier frequency,  $f_0$ .

Assuming a Gaussian distribution of surface roughness, the reflection coefficient,  $|\overline{V}|$ , can be written in term of the Fresnel reflection coefficient,  $V_F$ , as

$$|\overline{V(\hat{n}, f_0)}|^2 = \exp(-4 R_a^2) |\overline{V_F(\hat{n}_*, f_0)}|^2, \quad (5.3)$$

where the Raleigh parameter is  $R_a = (f_0/c)n_z\langle h^2 \rangle^{1/2}$ . Here,  $c$  is the speed of light,  $n_z$  is the vertical component of the vector  $\hat{n}_*$ , and  $h$  is the characteristic roughness height

of the surface. The coherent scattering coefficient in (5.3) is exponentially dependent on the Raleigh parameter. When the Raleigh parameter gets large, the coherent scattering component of the aggregate signal, (5.1), fades to zero. In practice, the coherent scattered power becomes negligible when the surface-level wind speed, a parameter that drives surface roughness, is greater than 5 m/s.

The angle bars around the WAF are an expected value of the WAF over the observation time,  $T$ , such that,

$$\langle |X(\tau, f_D)|^2 \rangle = \lim_{T \rightarrow \infty} \frac{1}{2T} \int_{-T}^T |X(t, \tau, f_D)|^2 dt. \quad (5.4)$$

The diffuse component of (5.1) is modeled as

$$|\overline{Y(\tau, f_D)_{nc}^2}| = \frac{P_T}{4\pi} \int_A \frac{|D_T D_R|^2}{R_{TS}^2 R_{RS}^2} \times \langle |X(\tau, f_D)|^2 \rangle \sigma_0(\vec{n}, \vec{m}, f_0) d\vec{p}, \quad (5.5)$$

where  $\sigma_0$  is the bistatic scattering cross-section, and  $R_{TS}$  and  $R_{RS}$  are the ranges from the transmitter and receiver to the surface element at  $\vec{p}$ .

The diffuse scattered power given in (5.5) for a specified delay-Doppler pair is the integral of the WAF projected onto the surface and scaled by the radar cross section and antenna directivity. Voronovich and Zavorotny [2018] provide an analytical expression for the bistatic radar cross section when the Raleigh parameter is large,  $R_a \gg 1$ ,

$$\sigma_0(\vec{n}, \vec{m}, f_0) = \pi \left| V_F \left( \frac{\vec{n}_\perp + \vec{m}_\perp}{2}, f_0 \right) \right|^2 \times \left( 1 + \left| \frac{\vec{n}_\perp - \vec{m}_\perp}{n_z + m_z} \right|^2 \right) P \left( -\frac{\vec{n}_\perp - \vec{m}_\perp}{n_z + m_z} \right). \quad (5.6)$$

The vectors  $\vec{m}$  and  $\vec{n}$  are expressed in terms of their horizontal  $n_\perp$ , and vertical  $n_z$ , components.  $P$  is the probability density function of surface slopes. Various models exist to describe the distribution of ocean surface slopes based on the local conditions, including wind speed, swell, etc [Elfouhaily et al., 2002; Elfouhaily and Johnson, 2007; Garrison et al., 2002; Zavorotny and Voronovich, 2000]. When modeling well developed seas in the open ocean, Gaussian statistics are assumed and have been shown to produce good results when compared

to scatterometry measurements. Such a bivariate Gaussian distribution that has the primary axis along the wind direction is used to produce the modeled GNSS-R observations for this work.

The inclusion of coherent scattering in the 2018 Voronovich and Zavorotny model is a significant advancement in modeling the reflection of GNSS signals. This update allows for more representative simulation of scenarios that are encountered in ocean surface observations. It is now possible to model the strongly coherent reflections observed in the CYGNSS measurements. A MATLAB implementation of the model, provided by V. Zavorotny, has been used in this research which will be referred to as VZ18 throughout.

## 5.2 A MATLAB Implementation of VZ18

The MATLAB implementation of VZ18 is configurable to simulate GNSS-R observations from aircraft, spacecraft, or stationary monuments and a wide range of surface conditions as parameterized by wind speed, fetch, and wavenumber range. The generality of this model allows it to be used for simulating the spaceborne observations from CYGNSS. The primary challenges of implementing a model like VZ18 stem from accurately modeling the geometry and reflecting surface in a discrete fashion that can be evaluated in code. In this implementation a specular-point centered coordinate system and a faceted, discrete surface are defined. The surface is discretized in a radial pattern with bins in azimuth and range from the specular point. Figure 5.1 shows how the discretized surface bins are arranged in a radial pattern from the specular point.

While illustrated as function of  $(x, y)$  coordinates in Figure 5.1, the discrete surface grid is not assumed to be planar. A spherical curvature of radius  $R_e = 6.371 \times (10)^6$  meters is used to approximate the Earth surface. The terms in equations (5.2) and (5.5) are evaluated for the contributing facets in the surface grid.

First, the coherent reflected power, described in (5.2), is written as

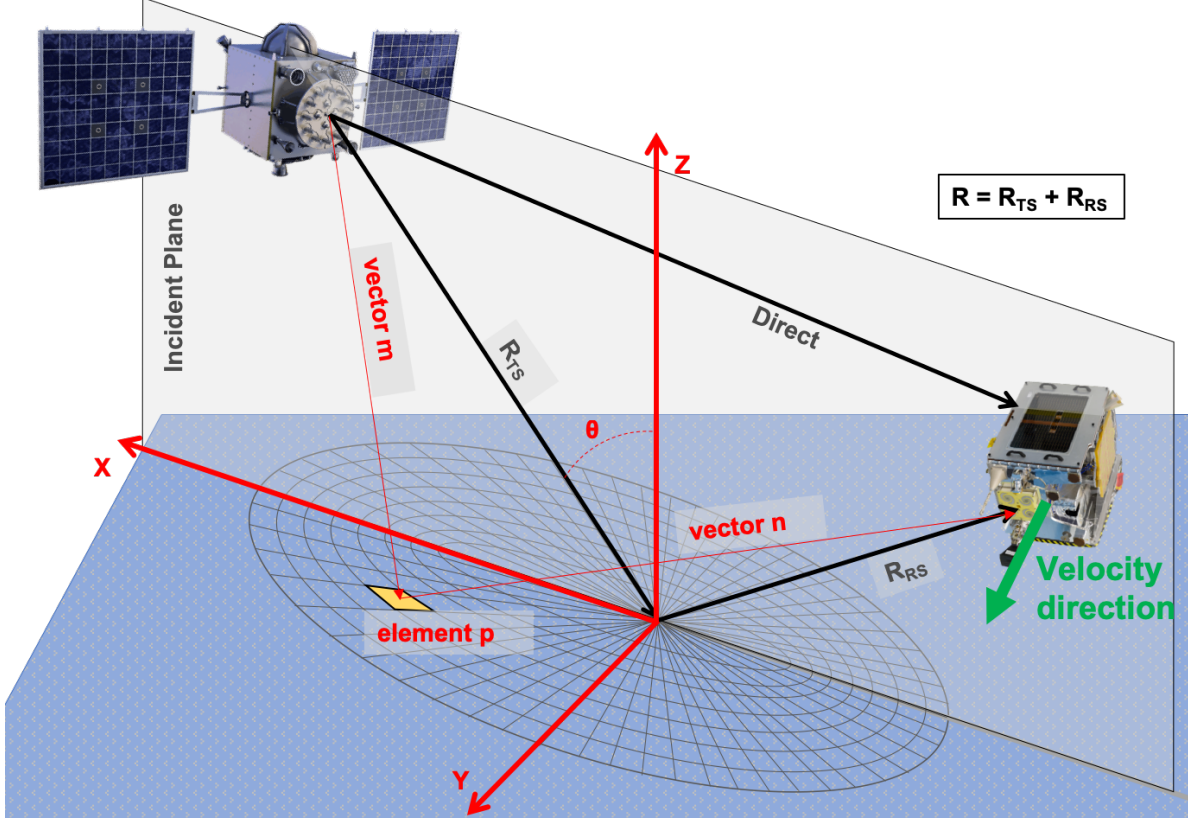


Figure 5.1: Illustration of the radially oriented discrete surface grid utilized in the VZ18 model. The grid origin coincides with the specular reflection point. Discrete cells extend radially from the specular point at fixed azimuth and range intervals. For CYGNSS, the grid extends  $\sim 300$  km in horizontal range from the specular point to capture the significant contributions from the reflecting surface to the resulting GNSS-R DDM. Each element on the surface ( $\vec{p}$ ) contributes to the integral of reflected power that results in the DDM.

$$F_c(\tau_*, f_{D*}) = \frac{P_T G_T G_R X(\tau_*, f_{D*}) \exp(-4 R_a^2) V_F \lambda_{L1}^2}{(4\pi)^2 R^2} \quad (5.7)$$

where

$$V_F = \frac{|b_{1v}|^2 + |b_{1h}|^2 - 2 \operatorname{real}(b_{1v}) \operatorname{conj}(b_{1h})}{4}. \quad (5.8)$$

The variables  $b_{1v}$  and  $b_{1h}$  are Bragg scattering coefficients dependent on the reflecting surface dielectric constant and specular reflecting geometry. The VZ18 model assumes the coherent scattered power is limited to a small area on the reflecting surface near the specular

point. This coherent contribution is considered a point source. That is,  $F_c$  is a scalar, and not summed over a vector of points on the surface. The transmit power, antenna gains, WAF, and scattering coefficients are evaluated only for the specular delay, Doppler, and geometry without integration over the surface.

The diffuse reflected power from a given facet at  $\vec{p}$  with corresponding delay  $\tau$  and Doppler  $f_D$  is written as,

$$F_{nc}(\tau, f_D, \vec{p}) = \frac{X(\tau, f_D, \vec{p}) G_R(\vec{p}) \sigma_0(\vec{p}) r(\vec{p}) \vec{v}_{norm}(\vec{p})}{4\pi R_{TS}(\vec{p})^2 R_{RS}(\vec{p})^2}. \quad (5.9)$$

Here,  $X$  is WAF including the GNSS delay  $\Lambda$  and Doppler  $S$  filters,  $r$  is the radial distance of each facet from the specular point, and  $\vec{v}_{norm}$  is the unit normal vector of each facet. The radial distance and normal vectors are included here to simplify the curved surface integral to an integral over the tangent plane (at the specular point) times the normal.

The WAF ( $X$ ) in (5.7) and (5.9) describes the delay and Doppler selectivity of the GNSS signal cross-correlation. The WAF can be modeled as the product of a delay  $\Lambda$  and Doppler  $S$  filter, that give weighting to the scattered power contribution of each facet on the surface. The WAF is written as

$$X(\tau, f_D) = \Lambda(\tau, \vec{p}) S(f_d, \vec{p}) = \Lambda(\tau, \vec{p}) \frac{\sin(f_d T_i/2)}{(f_d T_i/2)}, \quad (5.10)$$

with

$$\Lambda(\tau) = \begin{cases} 0 & |\tau| > 1 \\ (1 - |\tau|)^2 & |\tau| \leq 1 \end{cases} \quad (5.11)$$

to model the ideal delay filter in the initial MATLAB implementation.

Each component in (5.9) is, in the diffuse case, a function of location on the surface. Therefore, for each delay-Doppler sample in the GNSS-R DDM, a surface integral across the glistening zone accumulates the scattered power contributions. Figure 5.2 illustrates how the delay and Doppler filters, the bistatic radar cross-section, and antenna gain vary



over the glistening zone for an example CYGNSS reflection geometry. The projections in Figure 5.2 correspond to a receiver at 525 km altitude with a specular reflection at 90 deg azimuth with respect to the receiver velocity vector, and 15 deg incidence angle. The delay and Doppler filters are for  $\tau = 1$  C/A chip, and  $f_D = 0$  kHz. As (5.9) shows, the total power in the (1 chip, 0 kHz) delay-Doppler DDM sample will be the integrated product of the components in Figure 5.2 and the remaining terms,  $r(\vec{p})$ ,  $\vec{v}_{norm}$ , and  $R_{TS}(\vec{p})$  and  $R_{RS}(\vec{p})$  from (5.9).

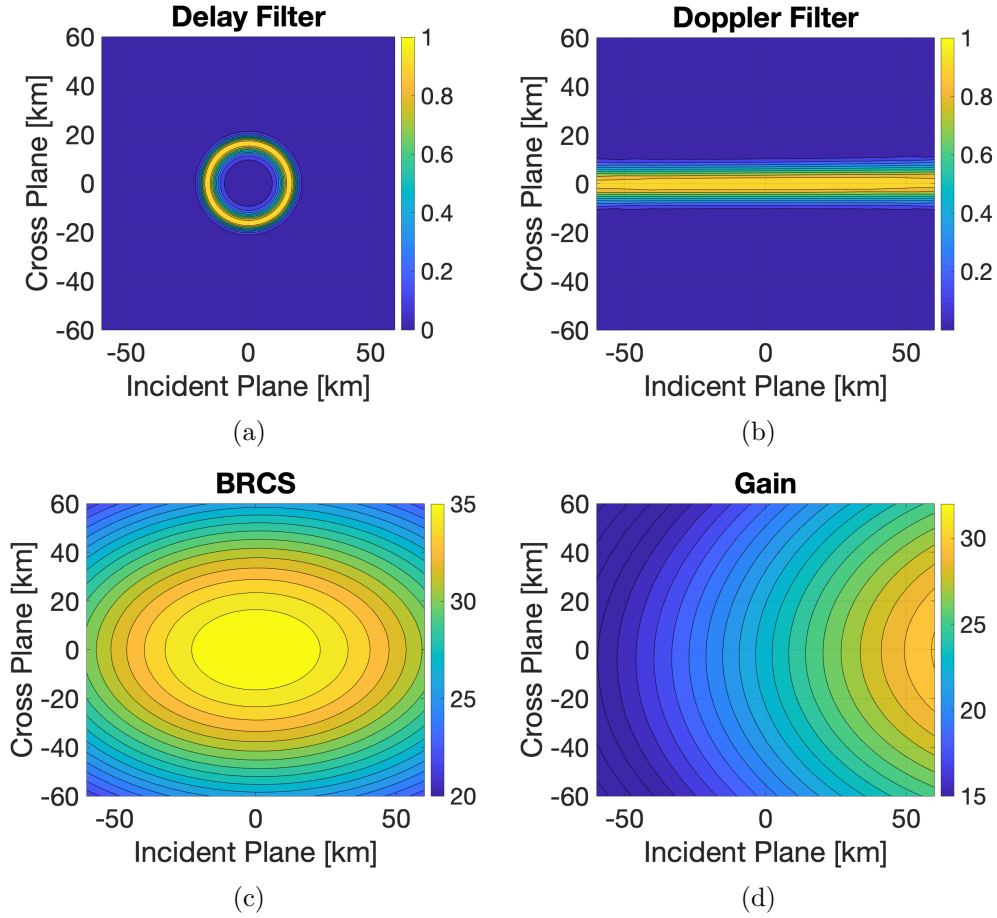


Figure 5.2: Modeled components of equations (5.7) and (5.9) projected onto the reflecting surface. These projections are representative of a GNSS-R receiver in LEO at altitude 525 km. The specular reflection is at a 90 deg azimuth with respect to the receiver velocity direction, and at 15 deg incidence, similarly to the geometry in Figure 5.1. (a) Delay filter for  $\tau = 1$  C/A chip. (b) Doppler filter for  $f_D = 0$  kHz. (c) Bistatic radar cross section in linear units. (d) CYGNSS antenna gain pattern in linear units.

Models of the coherent and diffuse reflected power after cross-correlation and represented in delay and Doppler space are formed in this manner. The final modeled DDM is the sum of the coherent and diffuse components.

### 5.3 Modifications to VZ18

Three limitations in the original VZ18 model implementation are addressed. First, the infinite-bandwidth delay filter is replaced with a bandlimited model. Second, continuous azimuth geometries are modeled. Third, a simplified Gaussian shaped antenna pattern is replaced with the CYGNSS antenna pattern. The modifications applied here are done to better represent observations from the CYGNSS spacecraft, but the same approach can be used to model any other observing systems.

#### 5.3.1 Modeling Limited Receiver Bandwidth

In its original form, the VZ18 model simulates an ideal GNSS-R receiver with infinite bandwidth. The idealized auto-correlation delay filter has the form of a triangle squared, described in (5.11), resulting from the cross-correlation of two perfectly rectangular chips. In evaluating flight data from CYGNSS, we found that this does not match well with the bandlimited observations of a real receiver. For example, the CYGNSS receiver bandwidth of 2.5 MHz [Ruf et al., 2016] results in rounding of the idealized correlation function and modifies the shape of the resulting DDM.

To more accurately represent real, spaceborne observations, a bandlimited delay filter was created and substituted into the VZ18 model. The bandlimited delay filter was empirically derived by comparison to examples of CYGNSS direct signal auto-correlation measurements. Andrew O'Brien from The Ohio State University provided realizations of the GPS direct signal auto-correlation as sampled by CYGNSS. The OSU utilized their engineering model to generate these direct signal DDMs that are not available from the flight receiver in orbit.

The sampled direct signal auto-correlations were used as models to evaluate the CYGNSS bandlimiting effect on the ideal auto-correlation function. The measured direct signal waveforms were compared to synthetic, bandpass filtered versions of (5.11) with bandwidths between 2 – 3 MHz. A simulated waveform with bandwidth  $BW = 2.78$  MHz was found to match the CYGNSS direct signals most closely. Figure 5.3 shows the CYGNSS direct signal waveform and the matching bandlimited waveform. This 2.78 MHz bandlimited waveform is now used as the delay filter when generating models for altimetry retrievals with the CYGNSS datasets.

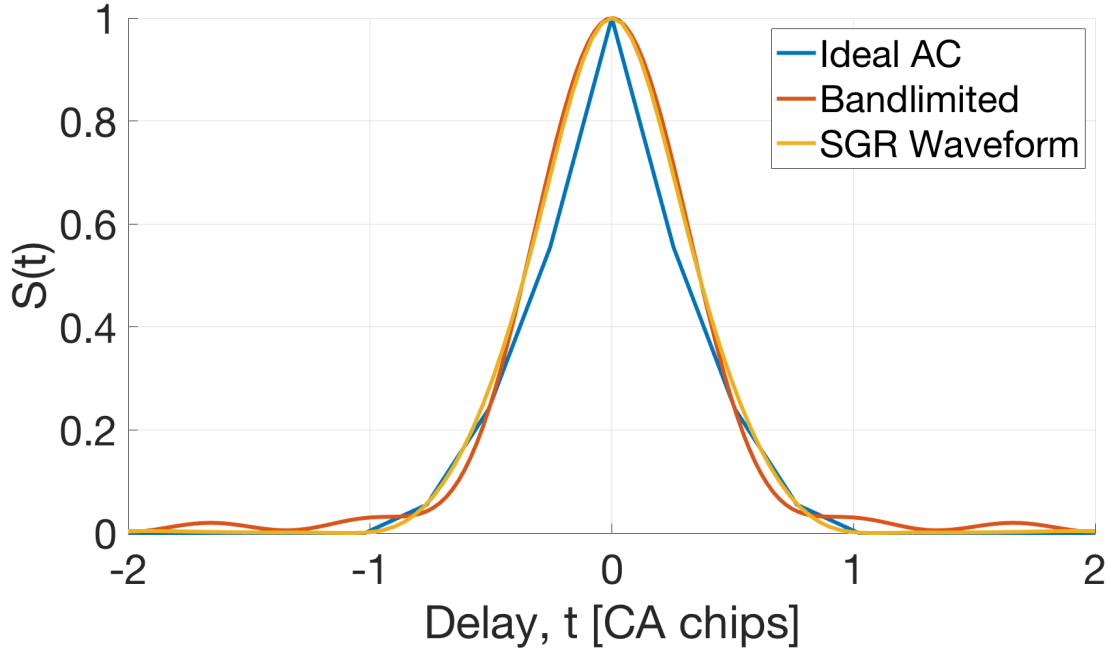


Figure 5.3: Modeling the CYGNSS bandlimited waveform. Autocorrelation models used in the VZ18 models. The ideal autocorrelation model is bandpass filtered to match closely the CYGNSS receiver configuration. A bandpass filter of 2.78 MHz is used in the final implementation of the VZ18 models for CYGNSS.

### 5.3.2 Modeling Continuous Azimuthal Geometries

The projection of the receiver and transmitter velocity vectors onto the reflecting surface was initially constructed for only four discrete cases - the receiver and transmitter flying

in parallel or perpendicular directions, and only either at 0 deg or 90 deg azimuth from the receiver velocity direction. Projection of the receiver and transmitter velocity vectors onto the model surface is used to predict the Doppler contours across the glistening zone. To accomplish realistic flight geometries I added capabilities to simulate all azimuthal geometries that a real GNSS-R receiver can be expected to see. Equations (5.12) and (5.13) show the decomposition of the transmitter velocity ( $\vec{u}$ ) and receiver velocity ( $\vec{v}$ ) onto the reflection plane coordinates centered on the specular point. The transmitter velocity is decomposed into

$$\begin{aligned} u_x &= -i_{dt} u \cos(\alpha_0) \cos(\phi_a) \\ u_y &= i_{dt} u \cos(\alpha_0) \sin(\phi_a) \\ u_z &= -i_{dt} u \sin(\alpha_0), \end{aligned} \tag{5.12}$$

where  $u$  is the velocity magnitude,  $i_{dt}$  is a coefficient, either 1 or  $-1$ , to specify if the transmitter is flying towards or away from the specular point,  $\alpha_0$  is an angle away from the local horizontal of the transmitter velocity with respect to the specular point, and  $\phi_a$  is the azimuth of the reflection as seen by the receiver. The azimuth angle is taken counter-clockwise from the receiver velocity direction. The receiver velocity is decomposed into

$$\begin{aligned} v_x &= -i_{dr} v \cos(\alpha) \cos(\phi_a) \\ v_y &= i_{dr} v \cos(\alpha) \sin(\phi_a) \\ v_z &= -i_{dr} v \sin(\alpha). \end{aligned} \tag{5.13}$$

This decomposition into the VZ18 coordinate frame (Figure 5.1) allows one to simulate a continuous range of geometries from all azimuths and properly calculate the Doppler contours on the surface.

### 5.3.3 Modeling the CYGNSS Antenna Pattern

Several generic antenna patterns were included in the original VZ18 model implementation. The measured CYGNSS antenna patterns (shown in Figure 5.4) were adapted and included into the model to produce more accurate representations of the real observations.

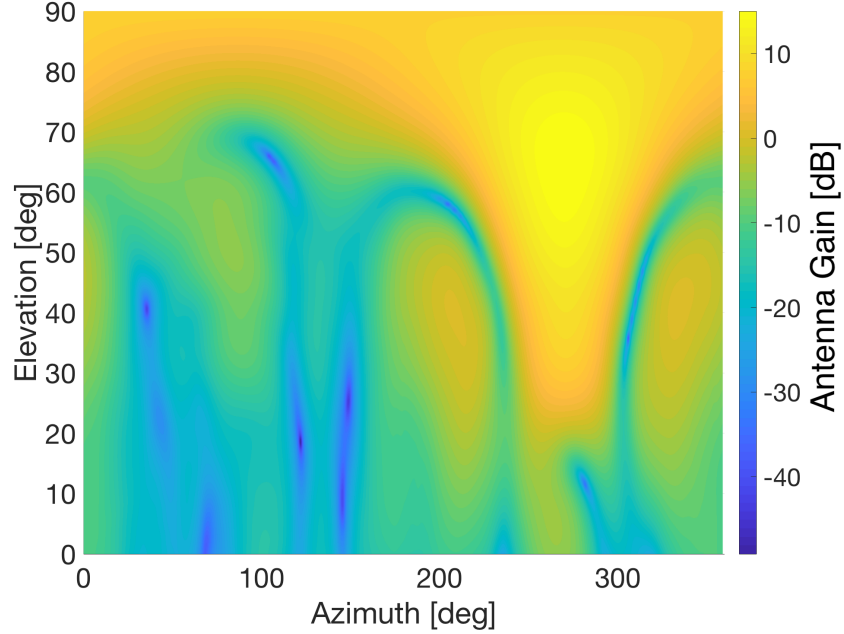


Figure 5.4: Measured CYGNSS antenna pattern. CYGNSS port antenna pattern plotted against the spacecraft body frame azimuth and elevation. In the CYGNSS body frame, azimuth is measured counter-clockwise from the  $+x$ -axis which is oriented along the major axis of the spacecraft and nominally aligned with the velocity direction. Elevation is measured from the body  $x-y$  plane (ie. the local horizontal) and toward the  $-z$ -axis or nominal nadir direction. The CYGNSS antenna are oriented such that the beam boresight is 28 deg away from nadir and at  $\pm 90$  deg (port and starboard) from the velocity direction.

Correct modeling of the receiver antenna pattern has been found to be an essential part of creating accurate and representative modeled DDMs. Especially in the CYGNSS case with two (port and starboard) side-looking antennas, the weighting introduced by the gain pattern can yield a large asymmetry in Doppler in the DDMs. Figure 5.5 illustrates how the receiver antenna pattern differentially scales contributions from across the Doppler axis as a function of the reflection azimuth angle away from the antenna boresight direction.

In the case of CYGNSS, there are two, side-looking antennas that point 28 deg off nadir at azimuths 90 deg and 270 deg from the nominal satellite velocity direction. DDMs for reflections to the fore and aft of CYGNSS will have more asymmetry in Doppler than those from directly side-looking geometries.

Figure 5.4 shows the measured CYGNSS port antenna pattern. A similar starboard pattern is utilized as well when the observation geometry requires. Unfortunately, the only antenna patterns measured for CYGNSS were a single pair of port/starboard patterns mounted on an engineering model of the spacecraft bus. The full contributions of the actual spacecraft bus and any unique differences among the antennas across all 8 CYGNSS spacecraft are not known. It is expected that the measured antenna patterns that are available should properly account for the majority of the antenna gain scaling in the VZ18 model.

#### 5.4 Model Representations of CYGNSS GNSS-R Data

The modified VZ18 model is used to retrieve specular reflection delays from CYGNSS observed DDMs. An example least-squares model-measurement DDM fit is presented in Figure 5.6 to illustrate how the VZ18 GNSS-R signal model can simulate real, spaceborne observations. The Doppler asymmetry, resulting from the CYGNSS antenna pattern, is captured well in the model DDM. The measured DDM (Figure 5.6 right) is shown with the retrieved specular delay and Doppler values. The original zero delay and Doppler alignment from the CYGNSS open-loop tracking is illustrated with red dashed lines. With the delay and Doppler offset applied, the qualitative agreement between measured and modeled DDMs can be seen.

There are some limitations associated with the current implementation of the VZ18 model that should be mentioned. For now, only the Elfouhaily et al. [1997] wind-driven wave spectrum is used to model surface roughness. Other surface effects, such as swell, are not modeled; therefore the surface roughness model is limited in its ability to fully represent the complete sea state. Further, the CYGNSS observation geometry is approximated in

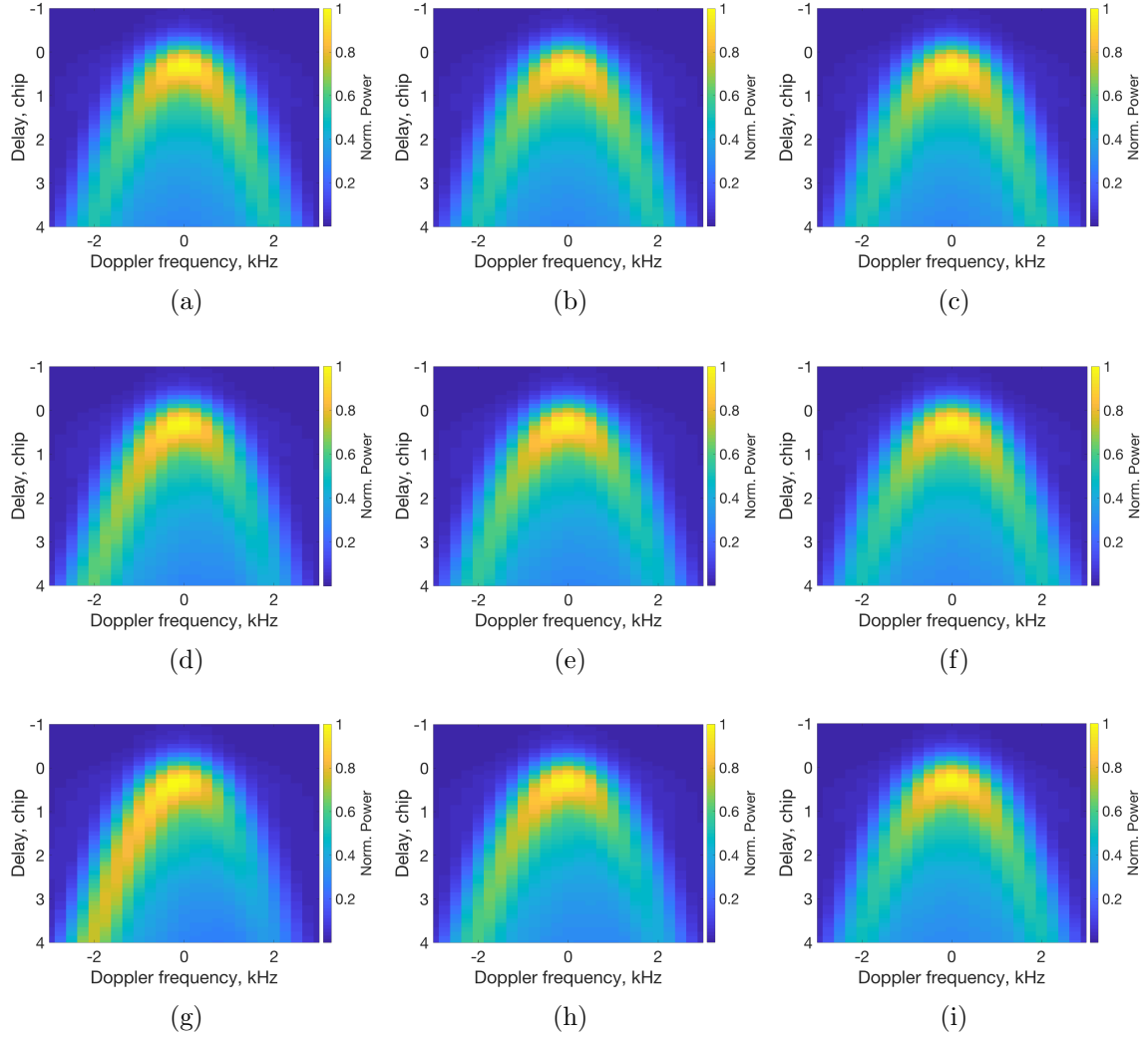


Figure 5.5: Modeled effect of the receiver antenna pattern on the DDM. (a)-(c) Synthetic DDMs created with an isotropic antenna pattern for reflection azimuths  $\alpha = 0$  deg, 60 deg, and 90 deg. (d)-(f) Synthetic DDMs created with a Gaussian shaped antenna pattern for reflection azimuths  $\alpha = 0$  deg, 60 deg, and 90 deg. (g)-(i) Synthetic DDMs created with the CYGNSS antenna pattern for reflection azimuths  $\alpha = 0$  deg, 60 deg, and 90 deg. Each model has an incidence angle of  $\theta = 15$  deg, receiver height  $h_R = 525$  km, and surface-level wind speed  $ws = 8$  m/s. Figures (a), (d), and (g) show reflections from directly fore of the receiving spacecraft. Figures (c), (f), and (i) show reflections from the starboard side of the spacecraft (and in the direction of the antenna boresight).

the model using an average receiver altitude, and a set of discrete incidence and azimuth angles. Finally, the CYGNSS receiver bandwidth effect is approximated through the use of a bandlimited auto-correlation model. These limitations will have a real effect on how

well the VZ18 modeled DDMs represent CYGNSS observations. The extent to which these limitations affect the VZ18 model fitting is explored further in the following two chapters.

Two delay re-tracking algorithms, VZ18WAVE and VZ18DDM, have been implemented for the measurement of altimetry delays. Both algorithms are covered in detail in Chapter 6. Altimetry results that utilized these methods with the CYGNSS data are then presented in Chapter 7.

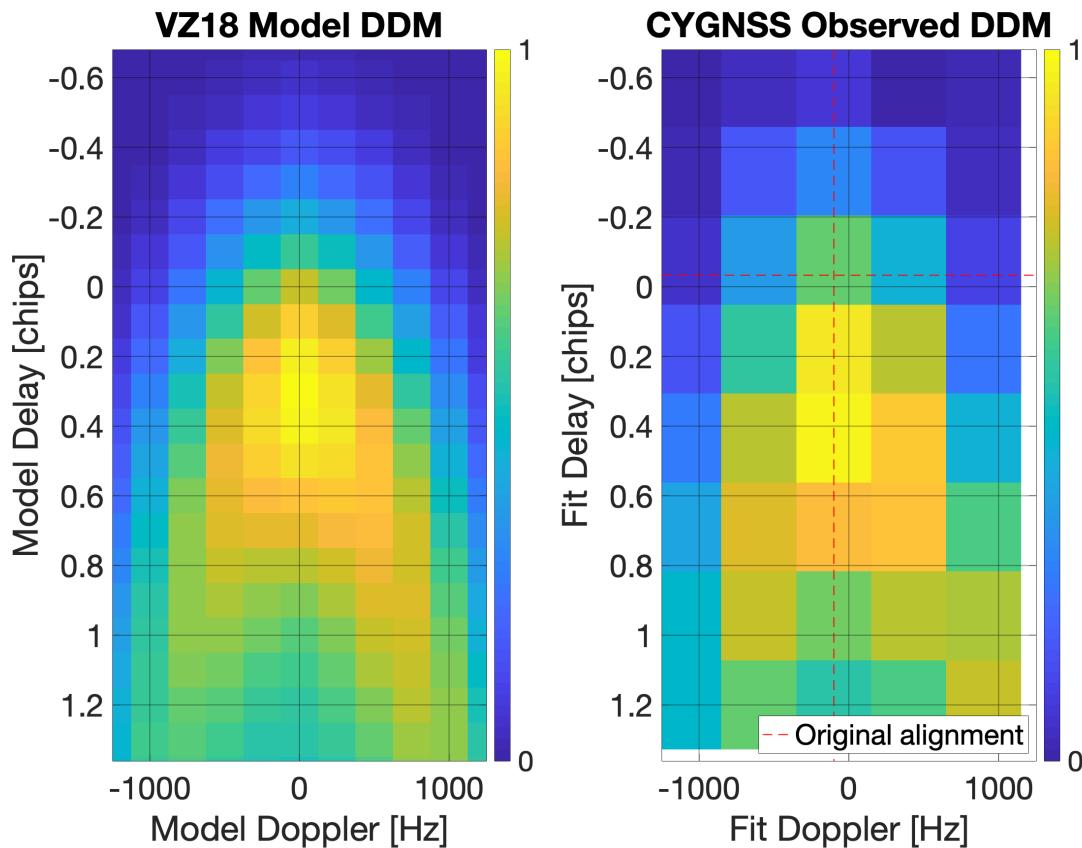


Figure 5.6: Example VZ18 model fit with an observed DDM from CYGNSS. Observation azimuth 102 deg, incidence 45 deg. Model azimuth 100 deg, incidence 45 deg. (left) A simulated VZ18 DDM with fine sample resolution. (right) A CYGNSS observed DDM at the CYGNSS sample resolution aligned to fit the VZ18 model by a least-squares fit. The CYGNSS predicted delay and Doppler are marked with red dash lines. The asymmetry in Doppler imposed by the antenna pattern is visible in both the simulated and observed DDMs.



## Chapter 6

### GNSS-R Altimetry Methods

Methods to retrieve ocean surface heights with conventional spaceborne GNSS-R are presented in this chapter. These techniques were developed incrementally through the analysis of airborne and spaceborne data sets. Earlier versions of the methods presented in this chapter were used in the analysis of airborne GNSS-R data from Monterey Bay, California (Mashburn et al. [2016], Chapter 3) and spaceborne data from the TechDemoSat-1 mission (Mashburn et al. [2018], Chapter 4). An analysis of CYGNSS observations in Indonesia that makes use of the improved techniques is presented in Chapter 7.

The development of methods to extract the highest quality altimetric retrievals from non-optimized flight data has been one of the primary aims for the research presented in this dissertation. These techniques are practical and were created to be modular and as generally applicable as possible. Keeping that in mind, the missions considered in this dissertation to characterize the performance of GNSS-R altimetry were not optimized to make altimetric measurements but still serve a useful purpose. Altimetry optimized, spaceborne GNSS-R sensor systems are not yet in operation. However, a few small-scale independent experimental campaigns for altimetry have been attempted [Carreno-Luengo et al., 2013; Fabra et al., 2012; Lowe et al., 2000; Semmling et al., 2013]. This is the challenge undertaken at the outset of this work and the context within which it was completed.

The use of monostatic radar soundings to make precise ocean surface height measurements is already well established [Chelton, 2001]. Figure 6.1 shows the key surface definitions

used in altimetry studies: the reference ellipsoid, mean sea surface, and sea level anomaly (SLA). The reference ellipsoid (ie. the WGS84 ellipsoid) is a geometric approximation of the earth's equatorially bulging shape. The geoid (not shown) is a model surface of equal gravity potential. The mean sea surface (MSS) closely follows the geoid and is a multi-year average sea surface topography derived from decades of continuous radar altimetry measurements [Andersen et al., 2015]. Sea level anomaly (SLA) is the instantaneous difference between the real sea surface and the MSS. The SLA is the quantity of interest for ocean surface altimetry.

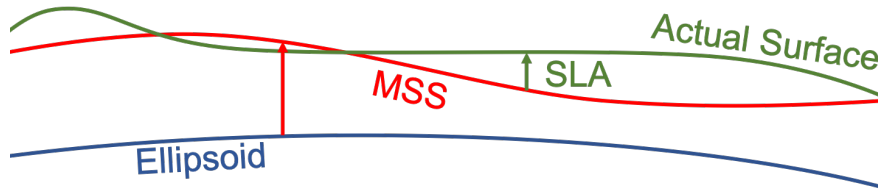


Figure 6.1: Illustration of some common traditional altimetry terms. Green represents the instantaneous sea surface.

The following sections present methods to form the altimetric measurement. First, we discuss mapping measured delays to surface heights. Second, methods to compute the altimetric delay are presented. Finally, we outline a path-delay model that considers the systematic error sources we have encountered.

## 6.1 Mapping Path Delay to Reflector Height

Three key features of the DDM are its shape, amplitude, and time delay (or path delay when multiplied by the speed of light) relative to the direct signal tracking. Determining the time delay of the specular reflected signal with respect to the tracked direct signal, allows retrieval of a relative surface height [Garrison and Katzberg, 2000]. This excess path delay, of the specular ray with respect to the direct ray, is determined by measuring the delay of the

correlation function recorded in the DDM,  $\delta_{measured}$ . The process of forming the altimetry delay measurement, called re-tracking, is covered in the following section. The specular point delay is used as the reflected signal track point, because it can be readily modeled and is less sensitive to roughness than the delay of the peak power or other possible track points on the waveform.

To solve for sea level anomaly, measured delays are compared to modeled delays. We form a precise delay model that accounts for systematic errors,

$$\delta_{modeled} = (R_R - R_D) + \delta_{iono} + \delta_{tropo} + \delta_b, \quad (6.1)$$

where  $(R_R - R_D)$  is the excess geometric range between the reflected and direct paths,  $\delta_{iono}$  is the ionospheric delay,  $\delta_{tropo}$  is the tropospheric delay, and  $\delta_b$  represents other delay terms like antenna baseline and instrument specific considerations. Each term in (6.1) is described in detail in subsequent sections of this chapter.

The measured delay is compared to the delay model to form the delay anomaly  $\Delta\delta$  defined as,

$$\Delta\delta = \delta_{measured} - \delta_{modeled}. \quad (6.2)$$

Delay anomaly (here in units of distance) is mapped into height anomaly  $\Delta h$  from the modeled surface by

$$\Delta h = \frac{\Delta\delta}{2 \cdot \cos(\theta)} \quad (6.3)$$

where  $\theta$  is the reflection incidence angle. This trigonometric relationship is derived by assuming that (a) the transmitter is far enough away that the incoming ray paths can be considered parallel, and (b) the reflecting surface is flat. Neither assumption is completely valid when considering the total excess path delay to a receiver in low Earth orbit. However, for the purpose of mapping range anomalies to height anomalies, the simplified mapping

function is quite sufficient, introducing errors  $\leq 1$  mm in height. To quantitatively assess the height mapping equation (6.3), artificial reflectors were simulated above the WGS84 ellipsoid at known height intervals. Assuming a perfect delay measurement, the delay anomalies between the artificial reflector and the ellipsoid model were mapped to height anomalies. The error between the “measured” height anomaly and the known height displacement of the artificial reflector is shown in Figure 6.2. A range of reflecting geometries were simulated between incidence angle 40 – 80 deg.

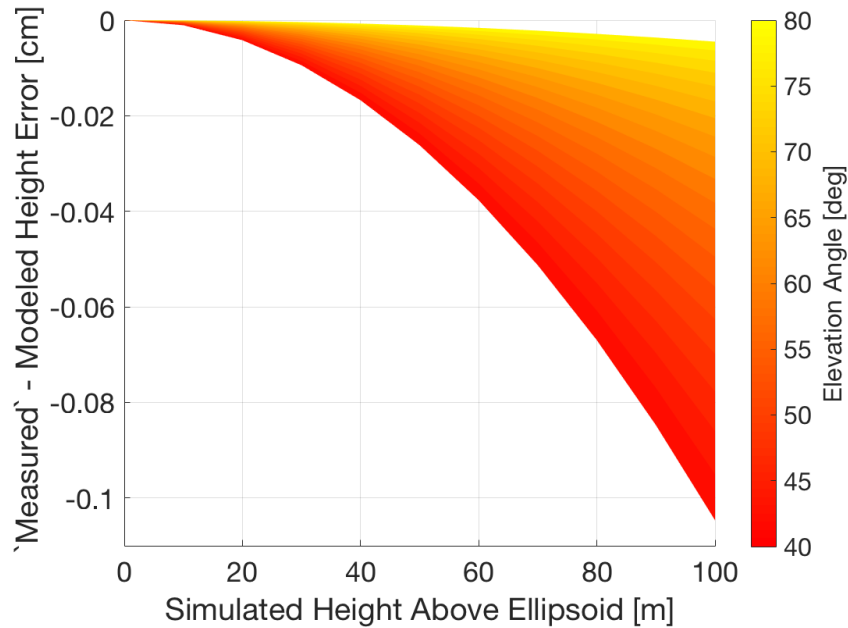


Figure 6.2: Estimated error from linearized delay to height mapping. The height retrieval error is limited to  $\sim 1$  mm for ellipsoid heights less than 100 m and incidence angles  $> 40$  deg. The mean sea surface dynamic range is limited to about  $\pm 100$  m with respect to the WGS84 ellipsoid.

## 6.2 Altimetric Delay Re-tracking

Delay re-tracking is the process by which the altimetric delay measurement is formed from the raw observable, in this case the GNSS-R DDM. Re-tracking is done by computing the range difference between the observed DDM signal and the predicted specular reflection

range. Measuring the delay (range) of the observed DDM signal requires that we make a choice about which point on the signal to track. Methods that have been implemented will track the DDM signal peak, the DDM leading edge half-power point (or other power levels), the leading edge maximum first derivative; or alternatively, retrieve altimetric delay by comparison of the observation to models. A comparison of re-tracking methods for GNSS-R altimetry has been presented in Mashburn et al. [2016], and Cardellach et al. [2014] among others. Here, we consider one single-point method and two model-based methods that make use of the Voronovich and Zavorotny [2018] DDM model.

### 6.2.1 Single Point Re-trackers

Single-point re-trackers are simple and efficient. Under the right reflection conditions, where the assumptions used to choose a tracking point are satisfied, single-point re-trackers can provide precise results. The precision of the delay is subject to the noise characteristics of the dataset. If the single-point tracker assumptions are invalid, large systematic errors arise. For example, tracking the maximum first derivative on the DDM leading edge assumes strong diffuse scattering from well-developed seas [Hajj and Zuffada, 2003]. Mashburn et al. [2016] and Cardellach et al. [2014] demonstrate and compare three different point re-trackers. In both studies the P70 (named HALF in those earlier studies) point was found to outperform the others. Thus, only the P70 point will be discussed here.

A specular delay measurement is typically constructed from an integer number of 1 msec incoherently integrated DDMs. Point re-trackers use a delay waveform taken from the DDM at the specular reflection Doppler offset. The delay waveform is a slice along the delay axis of the DDM resulting in a one-dimensional correlation function as seen in Fig. 6.3. Using P70, point on the leading edge of the correlation waveform at 70% of maximum power is tracked. The 70% power level is not, however, tied in any physical way to the specular reflection. Thus, a measurement bias is introduced with some dependence on the surface conditions. Proper considerations that restrict observations to well developed seas, with

strong diffuse scattering, at high elevation angles, should result in a constant bias for P70 that can be effectively calibrated.

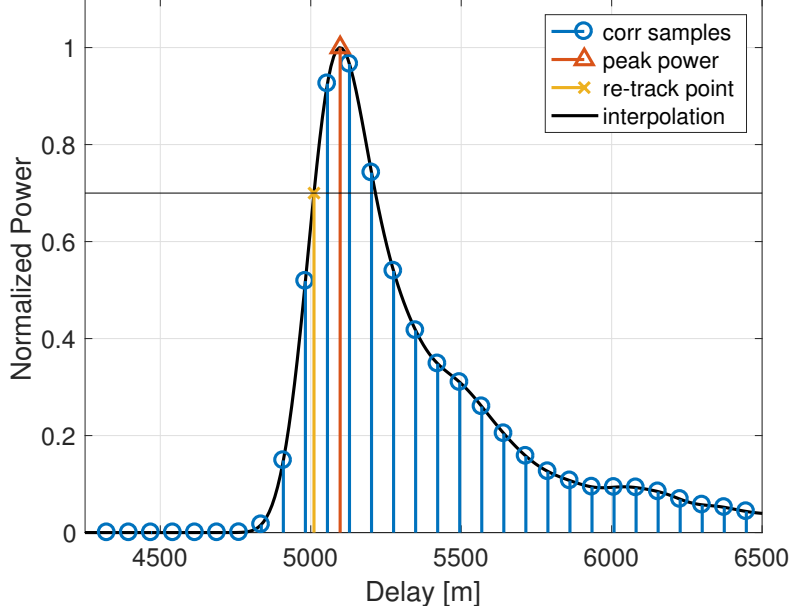


Figure 6.3: Example of P70 point tracking on a measured waveform. First, the noise floor is determined by the average correlation value of the first  $M$  samples (not shown) and removed.  $M$  may vary and is specific to the data set being used. The correlation waveform is then normalized by the peak power and the 70% tracking point is determined.

Tracking a point on the GNSS-R correlation waveform requires interpolation between samples and a normalized waveform. To do this, the noise floor is first estimated by averaging correlation values of the first  $M$  samples where no reflection signal is expected to be present. The number of noise samples available depends on the dataset - for TDS-1  $M = 20$ ; for CYGNSS  $M = 4$ . The noise floor is then subtracted from the correlation measurements and the waveform is normalized to a peak power of 1. A Whittaker-Shannon interpolation of the adjusted correlation measurements is used to determine the desired points, as follows,

$$x(\delta) = \sum_{n=-\infty}^{\infty} x[n] \cdot \text{sinc}\left(\frac{\delta - nd}{d}\right) \quad (6.4)$$

where  $x[n]$  are the normalized correlation samples after the noise floor has been re-

moved,  $\delta$  is continuous delay, and  $d$  is the sampling period. Newton's method is applied to first locate the peak power point on the waveform and then the 70% re-track point.

### 6.2.2 Re-tracking in the Presence of Coherent Measurements

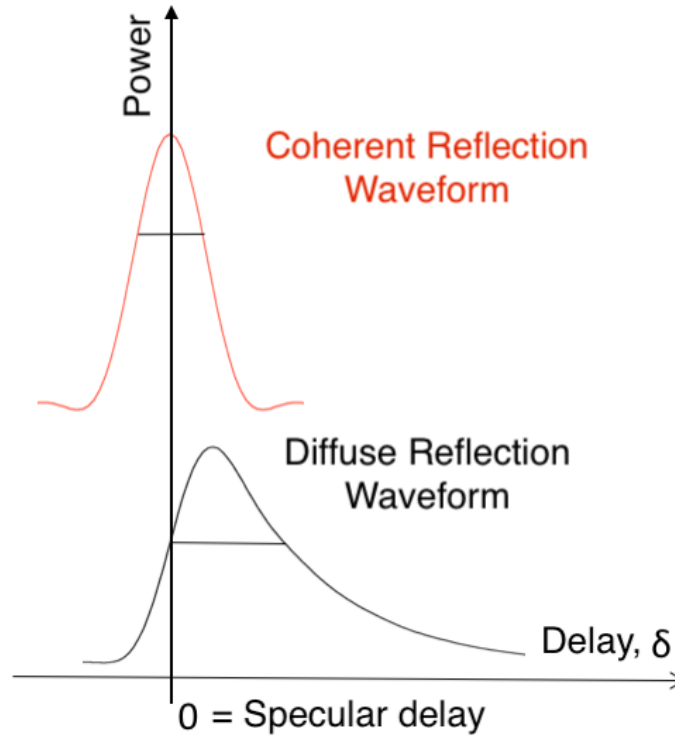


Figure 6.4: Illustration of the change in specular reflection tracking point on coherent and diffuse waveforms. The true specular tracking point of a GNSS-R delay waveform depends on the reflection coherence.

For moderate incidence angles in the open ocean, the assumption of strong-diffuse scattering is typically valid. There are, however, a significant number of observed cases where this assumption fails in the experimental data sets we have available. We found as many as 4% of the CYGNSS observations in a given day exhibit coherent reflection characteristics. If a single-point re-tracker is used, a calibration should be applied to compensate for the systematic biases introduced once the strong-diffuse scattering assumptions fail.

Figure 6.4 illustrates how the true specular track point on the delay waveform differs

between fully coherent and diffuse observations. A completely coherent reflection will be an auto-correlation waveform since only the first Fresnel zone on the surface, which is small, contributes to the observed power distribution. As the reflecting surface roughness increases, and the diffuse reflected power increases, the delay waveform takes on the characteristic extended trailing edge shape. The location of the “zero”, or specular, delay moves down the waveform leading edge between the coherent and diffuse cases. The expected single-point re-track delay error varies as a function of the chosen track point (e.g. 70% versus 50% maximum power). For example, the expected tracking error of a fully coherent reflection measured with the P70 method is 75 m ( $\sim 0.25$  C/A chips). A more subtle effect is also dependent on the receiver bandwidth. Bandwidth affects the slope along the rising and trailing edges of an observed GNSS-R waveform and therefore the re-tracking delays as well.

Observed GNSS reflections are not discretely either coherent or diffuse as illustrated in Figure 6.4. Instead, real GNSS-R observations lie on a spectrum between the two extremes. The challenge is that neither the TDS-1 nor the CYGNSS DDMs contain information about the reflected signal phase. Therefore, it is impossible to perfectly quantify the phase coherence of each observation. There are observable characteristics of each DDM, however, that can indicate if a measurement contains a strong coherently-scattered component. The delay waveform width and correlation SNR are found to be strong indicators of coherence. We measured the waveform width at the 70% power level of the delay waveform. Correlation SNR is defined as

$$SNR = \frac{P_{max} - P_{noise}}{\sigma_{noise}}, \quad (6.5)$$

(same as 4.12).

Figure 6.5 shows the variation of P70 delay anomaly with correlation SNR and delay waveform width. Clearly there is a systematic relationship between delay anomaly and the waveform width and correlation SNR. From Figure 6.5, SNR appears to be primarily an



indicator of measurement quality. That is, measurements with higher SNR tend to have delay anomaly closer to zero. Waveform width appears to be indicative of reflection coherence. More narrow waveforms tend to have delay anomaly systematically biased to the negative. This behavior is consistent with the expectation for coherent observations tracked by a fixed point method.

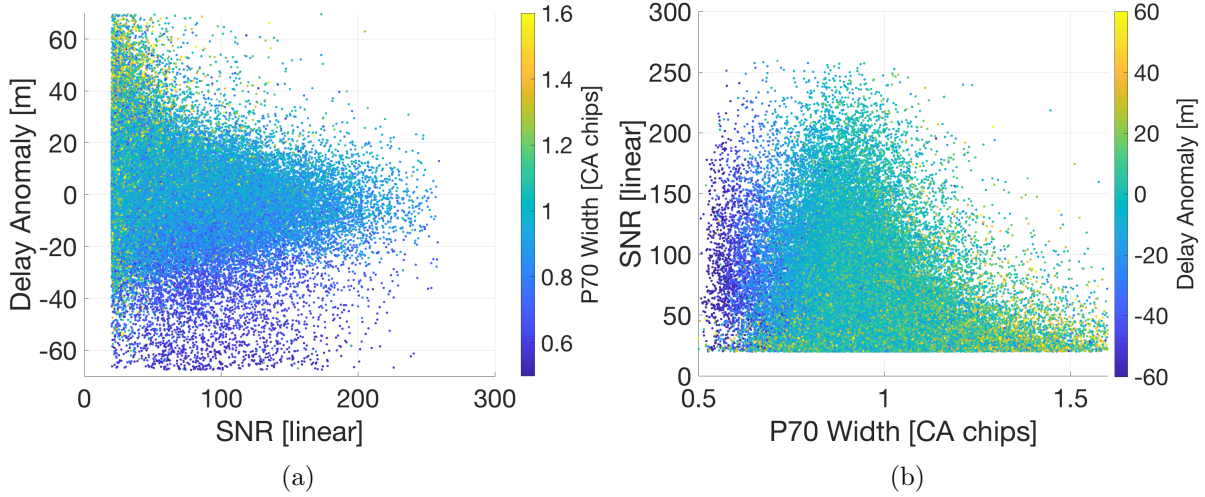


Figure 6.5: Measured P70 delay anomaly correlation with SNR and waveform width. (a) Measured - modeled delay anomaly versus correlation SNR. Colors represent correlation waveform width. There is a visible relationship between delay anomaly (P70 tracking) and waveform width, while correlation SNR is indicative of delay anomaly precision. (b) Correlation SNR versus waveform width. Colors represent delay anomaly (P70 tracking). Narrow waveforms tend to have high SNR.

A discrete classification approach may be used to handle coherent reflection tracking with single point re-trackers based on the expectations illustrated in Figure 6.4. Placing thresholds on the correlation SNR and waveform width metrics divides the CYGNSS observations into discrete cases of coherence. Each case can be re-tracked with the appropriate choice of tracking point. For example, we considered a binary classification to divide the data into coherent and incoherent groups. The waveform peak track point is used for coherent cases with width  $< 0.6$  chips, and the P70 method is used for incoherent cases with width  $\geq 0.6$  chips.

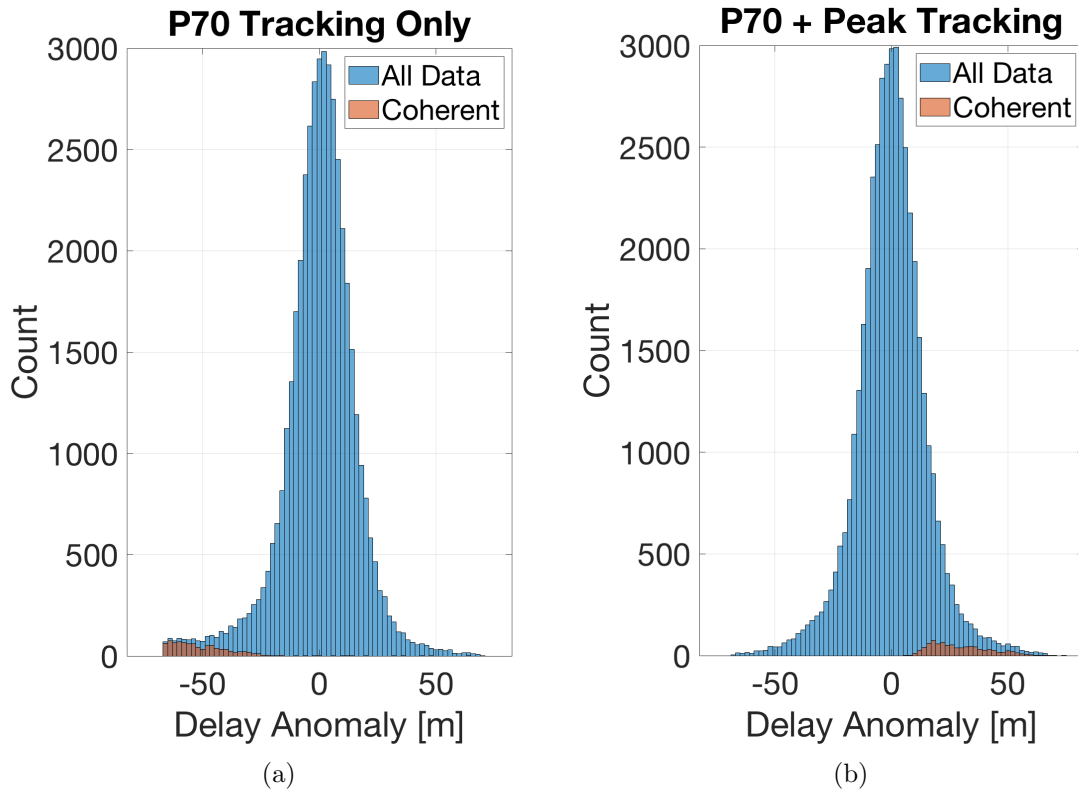
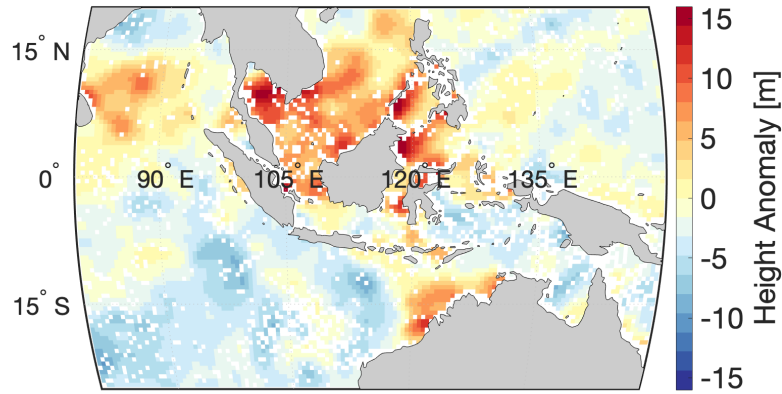


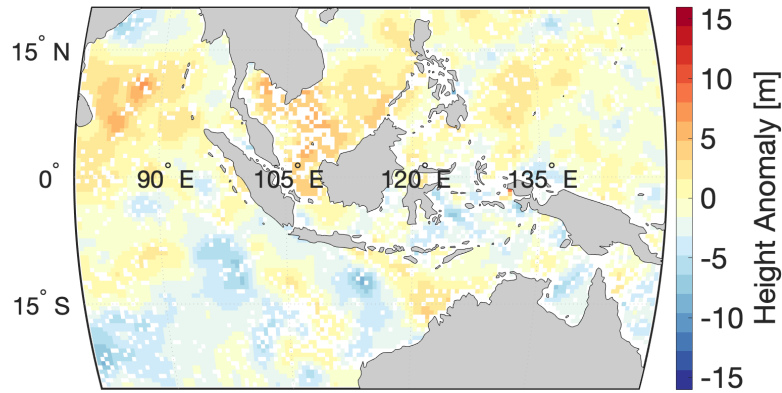
Figure 6.6: Delay anomaly distribution with and without consideration of coherent reflections using PEAK tracking. CYGNSS measurements from Indonesia exhibit both coherent and incoherent-like characteristics. (a) If P70 tracking is used to track all cases, a skewed distribution in delay anomaly is observed (blue). Those points classified as coherent-like by their width and SNR, are highlighted over in red. (b) If instead the coherent-like measurements are tracked by the peak of the correlation function, the delay anomaly distribution is more symmetric, and well distributed. However, this binary treatment leaves a discontinuity in the delay anomaly. Again the coherent-like observations are highlighted in red.

Figure 6.6 shows how the binary treatment of coherence influences the delay anomaly. If all of the measurements are treated as incoherent there is an obvious skew in the distribution of delay anomaly (blue histogram in Figure 6.6(a)). Instead, if the coherent measurements are tracked by the peak, the result is much closer to a Gaussian distribution (blue histogram in Figure 6.6(b)). Figure 6.7 illustrates the effect in height anomaly around Indonesia as computed with CYGNSS observations from August 2017. Many of the large systematic height signals are clearly and significantly reduced by this binary approach.

Unfortunately, while the binary coherence treatment reduces the delay anomaly bias



(a)



(b)

Figure 6.7: Height anomaly retrievals in Indonesia with and without considering coherent reflections by PEAK tracking. Smoothed height anomaly retrievals in Indonesia from 5 days of CYGNSS data, d230-234 2017. All available CYGNSS spacecraft are included here. (a) Re-tracking all measurements with P70 method. (b) Re-tracking coherent-like measurements with PEAK and incoherent measurements with P70. Many of the systematic patterns in the delay anomaly retrievals appear to be corrected when the coherent-like measurements are tracked with PEAK.

observed with coherent returns, it creates a discontinuity in the delay anomaly at the width threshold as seen in Figure 6.8. Clearly, there are a significant number of observations in a transition zone, with waveform width between 0.6–0.8 chips, that are not tracked correctly, and the peak tracking is too high. Figure 6.8 illustrates the primary difficulty of choosing



Figure 6.8: P70 + PEAK delay anomaly plotted against waveform width. Measurements classified as coherent are tracked with PEAK while incoherent measurements are tracked with P70. A discontinuity in delay anomaly is created by the binary classification of measurement types.

an appropriate fixed re-tracking point. If a discrete treatment is made to determine the appropriate tracking point, discontinuities in the final retrievals are introduced.

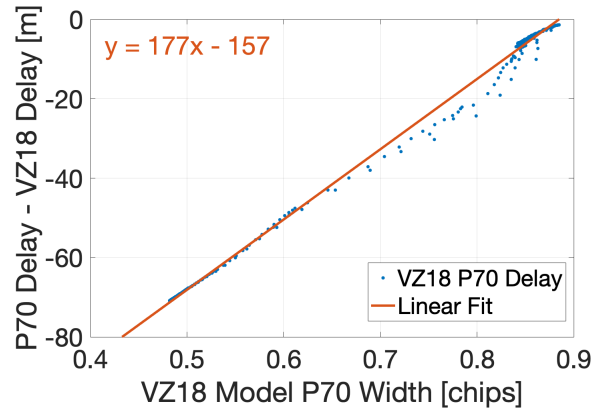


Figure 6.9: The predicted P70 delay re-tracking error on VZ18 modeled observations versus waveform width at 70% maximum power. This calibration can be used to correct tracking errors from strongly coherent observations.

A second approach using VZ18 modeled DDMs is taken to characterize the expected single-point re-tracking error for observations with width between 0.5 – 0.9 chips. Figure 6.9 shows the predicted P70 tracking error as a function of correlation waveform width, based on the VZ18 models. A linear calibration based on the predicted P70 tracking error is applied

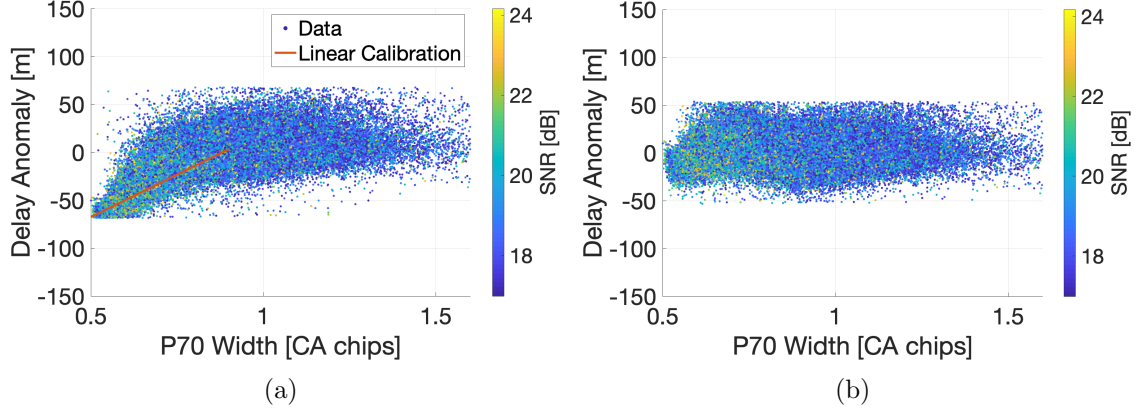


Figure 6.10: Calibrated P70 delay re-tracking results as a function of waveform width. (a) Uncalibrated P70 tracking results versus waveform width and the VZ18 linear tracking error calibration. (b) Calibrated P70 tracking results. Much of the systematic bias is corrected but higher order effects are observed.

to P70 delay anomaly results from CYGNSS in Figure 6.10. While most of the systematic bias is corrected in Figure 6.10(b), there are higher order effects that remain. The VZ18 calibration does not predict these residual higher-order effects.

An empirically derived track point that varies as a function of waveform width may correct for the systematic biases we observe. For example, a power function fit to delay anomaly versus waveform width. However, such an empirical solution should first be substantiated by improved modeling of the GNSS-R observations and understanding the true behavior. We have seen that the single-point tracker does not apply well to an important fraction of the data. Rather than search for an empirical correction, we turn to model based re-tracking. A VZ18 model fitting based approach could account for the smooth transition between coherent and incoherent reflections and re-track each measurement along that spectrum accordingly. In the next sections, the VZ18 GNSS-R scattering model is utilized for re-tracking delay waveforms and full DDMs, accounting for reflection coherence in a continuous way.

### 6.2.3 Model Re-trackers

To better capture the specular reflection delay, we now consider two re-tracking approaches based on the VZ18 model presented in the previous chapter. Two algorithms are presented that re-track 1-D delay waveforms, and full 2-D DDMs.

Delay re-tracking with the VZ18 model is first performed by fitting 1-D power-normalized, measured waveforms to power-normalized, model waveforms (VZ18WAVE). A database of model waveforms was compiled spanning the range of observation geometries seen by CYGNSS. This includes 45 – 85 deg incidence angles at increments of 1 deg, and 2 – 8 m/s wind speeds in increments of 0.05 m/s at a receiver altitude of 525 km. The resulting database contains 4,840 waveform models.

As shown in Figure 6.11, the shape of a power-normalized VZ18 delay waveform loses sensitivity to wind speeds above  $\sim 6$  m/s. Thus, the range of wind speed values evaluated only extends to 8 m/s.

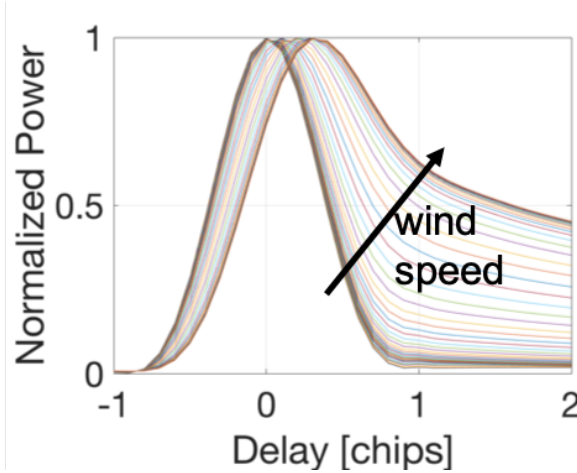


Figure 6.11: Sensitivity of power-normalized VZ18 waveforms to wind speed. Above wind speed  $\sim 6$  m/s, the VZ18 waveform shape converges. Wind speeds from 2 – 8 m/s are shown.

Modeled waveforms with matching incidence angle are fit to the observed data by minimizing the sum of the squared residuals over wind speed and delay. A model for each wind speed value is fit to a given observation. The specular delay from the lowest cost-to-fit

model becomes the re-tracking delay measurement. The cost-to-fit is calculated as

$$C_{\theta,w} = \sum_i (o_{\theta}^i - m_{\theta,w}^i)^2 \quad (6.6)$$

for each measurement-model pair. The VZ18WAVE models are found to fit many of the CYGNSS observations well up to delays  $\sim 1$  chip past the peak, as seen in Figure 6.12. In particular the strongly coherent observations are represented well with VZ18WAVE. However, we also found many of the diffuse CYGNSS observations are not well modeled at delays longer than 1 chip. Therefore, the cost-to-fit is computed over all delay samples within  $\pm 1$  chip of the waveform peak. This range provides a balance between fitting the waveform leading edge and peak without putting too much weight on the noisy and less well modeled long delays.

A further investigation determined a relationship between poor cost-to-fit and observation range rate. Figure 6.13 shows these results. Observations from fore or aft geometries with respect to the CYGNSS flight direction have large reflected-path range rates,  $\|\dot{R}\| > 2000$  m/s. A higher cost-to-fit is observed for these observations. This result indicates poor modeling of the observations with fore/aft reflection geometries.

The 1-D VZ18WAVE algorithm does not account for potential Doppler errors in the GNSS-R observation. In this implementation, the VZ18WAVE models are fit to observed waveforms at what the CYGNSS onboard, open-loop tracker has determined to be the “zero” Doppler bin. That prediction of the specular reflection Doppler is based on an approximate Earth model; and therefore, the systematic Doppler error is dependent on reflection azimuth, an effect that is seen by Figure 6.13.

#### 6.2.4 VZ18 DDM Re-tracking

The VZ18DDM algorithm fits power-normalized, 2-D modeled DDMs to power-normalized, observed DDMs. A approach similar to VZ18WAVE fitting is used here except the DDM

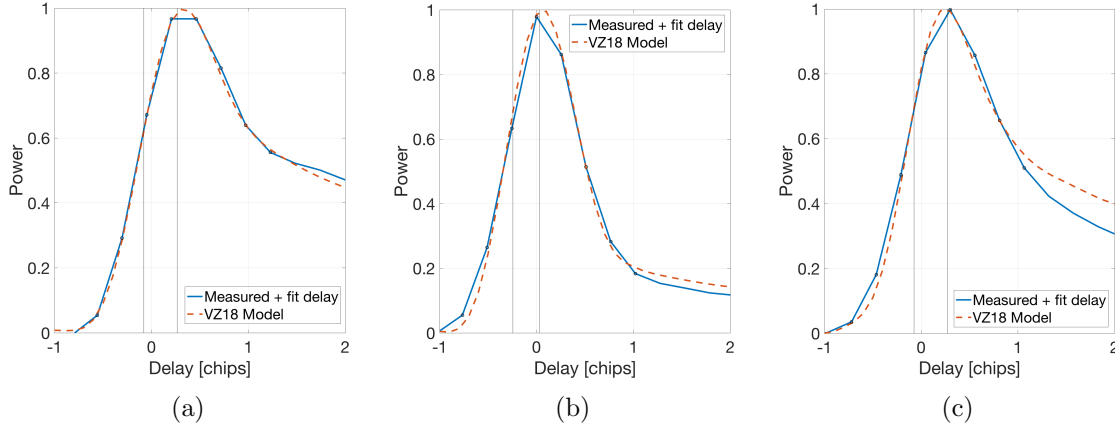


Figure 6.12: Examples of VZ18 Waveform model fitting to characteristic CYGNSS observations. (a) A typical observation-model matchup. (b) The VZ18 model is able to capture the coherent reflection characteristics. (c) Some observations have more power at longer delays than the models are able to account for.

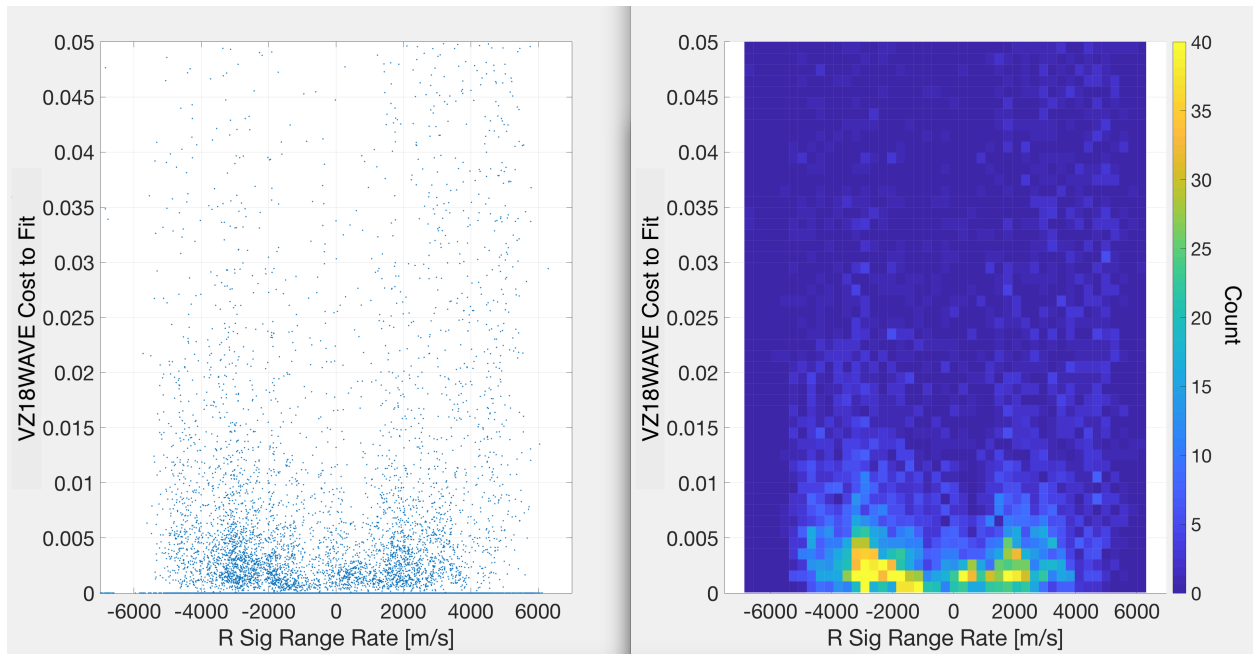


Figure 6.13: VZ18 waveform re-tracking cost versus reflected signal range rate. (left) Scatter plot of VZ18WAVE cost-to-fit versus reflected path range rate. (right) Binned histogram of cost-to-fit versus reflected path range rate. Higher cost is observed with measurements from fore or aft directions with large range rates. This result is indicative of mis-modeling of the reflected signal Doppler.

models are now Doppler shifted to account for the known CYGNSS onboard prediction error.



The known CYGNSS Doppler error results from the simplified Earth model used in prediction. The CYGNSS specular point prediction is presented in Section 6.3.2.1. This change to account for Doppler mis-modeling allows us to better track the dynamic delay-Doppler behavior of the DDM signal.

A model database of DDMs spanning  $45 - 85$  deg incidence angles at increments of 1 deg,  $2 - 8$  m/s wind speeds in increments of 0.05 m/s, and  $\pm 60 - 120$  deg azimuth angles in increments of 10 deg is created. This database contains 33,880 DDM model evaluations. Delay-Doppler samples within  $\pm 1$  chip and  $\pm 1000$  Hz from the peak of the observed DDM are used to compute a cost-to-fit for each model. The delay-Doppler offset of the lowest cost-to-fit model becomes the measured delay and Doppler.

The CYGNSS onboard delay-Doppler offset prediction algorithm for the specular reflection uses an ellipsoid reference that approximates the WGS84 ellipsoid. There is some error in the Doppler prediction with respect to the true specular reflection as illustrated in Figure 6.14. A bias of  $\sim 100$  Hz and linear trend from fore to aft geometries is observed in the open-loop tracker Doppler error. The VZ18DDM re-tracking method is constrained in Doppler to the predicted Doppler error computed with respect to the DTU mean sea surface model solution. That is, the VZ18DDM models are fit along the delay axis after being Doppler shifted to account for the known error from the MSS topography.

### 6.2.5 Re-tracking Error Statistics

The statistics of the VZ18WAVE and VZ18DDM signal tracking errors due to observation noise were investigated through synthetic noise analysis and with CYGNSS flight data. A Monte Carlo analysis by tracking VZ18 modeled observations with added Gaussian noise is used to simulate observations over a range of SNR. Real CYGNSS observations across a range of SNR are also re-tracked and the measurement precision is observed.

Analyzing the re-tracking performance with noisy VZ18 model observations is done to isolate the tracking precision from confounding errors in the flight observations from

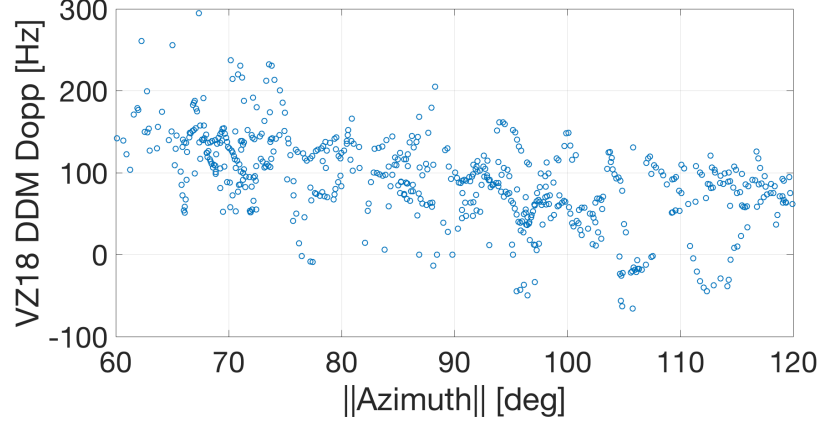


Figure 6.14: VZ18DDM retrieved Doppler versus reflection azimuth. The VZ18DDM re-tracking algorithm is able to retrieve the known Doppler error of the CYGNSS open-loop tracking prediction.

CYGNSS. Those VZ18 modeled observations are corrupted with synthetic Gaussian white noise  $w[n]$  with zero mean  $\bar{x}$  and constant variance  $\sigma_{noise}^2$  as

$$w[n] = rand(\sigma_{noise}^2, \bar{x} = 0). \quad (6.7)$$

The variance is chosen to vary the SNR parametrically. The calculation of SNR in (6.5) reduces to

$$SNR = 1/\sigma_{noise}, \quad (6.8)$$

for power-normalized modeled observations. SNR of the synthetic observations ranging from 8 dB to 20 dB were used to estimate the re-tracking performance. To create different realizations of the synthetic observation set, the Gaussian white noise is added to clean models,

$$x'[n] = x[n] + w[n]. \quad (6.9)$$

Each set of synthetic observations was then tracked by the VZ18WAVE and VZ18DDM methods. Table 6.1 lists the resulting tracking precision ( $\sigma_T$ ) for several SNR levels. The

Table 6.1: Re-tracking precision with the VZ18WAVE and VZ18DDM algorithms as a function of synthetic observation SNR.

| <i>Gaussian Noise Model, <math>w[n]</math></i> |          |                                      |                                     |
|--|----------|--------------------------------------|-------------------------------------|
|  | SNR [dB] | VZ18WAVE $\sigma_T$ [m]              | VZ18DDM $\sigma_T$ [m]              |
|  | 8        | 18.2                                 | 9.4                                 |
|  | 10       | 14.4                                 | 7.6                                 |
|  | 13       | 9.3                                  | 3.9                                 |
|  | 15       | 5.4                                  | 2.1                                 |
|  | 20       | 1.5                                  | 0.8                                 |
| <i>CYGNSS Observations</i>                     |          |                                      |                                     |
|  | SNR [dB] | VZ18WAVE $\sigma_{\Delta\delta}$ [m] | VZ18DDM $\sigma_{\Delta\delta}$ [m] |
|  | 13       | 12.3                                 | 12.3                                |
|  | 15       | 11.2                                 | 11.5                                |
|  | 20       | 10                                   | 9.8                                 |

VZ18DDM method outperforms VZ18WAVE in all cases. This is likely due to the additional information utilized in fitting more samples over a 2-D DDM than with a 1-D waveform. The DDM cost-to-fit is computed with 50 samples where as the waveform uses only 10 samples, a factor of 5 increase. It would be expected then, that the VZ18DDM method outperforms VZ18WAVE by a factor of  $\sqrt{5} \approx 2.2$  by Gaussian noise averaging. In fact, this is nearly the case as seen in Table 6.1. The simple noise model used here does not consider the correlation of noise between adjacent samples in the DDM, and is therefore optimistic. The change between VZ18WAVE and VZ18DDM will not, in practice, be a factor of  $\sim 2$  improvement in re-tracking. For comparison, Park [2017] predicts a 10% – 20% improvement for  $SNR = 20$  dB or 13 dB, respectively, when modeling speckle noise.

Flight data from CYGNSS were also analyzed to assess re-tracking precision, with care taken to isolate re-tracking precision from other confounding error sources in the delay anomaly. We selected a subset of 50,000 1-sec observations, spanning the range of observed SNR values. To eliminate mismodeling due to coherent signal components, the set only includes waveforms wider than 0.9 chips. To minimize ionospheric errors, the data were

selected from locations near the equator at local times between 22:00 and 05:00.

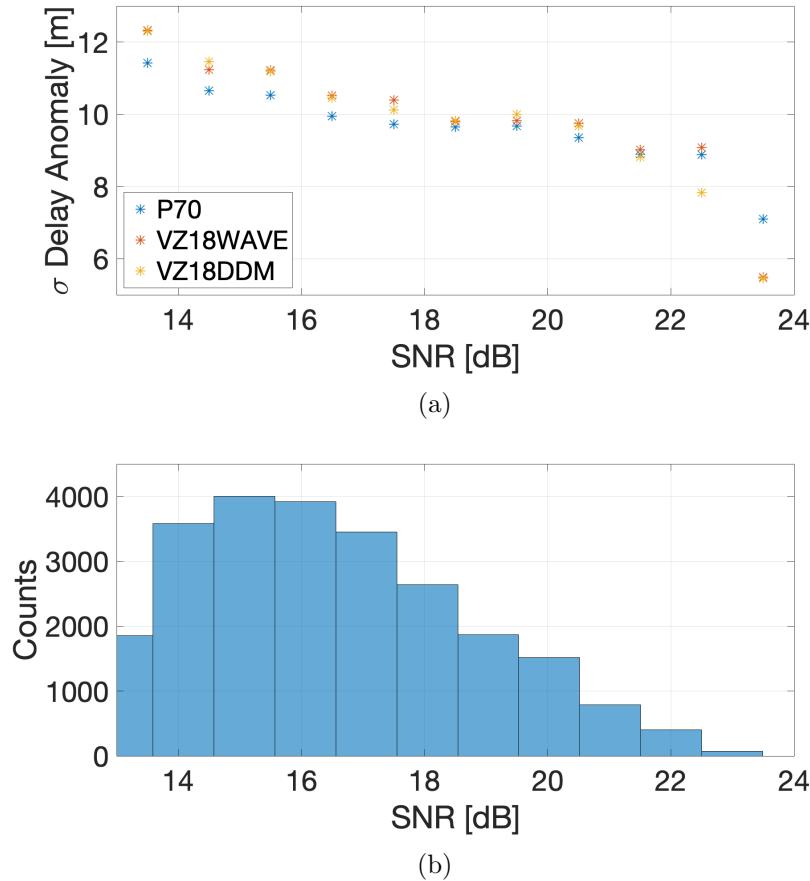


Figure 6.15: P70, VZ18WAVE, and VZ18DDM re-tracking precision versus SNR. (a) Re-tracking precision with P70, VZ18WAVE, VZ18DDM algorithms versus correlation SNR. (b) Histogram of delay anomaly samples versus SNR.

The P70, VZ18WAVE and VZ18DDM methods were each used to re-track these observations. The delay anomaly precision as a function of SNR is shown in Figure 6.15. All three methods are seen to produce similar results in delay anomaly precision. These errors are larger than predicted by the model-based analysis using simulated noise. The CYGNSS anomalies also show more modest reduction as a function of SNR and unexpectedly, no improvement with VZ18WAVE or VZ18DDM over the P70 tracker. We conclude that this is likely due to the dominance of atmospheric error or other effects not tied to signal tracking. However, an improvement in precision as SNR increases can still be observed. Note that for

$SNR > 19$  dB, the number of observations decreases significantly. The sudden improvement in delay anomaly precision observed for  $SNR > 22$  dB is suspect due to the limited number of available samples.

### 6.3 Reflection Modeling

A high-fidelity model has been assembled to simulate the GNSS-R reflection geometry and signal propagation errors as accurately as possible. Accurate modeling of the reflection path delay and propagation errors will account for geometric dependencies and remove systematic perturbations in the height retrieval caused by atmospheric interference. Each component of the model and the estimated uncorrected and residual errors of that component are described in Table 6.2.

#### 6.3.1 Receiver and Transmitter Orbits

Precise knowledge of the receiver and transmitter locations at the measurement time are vital for precise altimetry retrievals. The surface height measurement is made relative to the receiver location, and so any position errors map directly into the predictions. Errors in the vertical (or radial) coordinate have the largest effect on the height measurements. The precise delay model (6.1) predicts the geometric path delay of the reflected signal using the best possible estimates of the receiver, transmitter, and specular point coordinates. Receiver orbits are from post-processed orbit solutions. GPS transmitter coordinates are from the published International GNSS Service (IGS) final orbits [Dow et al., 2009]. Specular point coordinates are computed on the DTU mean sea surface model using the methods presented in Section 6.3.2 [Andersen, 2010].

The TDS-1 and CYGNSS onboard real-time processing algorithms use the GPS broadcast ephemerides. GPS broadcast orbits are estimated to be accurate to  $\sim 1$  m while the IGS final orbits are estimated to be accurate to  $\sim 3$  cm in position [IGS]. Thus, the use of IGS final orbits can improve altimetry. Accurate prediction of the excess path length of

Table 6.2: High-fidelity path delay model components with expected RMS error if left uncorrected and residual errors after correction.

| <b>Name</b>       | <b>Source</b>                | <b>Uncorrected<br/>Magnitude</b> | <b>Post-processing<br/>Residual Error</b> |
|-------------------|------------------------------|----------------------------------|---|
| RX orbit error    | L1 C/A Nav                   | 3 m position                     | 0.03 m ( $1\sigma$ GipsyX)                |
| TX orbit error    | [Dow et al., 2009; IGS]      | 1 m position                     | 0.03 m position ( $1\sigma$ )             |
| DTU10 MSS         | [Andersen, 2010]             | 100 m height                     | 0.1 m height ( $1\sigma$ )                |
| Ionosphere delay  | [Bilitza, 2015]              | < 15 m delay                     | < 3.5 m delay (day)                       |
|                   | [Komjathy, 1997]             | < 7 m delay                      | < 2 m delay (night)                       |
|                   | [Kumar, 2016]                |                                  |   |
|                   | [Montenbruck and Gill, 2002] |                                  |   |
|                   | [Roma et al., 2017]          |                                  |   |
| Troposphere delay | [Leandro et al., 2006]       | 6 m delay                        | 0.05 m delay ( $1\sigma$ )                |
| Antenna Baseline  | Metadata                     | 1 m delay                        | 0.001 m delay ( $1\sigma$ )               |

spaceborne GNSS-R also requires the consideration of satellite motion during the signal time of flight. Using the CYGNSS geometry as an example, a typical excess flight time of the reflected path is  $\sim 2$  msec. A GPS transmitter will move  $\sim 9$  m along its orbit during that time which produces a  $\sim 1$  m difference in the geometric path length. To account for this, separate transmitter coordinates are computed for the time of direct signal transmission and reflected signal transmission.

Current spaceborne GNSS-R missions, TDS-1 and CYGNSS, use GPS L1 C/A code pseudoranges for real-time positioning. Both missions compute navigation solutions at 1 Hz. These solutions are interpolated to the reflection observation time, and then downlinked to the ground and published. When using GPS L1 C/A for real-time navigation, there are well-known sources of error limiting the resulting accuracy. For example, the GPS transmitter broadcast ephemeris, clock errors, ranging noise, uncorrected ionospheric delays,

as well as interpolation artifacts in the published values. High-pass filtering the receiver orbit positions of both TDS-1 and CYGNSS to remove long period systematic behavior reveals that the onboard point solution variability of these spacecraft is comparable at  $\sim 3$  m in 3D position. More specific differences and limitations of the receiver positioning for TDS-1 and CYGNSS are discussed in Chapters 4 and 7 respectively. Typically though, the receiver L1 C/A navigation orbit solutions should be improved in post-processing to achieve the best altimetry measurement.

### 6.3.1.1 Precise Determination of the Receiving Platform Orbit

The third largest contribution to error in sea surface height retrievals for CYGNSS appears to be the spacecraft orbit knowledge, Table 6.2. Previous sections showed the TDS-1 or CYGNSS GPS L1 C/A position solution is  $\sim 3$  m RMS in 3D position. Two strategies were employed to assess the accuracy of the real-time CYGNSS orbits and to improve them by dynamical orbit constraints on the data. The first is to filter the original navigation solutions with an unscented Kalman filter (UKF). The second was to request for the CYGNSS team to downlink extra meta-data packets containing the raw pseudorange measurements made on-board. Those pseudorange values were then filtered with the GipsyX software by Bruce Haines (NASA JPL).

Filtering the original solutions with a UKF, and filtering the pseudorange observations with GipsyX, both yield similar orbit solutions. The residual error between the original solutions and the UKF solutions have  $RMS_{3D} = 2.7$  m. The residual error between the original solutions and the GipsyX pseudorange solutions have  $RMS_{3D} = 2.9$  m.

Figure 6.16 shows the residuals between the original CYGNSS orbits and the GipsyX pseudorange orbits over a long track through Indonesia (equatorial latitudes). The distribution of 3D position differences over the course of a day are shown as well. In the case shown here, most of the onboard orbit error is in the radial direction. Errors along the radial direction will have the largest, and most direct, impact on altimetry height retrievals.

For the CYGNSS analysis presented in Chapter 7, the UKF orbit solutions are used in place of the onboard computed solutions.

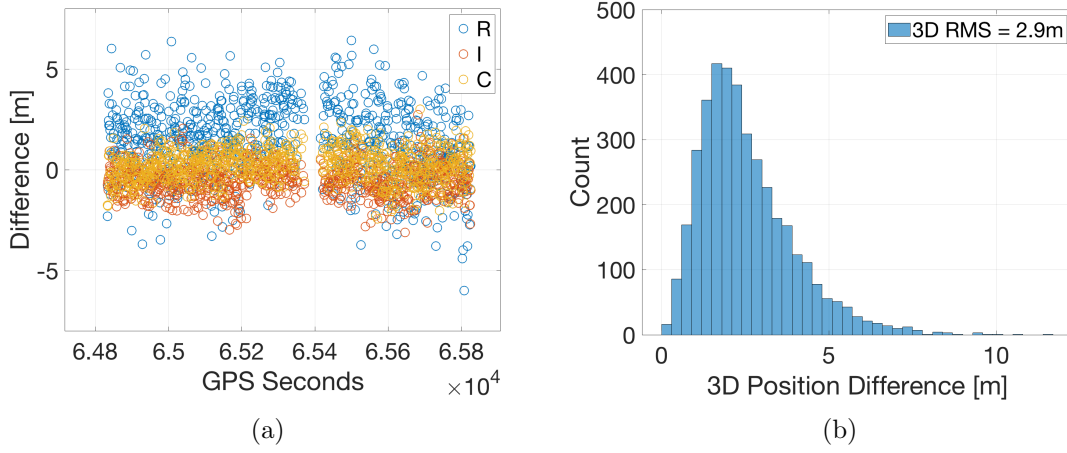


Figure 6.16: RIC orbit differences between CYGNSS point solutions and GipsyX filtered solution. (a) The CYGNSS meta-data orbits are compared to estimates from the GipsyX software in Radial (R), In-track (I), and Cross-track (C) components along two tracks over Indonesia. (b) Histogram of the 3D position RMS difference between the 1 Hz navigation solutions the GipsyX solutions.

### 6.3.2 Model Target Surface and Specular Point Prediction

A model surface is chosen to be the datum against which retrieved height anomalies will be referenced. The reference used when considering spaceborne reflections is the DTU10 mean sea surface (MSS). The airborne analysis in Chapter 3 uses the DTU13 MSS. Both DTU models are 2 arc-minute resolution gridded mean ocean topography maps from the Danish Technical University [Andersen et al., 2015; Andersen, 2010]. In future analysis the most up-to-date MSS models should be used. However, at this time the difference between DTU10 and DTU13 (or DTU15) is well below the level of error in the GNSS-R altimetry retrieval. Figure 6.17 shows that the DTU MSS models across Indonesia are less than  $\leq 10$  cm different.

The analysis with TDS-1 data in Chapter 4 adds ocean and solid body tides onto the DTU MSS. These tide model effects have not been included in the high-fidelity path-



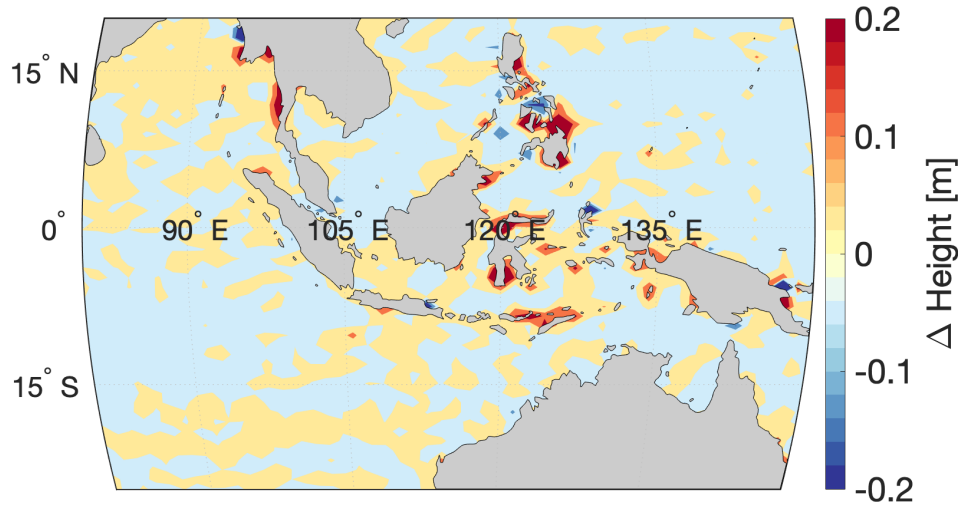


Figure 6.17: Difference between DTU15 and DTU10 MSS models. Most of this region is limited to  $\Delta h \leq 0.1$  m. Some coastal areas have a larger difference but those areas are too close to land to be considered in the GNSS-R altimetry analysis.

delay model for analysis of the CYGNSS datasets. Rather, the static MSS alone is used as the reference. Measured height anomalies with out tidal corrections conform to what the traditional radar altimetry community refers to as sea level anomaly.

#### 6.3.2.1 Prediction of Specular Point on the Model Surface

Given a reference surface and a time history of the GNSS-R receiver and GPS transmitters positions, the corresponding specular point locations can be predicted. An iterative approach developed by Wu et al. [1997] to compute the expected location of the specular reflection point is used in the high-fidelity model. The spherical Earth model solution can be solved analytically and is used as an initial guess for the solution on an ellipsoid or MSS

model. The spherical solution is described in Martin-Neira [1993]. Wu’s method constrains the spherical solution to the ellipsoid or MSS Earth model and computes the incident and reflecting angles. The specular point coordinate is adjusted until those angles match within a given tolerance.

In real-time, TDS-1 and CYGNSS predict the delay and Doppler offsets of the specular point with a computationally efficient quasi-spherical Earth model that approximates the WGS84 reference ellipsoid [Jales, 2016]. Beginning with the receiver ( $R$ ), and transmitter ( $T$ ) coordinates, they are transformed such that the earth ellipsoid is scaled down to a unit sphere. That is,

$$R' = FR, \quad T' = FT, \quad (6.10)$$

where the scaling matrix  $F$  uses the Earth semi-major ( $a$ ) and semi-minor ( $b$ ) axes,

$$F = \begin{bmatrix} \frac{1}{a} & 0 & 0 \\ 0 & \frac{1}{a} & 0 \\ 0 & 0 & \frac{1}{b} \end{bmatrix}. \quad (6.11)$$

The spherical solution is found with  $R'$  and  $T'$ , call the solution  $S'$ , and the coordinate transformation is reversed,

$$S = F^{-1}S'. \quad (6.12)$$

This onboard model yields a specular position that correctly predicts delay to within 15 m, and Doppler to within 250 Hz of the solution computed on the WGS84 ellipsoid by Wu’s method. The quasi-spherical Earth solution delay error, with respect to the WGS84 solution, varies as a function of incidence angle and latitude as seen in Figure 6.18. The prediction error associated with this model is known for TDS-1 and is removed in our high-fidelity model. The CYGNSS data includes the delay and Doppler offsets computed by the receiver in real-time and therefore avoids the need for recovering and removing this error.

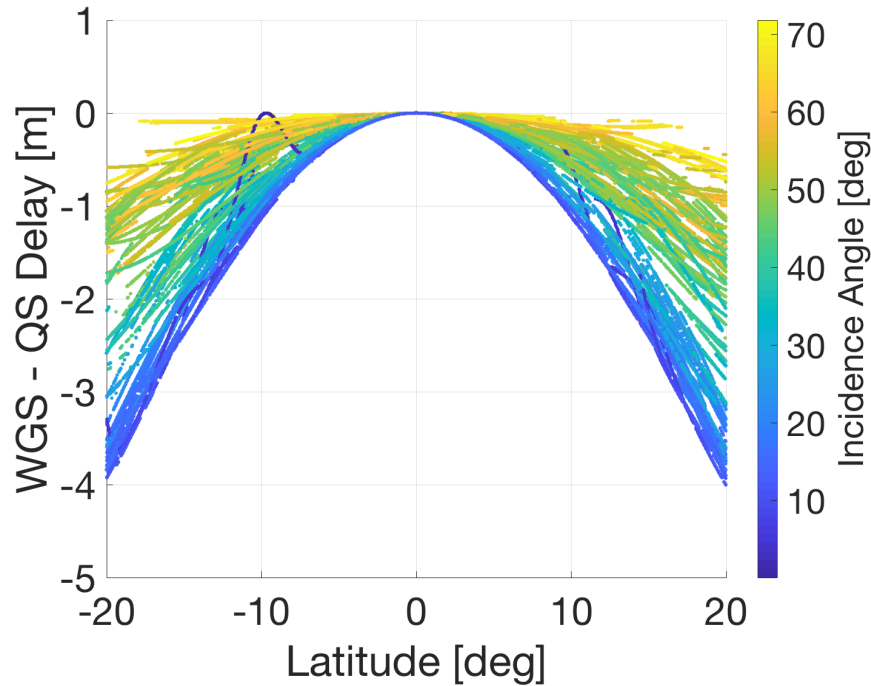


Figure 6.18: Delay prediction error with the quasi-spherical Earth model. The difference in geometric path delay between the full WGS84 and the quasi-spherical (QS) Earth solution is a function of latitude and incidence angle and reaches a maximum near  $\pm 40$  deg latitude. Only up to 20 deg latitude are shown for CYGNSS reflection geometries observed near Indonesia.

Accurately accounting for the receiver predicted delay and Doppler offsets in the open loop tracking is critical for precise altimetry. Errors here will map directly into the delay anomaly measurements. Figure 6.19 illustrates the change in the P70 re-tracking point as a function of Doppler error in the DDM as predicted by the Voronovich and Zavorotny 2018 model. Relatively small Doppler errors (much less than the bin size in TDS-1 or CYGNSS measured DDMs) can yield delay errors on the order of several meters. Recovery of the TDS-1 predicted delay/Doppler offsets is a topic of discussion in Chapter 4. CYGNSS, on the other hand, provides these values in the published meta-data. Other, unique challenges associated with these CYGNSS predicted values are covered in Chapter 7.

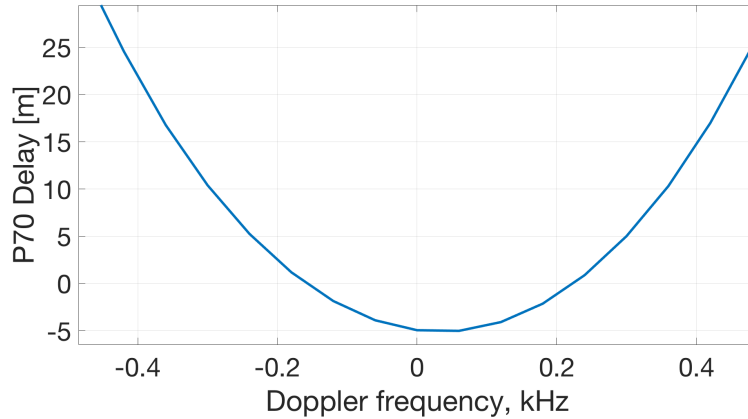


Figure 6.19: Predicted change in P70 re-track delay for Doppler shifted correlation waveforms. Small Doppler errors can produce relatively large delay errors. For example, a -100 Hz Doppler shift is already a change of 2.5 m in delay.

### 6.3.3 Ionospheric Delay

Ionospheric delay along the direct and reflected signal paths cause ranging errors of several meters. High-precision orbit determination and scientific observations with GNSS rely on dual-frequency (L1 and L2) measurements to directly measure and remove ionospheric effects [Brunner, 1991]. Unfortunately, TDS-1 and CYGNSS rely solely on single-frequency L1 measurements. Two models for vertical TEC ( $vTEC$ ) have been implemented for analysis of TDS-1 and CYGNSS data. The International Reference Ionosphere 2012 (IRI2012) [Bilitza, 2015] is used to model the vertical total electron content ( $vTEC$ ) values for the TDS-1 analysis. IGS Global Ionospheric Maps (GIMs) [Hernández-Pajares et al., 2009] are expected to be more accurate and are used to estimate  $vTEC$  for the CYGNSS observations. The IGS GIMs are models informed by GNSS ionosphere observations from a global network of ground stations [Roma et al., 2017]. In both cases (IRI model or IGS GIM) the same procedure is used to correct for the excess ionospheric delay along the reflected signal path.

To estimate the excess ionospheric delay a  $vTEC$  value is estimated at ionospheric pierce points associated with each of the three ray paths illustrated in Fig. 6.20, namely, the rays from the GPS transmitter to receiver ( $vTEC_3$ ), the GPS transmitter to the surface

reflection point ( $vTEC_1$ ), and the reflection point to the receiver ( $vTEC_2$ ).

The vTEC values estimated for the two pierce points on the reflected path (rays 1 and 2 in Figure 6.20) are mapped to slant path delays with the mapping function

$$M_{1,2}(E) = \frac{1}{\sqrt{1 - \left( \cos(E) \cdot \frac{R_E}{R_E + h} \right)^2}} \quad (6.13)$$

given by Equation 4.20 in Komjathy [1997], where  $E$  is the elevation angle at the reflection point,  $R_E$  is the Earth's radius, and  $h$  is the ionospheric shell height, set to be 450 km in this work.

Correction of ionospheric delay on the direct signal from the GPS to the spaceborne receiver (ray 3 in Figure 6.20) is performed using a method developed by Montenbruck and Gill [2002]. The mapping function given by Montenbruck and Gill [2002], specifically formulated to compute slant path delays for low Earth orbiting spacecraft, is given by,

$$M_3(E_{IP}) = \frac{\alpha}{\sin(E_{IP})} \quad (6.14)$$

where  $E_{IP}$  is the elevation angle of the line of sight path through the ionospheric pierce point, and  $\alpha$ ,

$$\alpha = \frac{e - \exp(1 - \exp(-z_{IP}))}{e - \exp(1 - \exp(h_0/H))}, \quad (6.15)$$

is a scaling factor for the ionospheric density above the receiver altitude, which depends on the receiver altitude,  $h_s$ , the shell height,  $h_0$ , and a scale height,  $H$ . The scaled height of the ionospheric pierce point,  $z_{IP}$ , is solved for from

$$\begin{aligned} \exp(1 - \exp(-z_{IP})) &= \frac{1}{2}(e + \exp(1 - \exp(-z_s))); \\ z_s &= (h_s - h_0)/H. \end{aligned} \quad (6.16)$$

The total group delay along the reflected and direct ray paths is then estimated from those slant TEC values by

$$\delta_{1,2,3} = M_{1,2,3} \cdot \frac{40.3 \times 10^{16} \cdot vTEC}{f_{L1}^2} \quad (6.17)$$

and the excess delay on the reflected signal due to the ionosphere is modeled by

$$\delta_{iono} = (\delta_1 + \delta_2) - \delta_3. \quad (6.18)$$

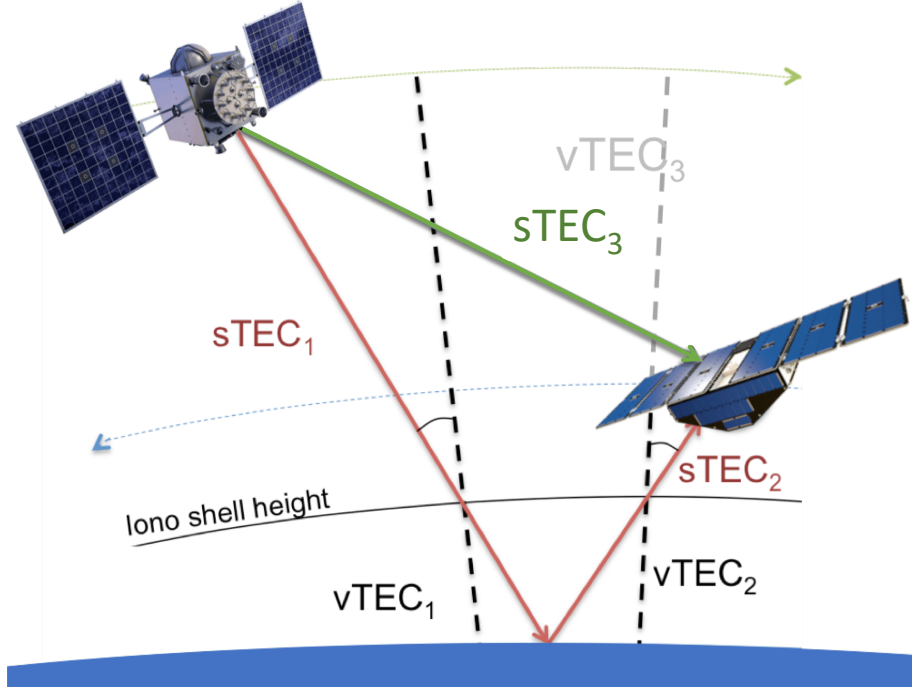


Figure 6.20: Ionospheric delay model. The ionospheric delay effect is estimated on the reflected signal ray path. Vertical TEC ( $vTEC$ ) columns at the up and down-traveling pierce points are evaluated from the IRI2012 model and mapped to slant angles. The summed slant TEC is used to estimate the excess delay effect.

### 6.3.3.1 Accuracy of the Ionospheric Delay

CYGNSS, like TDS-1, can only measure single frequency GPS L1 signals and therefore requires an estimated ionospheric delay to remove the effects of the charged atmosphere from the altimetry retrievals. The residual error associated with modeling the ionospheric delay

along the GNSS-R signal path is identified as the second largest error source in the error budget presented in Table 6.2.

The literature on ionospheric delay modeling suggests that the International Reference Ionosphere 2012 (IRI-2012) model may have an error up to about 35% in estimation of TEC [Kumar, 2016]. The IGS GIMs on the other hand are estimated to have a 20% relative error and bias up to 4 TECU [Roma et al., 2017]. A 25 – 35% error with either model would leave a residual error of  $\sim 2 - 7$  m delay RMS depending on the measurement time of day. It is difficult to isolate how such residual errors might be structured along a measurement track or across geography without collocated and contemporaneous measurements of the ionosphere. We can look at the delay anomaly versus estimated ionospheric delay, and any delay anomaly differences between day-time and night-time measurements to better understand how well the modeled ionospheric corrections generally perform.

The night-time observations are predicted to be relatively free of ionospheric influence. The mean predicted night-time ionospheric delay contribution along the direct path is  $< 1$  m, and along the reflection path is  $\sim 2.5$  m. Comparing night-time observations to ionosphere-corrected day-time observations may reveal the magnitude of any remaining error. Figure 6.21 shows the measured - modeled delay anomaly versus GIM excess ionosphere delay estimate. Using the GIM to correct for the ionosphere delay significantly reduces the correlation between delay anomaly and estimated ionosphere delay. Linear regression of the delay anomaly versus GIM ionosphere delay in Figure 6.21(a) and (b) shows that using the GIM based correction helps to remove much the ionospheric error in the measurement.

Figure 6.22 shows that the IRI-2012 based corrections also significantly reduce the bias between day and night time delay anomalies. Before applying the IRI-2012 corrections, a 6.6 m delay bias is observed between day and night observations. After applying the IRI-2012 corrections, the bias is reduced to 1.6 m delay. If the GIM based correction is used with the same CYGNSS data, the day-night bias is reduced to 0.4 m.

Both models correct for the majority of the ionospheric influence on the measured path

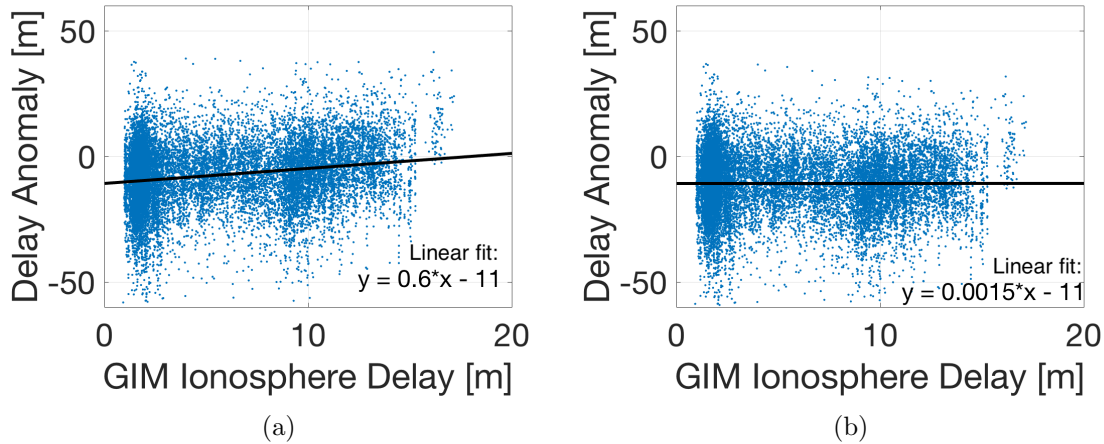


Figure 6.21: CYGNSS Delay anomaly before and after considering the GIM ionosphere corrections. (a) Delay anomaly before correcting for ionosphere has a clear correlation with the ionosphere delay estimate. (b) Delay anomaly after correcting for ionosphere has significantly reduced correlation.

delay. However, there is room for improvement in the implementation of both methods. The exact ionospheric density profile is not known for either case and can play an important part in accurately mapping vertical TEC columns to slant angles and estimating top-side contributions. For my analysis, a Chapman type profile model is assumed in all cases [Montenbruck and Gill, 2002]. The inflection point (or peak density) of the Chapman profile is assumed to be 450 km, matching the GIM shell heights. More accurate modeling of the ionospheric density profile could improve the delay estimates and further reduce ionospheric errors.

Martin-Neira et al. [2011] investigates using GPS L1 and L5 dual-frequency observations to reduce the ionospheric error for GNSS-R altimetry. It is predicted that the residual ionospheric error could be reduced to  $\sim 5$  cm. This result stresses the importance for dual-frequency observations in future GNSS-R altimetry experiments.



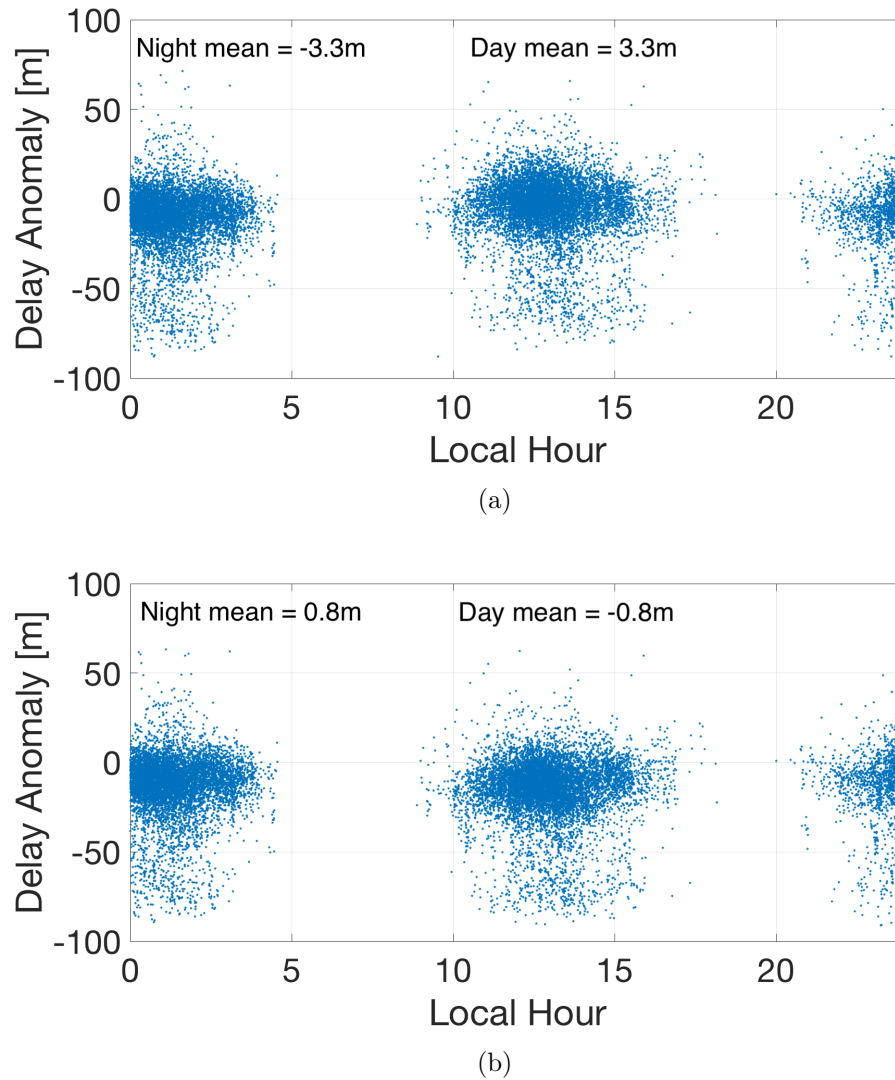


Figure 6.22: Delay anomaly before and after considering IRI-2012 ionosphere corrections. (a) Delay anomaly from CYGNSS data in Indonesia before being corrected for ionospheric delay effects with IRI-2012 TEC estimates. (b) Delay anomaly after being corrected for ionospheric delay effects. The bias between local day and night measurements is significantly reduced.

### 6.3.4 Tropospheric Delay

Tropospheric delays on the reflected signal path are accounted for using the UNB3m model [Leandro et al., 2006]. UNB3m uses empirically derived average atmospheric parameters computed for a grid of latitudes and seasons, Saastamoinen zenith delays [Davis et al., 1985], and Niell mapping functions [Niell, 1996] to estimate the delay. This type of model

is convenient to use for large scale analysis with global, spaceborne, observations. Leandro et al. [2006] estimate a worst-case residual delay error of  $\sim 5$  cm for the UNB3m model as compared to radiosonde measurements.

The tropospheric delay effects are highly concentrated below an altitude of 10 km, and we are only considering GNSS satellites at elevation angles above  $\sim 40$  deg. Therefore, tropospheric corrections are only applied to the downward and upward reflected signal paths below the receiver altitude. No tropospheric correction is required for the direct signal path to the spaceborne receiver. The UNB3m model is evaluated at the specular point latitude and doubled to account for the downward and upward paths. As modeled by UNB3m, the latitudinal sensitivity in the tropospheric propagation delay is less than 0.5 cm/100 km ( $\sim 1$  deg latitude). The pierce points of each reflection path through the troposphere at 10 km altitude are at most 10 km apart resulting in a negligible error,  $< 0.05$  cm, due to the single evaluation. Therefore, evaluating the model at two separate pierce points appears to be unnecessary.

### 6.3.5 Bistatic Antenna Baseline Effect

Accurate prediction of the reflected signal path delay must also account for the physical offset between zenith and nadir-looking antennas on the receiving spacecraft. To make this correction precisely, one would need information on the antenna installations, the effective phase centers of the two antennas, and the attitude of the satellite in orbit. For TDS-1, the coordinates of the antenna internal centers, on the faces where they are mounted, are provided by SSTL. The spacecraft attitude is controlled such that the body frame is aligned with the orbit local-vertical, local-horizontal (LVLH) frame [Jales, 2016; Jales and Unwin, 2015]. The body frame x-axis is aligned in the velocity direction, the body frame z-axis is aligned in the orbit radial (local vertical) direction, and the body y-axis completes the right handed coordinate system. The TDS-1 antenna baseline vector,  $\vec{b} = [-264.1, 399.1, -910.8]^T$  mm, given in the body frame is used to model the delay effect  $\delta_{baseline}$  for a given

incident signal by

$$\delta_{baseline} = (\mathbf{R} \vec{b}) \cdot \hat{e} \quad (6.19)$$

where  $\mathbf{R}$  is the rotation matrix from the LVLH frame to the earth-centered, earth-fixed (ECEF) frame,  $\vec{b}$  is the antenna baseline vector expressed in the body frame, and  $\hat{e}$  is the line of sight direction to the GPS transmitter expressed in the ECEF frame. The rotation matrix  $\mathbf{R}$  is computed from the basis vectors of the LVLH frame by

$$\mathbf{R} = \begin{bmatrix} \hat{i}_1 & \hat{c}_1 & \hat{r}_1 \\ \hat{i}_2 & \hat{c}_2 & \hat{r}_2 \\ \hat{i}_3 & \hat{c}_3 & \hat{r}_3 \end{bmatrix} \quad (6.20)$$

where  $\hat{r}$  is the orbit radial (local vertical) direction,  $\hat{c} = \hat{r} \times \hat{v}$ , and  $\hat{i}$  completes the set in the in-track direction, each written in the ECEF frame.

The CYGNSS spacecraft body frame is illustrated in Figure 6.23. The same information regarding antenna mounting and nominal spacecraft attitude is known for CYGNSS. Thus, a similar approach is used. Errors in the spacecraft pointing for TDS-1 or CYGNSS are typically limited to  $\pm 1$  deg. Pointing errors at this level produce effects in the delay anomaly due to the antenna baseline that are  $\leq 1$  mm. So, the nominal spacecraft attitude may be assumed when applying the antenna baseline correction with either spacecraft.

### 6.3.6 Future Components of the High-fidelity Model

There are three other small effects that are not accounted for in the high-fidelity model presented above. These effects are nonetheless important for completeness and should be considered in future work. Electromagnetic sea state bias is an important effect in traditional radar altimetry, but is not included in the model at this point because the magnitude, estimated to be 10 – 20 cm [Camps et al., 2017; Ghavidel et al., 2016; Park et al., 2016], is well below other current limitations of the observations and models. Other considerations

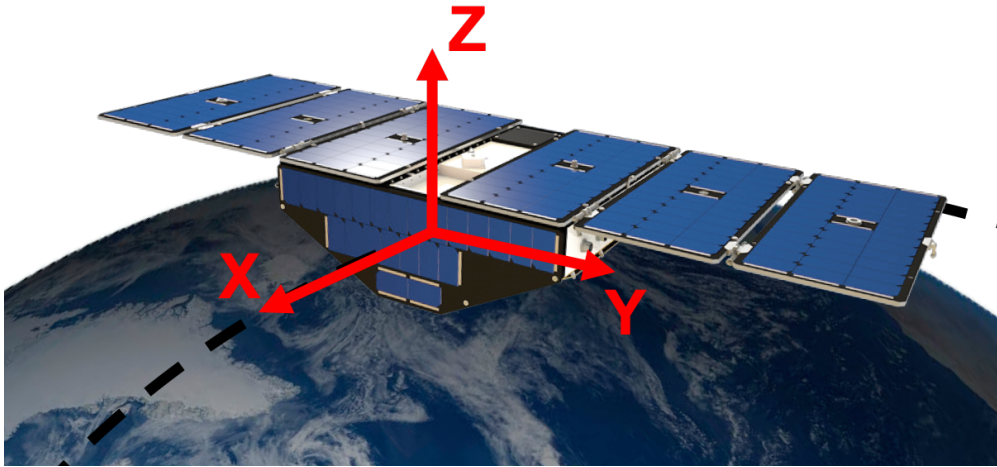


Figure 6.23: CYGNSS body frame illustration. The CYGNSS body frame is nominally aligned such that the  $+x$ -axis is in the velocity direction, the  $+z$ -axis is in the radial direction, and the  $+y$ -axis completes the set.

include improved ionosphere profile modeling as proposed by Martin-Neira et al. [2011], and tropospheric corrections based on localized observations.

## Chapter 7

### Analysis of CYGNSS GNSS-R Observations for Ocean Surface Altimetry

#### 7.1 Introduction

The CYGNSS mission dataset is the largest set of spaceborne GNSS-R data available today. Such a large set of spaceborne observations is an excellent resource for continuing to develop methods for ocean altimetry. The analysis with TDS-1 data in Chapter 4 presented an initial error budget for space-based conventional GNSS-R ocean surface altimetry, and now, the CYGNSS data allow us to revise that. The error budget gives a breakdown of the distribution of error in the ocean height retrieval, specifying the error magnitude of each source of mis-modeling, or natural interference that has been identified. The breakdown in Table 4.1 showed that the three leading error sources were delay re-tracking ( $\sim 10$  m delay from 1 sec integrations), residual error in the ionospheric delay correction ( $\sim 2 - 5$  m delay), and error in the receiver positioning ( $\sim 3$  m position) [Mashburn et al., 2018]. Applying the improvements and new retrieval methods presented in Chapter 6 allows us to analyze the altimetry performance in the presence of coherent observations by way of Indonesian ocean altimetry with CYGNSS.

This chapter provides an overview of the CYGNSS mission and the GNSS-R altimetry results we have achieved. Relevant details of the CYGNSS data and receiver operation are presented first. Subsequently, a case study for GNSS-R altimetry in Indonesia is motivated and an analysis of the most significant errors is presented. Finally, the CYGNSS GNSS-R altimetry sea surface height retrievals are shown.

## 7.2 CYGNSS Mission Description

The CYGNSS mission is a University of Michigan led, NASA Earth Ventures project [Ruf et al., 2016]. CYGNSS was designed to utilize GNSS-R observations from its constellation of 8 spacecraft in low Earth orbit for remote sensing of ocean surface level winds inside tropical cyclones. As the first GNSS-R science mission in space, CYGNSS represents a major step forward in the development of GNSS bistatic radar remote sensing as a viable technique for Earth science.

The CYGNSS constellation is configured such that the spacecraft will overfly similar regions at 12 minute intervals, providing many closely-spaced samples of the surface [Ruf et al., 2016]. Complete coverage and re-sampling of the tropical latitudes, between  $\pm 38$  deg latitude, occurs in less than 24 hours.

For ocean altimetry, the CYGNSS measurement density, coverage, and frequency are favorable to fill in gaps between traditional altimetry observations. CYGNSS covers the tropical latitudes with a wide effective swath. Dense and frequent coverage should allow observation of mesoscale features that can slip past geodetic track altimeters. For example, the CYGNSS median and mean revisit times are 2.8 hours and 7.2 hours, respectively [Ruf et al., 2016], as compared to the 10 day repeat tracks of JASON [Lambin et al., 2010].

## 7.3 The CYGNSS GNSS-R Receiver and Observations

Each of the eight CYGNSS spacecraft is equipped with an SGR-ReSI GNSS-R receiver, the same instrument flown onboard TDS-1 [Jales and Unwin, 2015; Ruf et al., 2016; Unwin et al., 2010]. The SGR-ReSI system has been designed for ocean surface wind speed retrievals rather than altimetry. The resulting limitations and issues for altimetry include imprecise pseudorange positioning and timing with no recorded carrier phase data, tracking of only single-frequency, low-bandwidth signals, and relatively low LHCP antenna gains. More detailed descriptions of the SGR-ReSI operations for positioning, timing, and reflection tracking

Table 7.1: CYGNSS data level definitions.

|              |  |
|--------------|--|
| Level 1      | Raw counts and power calibrated DDMs of the observed bistatic radar cross-section.                                     |
| Level 2 MSS  | Spatially averaged mean square slope (MSS) product over a $25 \times 25$ km <sup>2</sup> region.                       |
| Level 2 Wind | Wind speed retrieval product with 25 km resolution.  |
| Level 3      | Gridded wind speed product at 0.2 deg resolution.  |
| Level 4      | Assimilated wind speed product at 9 km resolution. Combines conventional data and CYGNSS winds with NOAA's HWRF model. |

were presented in Chapters 4 and 6, and in Unwin et al. [2010]. Realistically, CYGNSS cannot be expected to produce science quality ocean surface altimetry data. Rather, analysis of these data from CYGNSS, as with TDS-1, help us to understand the challenges encountered with GNSS-R, and to establish requirements for future GNSS-R altimetry missions.

Since the launch of CYGNSS in December 2016, the GNSS-R observations have been published to the NASA Physical Oceanography Distributed Active Archive Center (PO.DAAC) where they are freely available [CYGNSS, 2017]. As of October 2018, there are 550 days of CYGNSS data published on the PO.DAAC. The daily data sets include observations from several, though not always all, of the CYGNSS spacecraft; with each receiver nominally recording 4 simultaneous reflections at 1 Hz. There are an estimated 750 million to 1.5 trillion GNSS-R observations now available online from CYGNSS; this assumes between 50% - 100% duty cycle for the 8 spacecraft.

Table 7.3 lists and defines the CYGNSS data levels. The following analysis is based on the Version 2.1 Level 1 data products [CYGNSS, 2017]. CYGNSS Level 1 data are the raw counts and power-calibrated 1-sec incoherently averaged delay-Doppler map observations. Only the raw count DDMs are used here. This choice allows antenna pattern effect to be explicitly accounted for in our analysis.

## 7.4 CYGNSS Onboard Processing and Issues for Altimetry

Primarily due to the limited capacity of the spacecraft-to-ground telemetry budget, use of the CYGNSS data set poses some unique challenges and limitations for altimetry. Fortunately, the timing issues seen with TDS-1 are not present here. Most of the data sent from CYGNSS to the ground is optimized for scatterometry applications. Variables that are secondary to that application tend to be truncated to minimize packet size. Truncation adversely affects both the predicted excess path delay computed by the onboard open-loop tracker, and the onboard position solutions. The following discussion describes how the predicted path delays and the position solutions are affected by truncation.

At each millisecond, the CYGNSS flight computer sets up a nominal GPS signal model at the predicted reflection delay and Doppler offsets to be cross-correlated with the incident signal. The predicted delay and Doppler offsets are computed using the quasi-spherical Earth algorithm described in Chapter 6 Section 6.3.2.1 [Jales, 2016]. Each 1-msec integration is aligned in delay and Doppler by the predicted values, and one-thousand 1-ms coherent integrations are summed to form a 1-sec DDM. To conserve downlink data, the DDMs are cropped tightly in delay and Doppler, around the peak observed sample, to produce an  $11 \times 17$  array of correlation power values. CYGNSS tags each 1-sec DDM with the time and the predicted excess delay and Doppler values corresponding to the mid-point of the incoherent integration. The open-loop predicted excess delay and Doppler values are necessary to compute the correct offset of each DDM sample from the closed-loop direct signal tracking. Therefore, knowing the predicted excess path delay of each reflection with high precision is necessary for accurate ocean altimetry with the CYGNSS observations.

The predicted excess path delay is, unfortunately, secondary to the scatterometry mission and therefore has been truncated to discrete 0.1 C/A chip intervals ( $\sim 30$  m resolution). Figure 7.1 shows the truncated predicted excess delay (a variable called *add\_range\_to\_sp*) compared to the full precision values. The full resolution example is part of a small se-



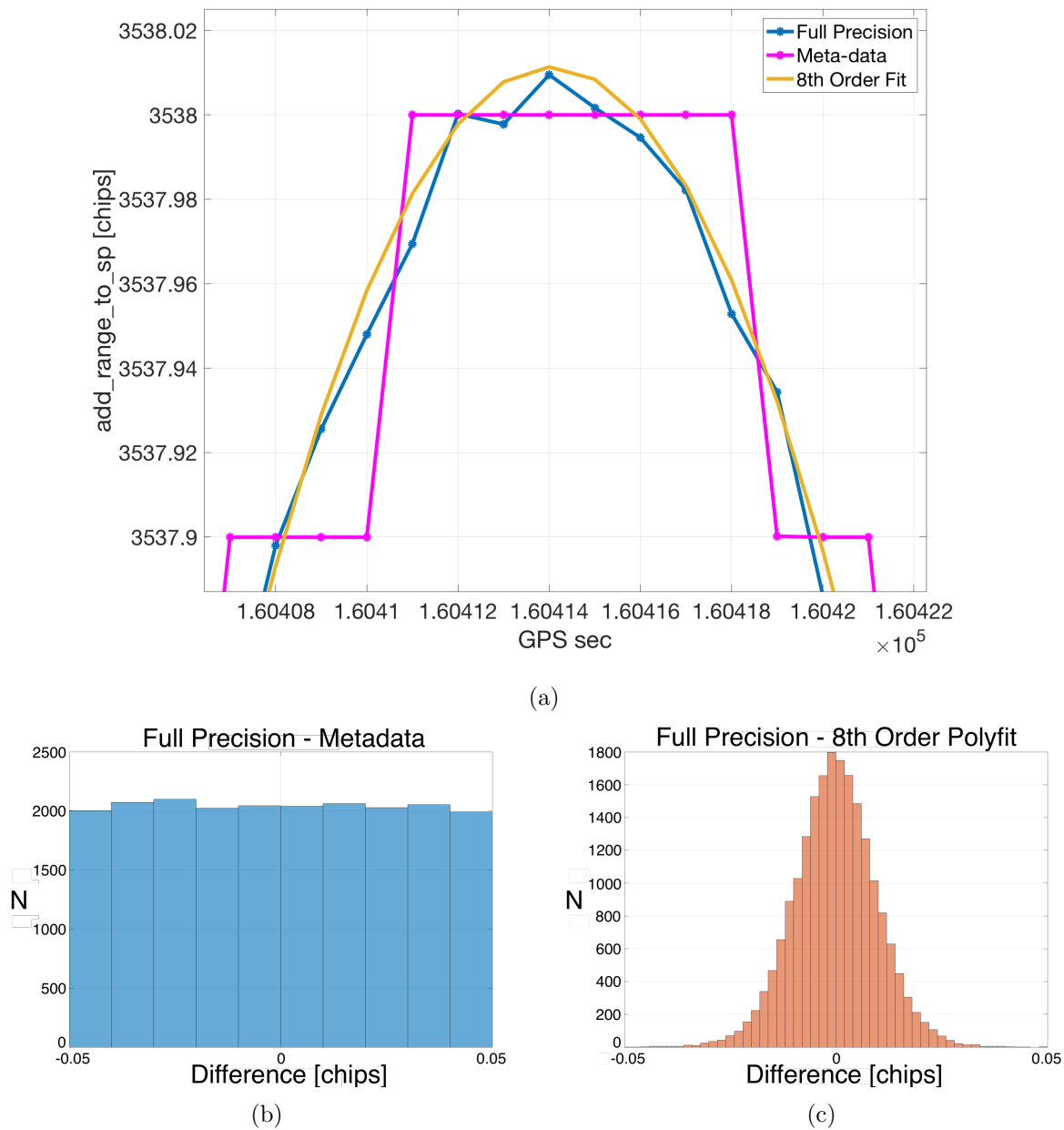


Figure 7.1: The CYGNSS onboard path delay prediction and a method of compensation for quantized values. (a) The predicted delay of each 1 second integration period is reported with 0.1 chips ( $\sim 30$  m) numeric precision. (b) The truncated values have uniformly distributed residuals from the full precision values. (c) An 8th order polynomial fit to the truncated delays. The full precision - polyfit residuals have standard deviation  $\sigma = 0.016$  chips  $= 4.6$  m.

lection of extra debugging data packets we received from a “flat-sat” engineering model at

the Ohio State University [personal communication from Andrew O’Brien and Eric Loria, 03/21/2018].

To compensate for the truncation, a method to best approximate the full precision *add\_range\_to\_sp* values is needed. Andrew O’Brien and Eric Loria suggest a polynomial curve fit to the truncated delay values to produce a good approximation with no bias and Gaussian residuals from the full precision values. A polynomial of order  $n = 8$  gives the best results as illustrated in Figure 7.1(c). The residual error of the polynomial fit has a standard deviation of  $\sigma = 0.016$  chips = 4.6 m with respect to the full precision values.

A second, smaller effect also impacts the predicted delay and Doppler values used by CYGNSS during the open-loop tracking process. The CYGNSS receiver attempts to minimize the computational load required to predict the delay and Doppler offsets of each reflection. The open-loop tracker updates the prediction at 10 Hz (100 ms intervals) and propagates that prediction forward in time linearly. The true specular delay varies non-linearly. Thus, the measured DDM is then smeared in delay/Doppler according to the error in the linear propagation. The observed reflected-path range accelerations are limited to  $\pm 20$  m/s<sup>2</sup>. Therefore, the delay smearing is expected to be  $< 0.1$  m per update interval.

The position solution coordinates are also truncated in downlink. Each 1 Hz position solution is reported with 1 m numerical precision. Two methods for orbit determination improvements were presented in Chapter 6. How those strategies affect the altimetry results is discussed later in Section 7.6.1.

## 7.5 A Case Study in Indonesia

To explore the potential utility of the CYGNSS data for ocean altimetry the region surrounding Indonesia, bounded by latitudes S25 deg and N20 deg and longitudes W80 deg and W150 deg, was chosen. This region is of high oceanographic interest because of the large scale, seasonal ocean height signals associated with the Indonesian throughflow currents ( $\pm 1$  m height across several hundred km). Large algal blooms are also known to take place

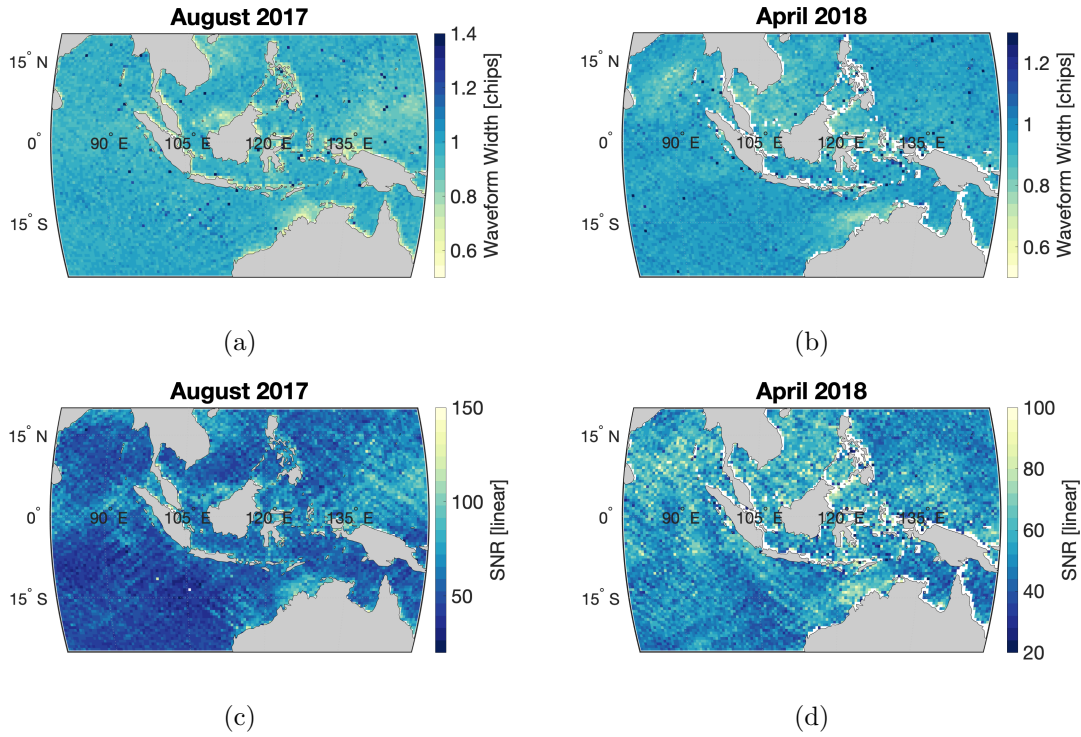


Figure 7.2: Observed coherence patterns with correlation waveform width and SNR across Indonesia. (a,b) CYGNSS delay waveform width at 70% power measured in C/A chips in August 2017 and April 2018. Narrow waveforms indicate more coherent-like reflections while wide waveforms indicate diffuse reflections. (c,d) CYGNSS reflected signal correlation SNR in linear units. Higher SNR is correlated with narrow waveform width and therefore coherent-like reflections.

around Indonesia. These blooms have the effect of calming the surface of the sea, providing a region where in one can expect to see coherent reflecting characteristics. Such sea state conditions tend to produce relatively high SNR observations, further aiding the altimetry retrieval as seen in Figure 7.2(c) and (d).

The CYGNSS data set contains  $\sim 4000$  1-sec ocean observations, per spacecraft, per day within our geographic constraint. Of those,  $\sim 35\%$  typically have SNR above 10 dB and  $2-3\%$  have the narrow delay waveform characteristic of a coherent reflection. The CYGNSS observations from around Indonesia not only include a large number of potentially coherent reflections, but certain regions persistently produce reflections with coherent characteristics. Figure 7.2 shows delay waveform width and correlation SNR around Indonesia for 5 days in

August 2017 and 5 days in April 2018. From these maps, the correlation between waveform width and SNR is clear. It can also be seen that there are regions with persistently narrow and high SNR observations over these 5 day periods. Those patterns appear to change between months as well as seen by comparing results from August and April. Indonesia as a test bed provides a sufficiently large and varied data set with which to develop correction terms and evaluate the performance of new delay re-tracking algorithms.

## 7.6 Analyzing CYGNSS Data

The CYGNSS observations are processed according to the procedures outlined in Chapter 6. As defined there, ‘delay anomaly’ and ‘height anomaly’ results refer to fully corrected values with all components of the path delay model included.

CYGNSS data from April 20 - 28, 2018 and from the area of Indonesia have been analyzed here. The full high-fidelity delay model was used along with P70, VZ18WAVE, and VZ18DDM re-tracking, and the CYGNSS specific considerations described above. Only data from open waters (specular point  $\geq 25$  km from land) with a correlation SNR  $\geq 10$  dB are considered. Table 7.2 lists each of the error sources expected to affect the CYGNSS altimetry returns. The following sections discuss the error contributions to CYGNSS altimetry. Specifically, the effects of precise orbit determination, and model-based re-tracking are discussed in Sections 7.6.1 and 7.6.2. Figure 7.3 shows the measured surface height with respect to the WGS84 reference ellipsoid using the April 20 - 28, 2018 data with 1 second incoherent averaging around Indonesia. A 0.8 deg Gaussian kernel filter is applied to the measured surface heights in Figure 7.3(a). The VZ18DDM re-tracking method is used, along with UKF filtered CYGNSS position solutions and IGS GIM ionospheric delay corrections.

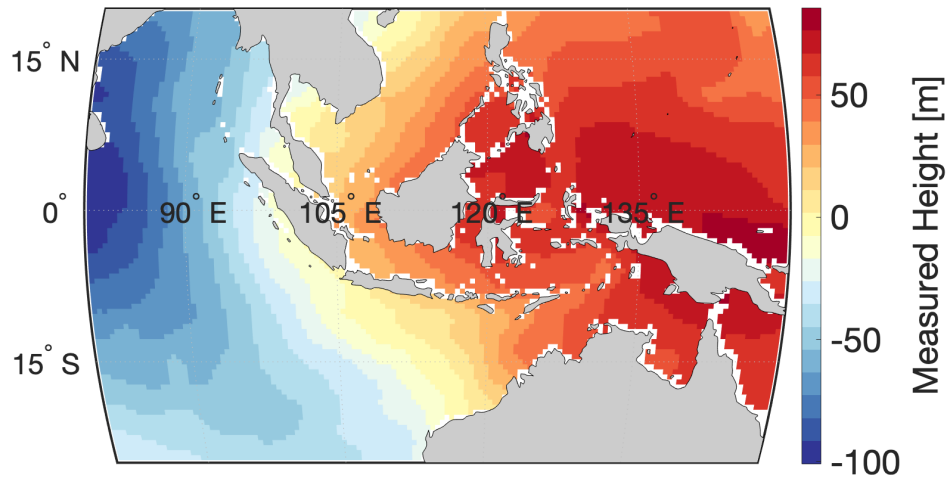
Table 7.2: CYGNSS specific table of error contributions. Final RSS values assume UKF orbit solutions, daytime ionospheric errors and 1 sec incoherently averaged observations.

| Name   | Information Source  | Uncorrected Magnitude                     | Post-processing Residual Error                       |
|--|---|---|--|
| CYG orbit                                    | Downlinked<br>Position Solutions                                    | 3 m position                              | 0.11 m ( $1\sigma$ Gipsy)<br>0.70 m ( $1\sigma$ UKF) |
| GPS orbit                                    | [Dow et al., 2009; IGS]   | 1 m position                              | 0.03 m position ( $1\sigma$ )                        |
| DTU10 MSS                                    | [Andersen, 2010]  | 100 m height                              | 0.1 m height ( $1\sigma$ )                           |
| Ionospheric delay                            | [Komjathy, 1997; Montenbruck and Gill, 2002]<br>[Roma et al., 2017] | < 15 m delay (day)<br>< 7 m delay (night) | < 3.5 m delay (RMS)<br>< 2 m delay (RMS)             |
| Tropospheric delay                           | [Leandro et al., 2006]  | 6 m delay                                 | 0.05 m delay ( $1\sigma$ )                           |
| Antenna baseline                             | Metadata  | 1 m delay                                 | 0.001 m delay ( $1\sigma$ )                          |
| add_range_to_sp<br>truncation                | Metadata  | $\pm 15$ m delay                          | 4.6 m delay ( $1\sigma$ )                            |
| Open loop delay-<br>Doppler smearing         | SGR-ReSI operations   | $\leq 1$ m delay                          | $\leq 1$ m delay                                     |
| Tracking error noise<br>(at mean SNR = 15dB) | P70 (1s obs)<br>VZ18WAVE (1s obs)<br>VZ18DDM (1s obs)               | -<br>-<br>-                               | 10 m<br>5.5 m<br>2 m                                 |
|  |   | $RSS_{P70}$                               | = 11.6 m delay                                       |
|  |   | $RSS_{VZ18WAVE}$                          | = 7.9 m delay  |
|  |   | $RSS_{VZ18DDM}$                           | = 5.9 m delay  |

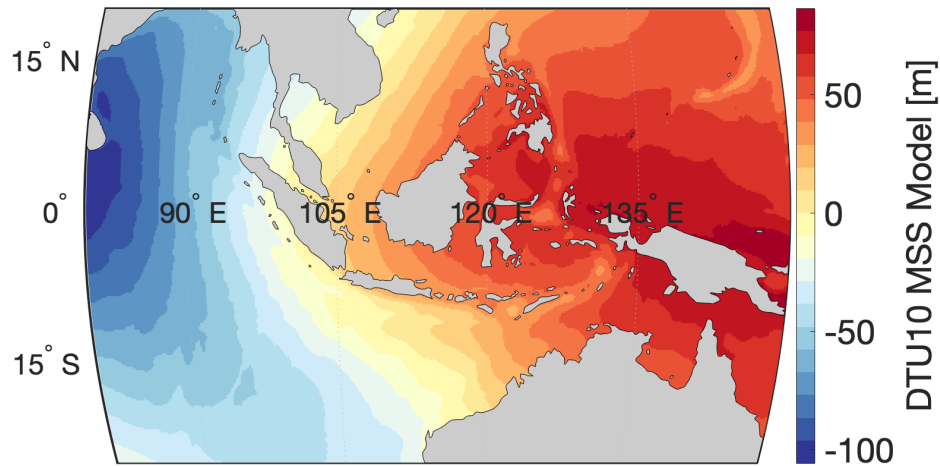
The tracking error estimates presented in Table 7.2 are based on re-tracking of synthetic observations (VZ18 modeled DDMs) corrupted with random sample noise, as presented in Chapter 6 Section 6.2.5. P70, VZ18WAVE, and VZ18DDM re-tracking methods were applied to synthetic observations with configurable noise levels. Two simplifications in our analysis make the resulting tracking error estimates optimistic compared to the performance with flight data. First, speckle noise has been neglected when simulating the noise signal. Second, the model re-trackers are being compared to noise-corrupted realizations from the same model, VZ18. Any mis-modeling compared to the real CYGNSS observations will increase the observed tracking error. Finally, the noise model used is simply Gaussian white noise. The correlation between noise on adjacent samples in the DDM is not considered. This leads to a better predicted improvement from the VZ18WAVE to the VZ18DDM method than is actually observed. Regardless of these limitations, the predicted P70 tracking delay,  $\sigma_T^{P70} \approx 10$  m at  $SNR = 15$  dB, does match very well with the observed delay anomaly precision,  $\sigma_{\Delta\delta}^{P70} = 10.5$  m delay at  $SNR = 15$  dB (see P70 results in Figure 6.15).

### 7.6.1 Effects of Precise Orbit Determination

Currently, onboard position solutions are identified as the third largest error source in the altimetric retrieval. To investigate the potential benefit of precise orbit determination for CYGNSS, additional data packets, that include the single-frequency pseudorange and carrier phase observations made on-orbit, were downlinked from CYGNSS FM04 from April 20 - 28, 2018. Bruce Haines (NASA JPL) used the precise orbit determination capabilities of the GipsyX software [NASA Jet Propulsion Laboratory, 2018] to process the pseudorange measurements. High fidelity forcing models and ionospheric models were incorporated to produce the best possible orbit solutions with the measurements available. Carrier phase observations could not be used due to an undiagnosed clock discrepancy between the two data types. It is expected that if the measurements issue can be resolved, an even better position solution will be possible.



(a)



(b)

Figure 7.3: CYGNSS retrieved surface heights in Indonesia compared to the DTU10 MSS model. (a) CYGNSS observations are used to observe the ocean surface height with respect to the WGS84 ellipsoid around Indonesia. These height retrievals match the large-scale characteristics of the DTU10 mean sea surface model shown in (b). 1 second data from 5 days in April 2018 re-tracked with the VZ18DDM method are smoothed with a 0.8 deg Gaussian kernel filter to produce the measured surface heights shown here.

A second approach is taken here to filter the CYGNSS 1 sec position solutions with an unscented Kalman filter (UKF) modeling the orbital dynamics [Tapley et al., 2004]. Both

the GipsyX and UKF solutions have similar differences from the original CYGNSS positions,  $RMS_{3D} \approx 3$  m. To estimate the accuracy of the GipsyX and UKF solutions, the formal 3D position covariance is used. The 3D position covariance for the GipsyX solutions gives  $\sim 11$  cm  $1\sigma$  and of the UKF solutions reports  $\sim 70$  cm  $1\sigma$ .

Height retrievals from FM04 using the GipsyX pseudorange orbits and VZ18DDM re-tracking have a standard deviation of  $\sigma_H^{GX} = 3$  m. Retrievals using the UKF filtered orbits and VZ18DDM re-tracking have a standard deviation of  $\sigma_H^{UKF} = 3.5$  m. For comparison, using P70 re-tracking and the original CYGNSS FM04 orbits, the height retrievals have a standard deviation of  $\sigma_H = 4$  m.

Component-wise, changes to the radial component of the receiver position solution will have a direct effect on height anomaly. In-track and cross-track orbit error components will have a more subtle effect. Figure 7.4 shows how the radial, in-track, and cross-track orbit components, between the original and GipsyX filtered solutions, influence the height anomaly from CYGNSS FM04, and the distribution of the orbit differences.

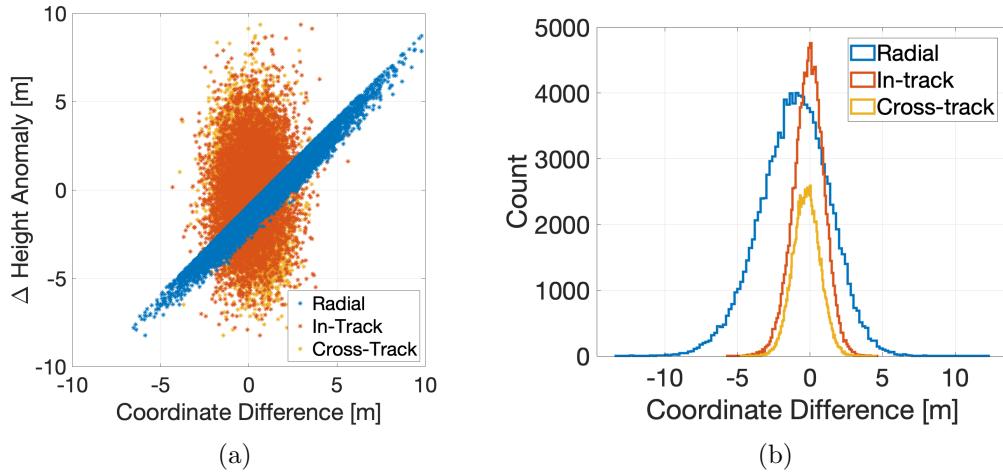


Figure 7.4: Change in height anomaly from the GipsyX orbit solutions decomposed into radial, in-track, and cross-track components. (a) Change in height anomaly versus change in receiver orbit decomposed into radial, in-track, and cross-track components. (b) The distribution of the decomposed orbit differences, between the GipsyX orbit and original CYGNSS orbit.



Figure 7.5 shows a time series of the change in height anomaly from CYGNSS FM04 across a long pass over open ocean east of Sumatra and Australia. This result compares the GipsyX pseudorange orbits to the original CYGNSS solutions. It can be seen that the change to height anomaly is small but not insignificant along a track, in this case ranging a few meters. Statistically, over a week of data, the improvement in height precision is small, with a change in standard deviation less than 1 m. Clearly, there are larger errors still present (e.g. re-tracking error and ionosphere) that mask any changes brought by precise orbit determination.

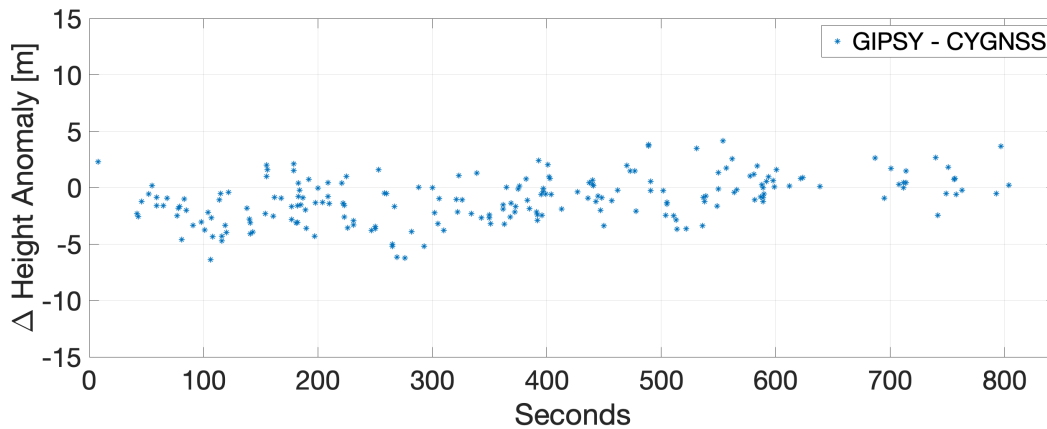


Figure 7.5: Change in height anomaly from original CYGNSS orbits to GipsyX pseudorange orbits along a single 800 sec track.

### 7.6.2 Re-tracking in the Presence of Coherent Signals

The VZ18WAVE and VZ18DDM re-tracking methods described in Chapter 6 have been tested with the CYGNSS Indonesia data. With 2% – 4% of the data indicating strong coherent reflections, depending on the day and time of year, these data will stress the ability of the VZ18WAVE and VZ18DDM methods to track observations from a mix of surface conditions.

### 7.6.2.1 VZ18WAVE Tracking Results

The VZ18WAVE re-tracking performance with coherent observations is compared to the P70 tracking performance. A subset of  $N = 34,000$  CYGNSS ocean observations from August 18 - 22, 2017 were used to compare the two methods. These observations were chosen because they have relatively high SNR and span a wide range of coherence conditions from strongly coherent to completely diffuse. The waveform model based approach is seen to be better at tracking strongly coherent observations than the P70 method, but the VZ18WAVE results are still biased for observations in the transition zone between fully coherent and incoherent. Figure 7.6 shows how the VZ18WAVE algorithm compensates for reflection coherence, quantified by delay waveform width. Much of the negative trending bias towards narrow waveform width is corrected by the VZ18WAVE re-tracking. The VZ18WAVE method does, however, over-compensate for observations with widths between 0.6 – 0.8 chips. The VZ18WAVE delay anomaly precision is comparable to P70 for widths greater than 0.9 chips with delay anomaly  $\sigma_{\Delta\delta} \approx 12.5$  m on these 1-sec integrated observations. The dramatic systematic bias reduction,  $\sim 70$  m for very narrow observations, is a significant improvement over P70. However, the over correction behavior for transition zone observations is indicative of some mis-representation of the CYGNSS observations by the VZ18 model waveforms.

When producing spatially-averaged height retrievals, VZ18WAVE re-tracking does significantly reduce the systematic, non-physical signals across the Indonesia zone, as compared to P70 tracking seen in Figure 7.7. Most of the negatively biased values in the western ocean are corrected toward  $\Delta h = 0$  by the VZ18WAVE tracking. The measured height values in the Figure 7.7 maps have been smoothed with a Gaussian kernel filter ( $\sigma_{GF} = 0.85$  deg) to reduce random scatter and better highlight the underlying systematic patterns.

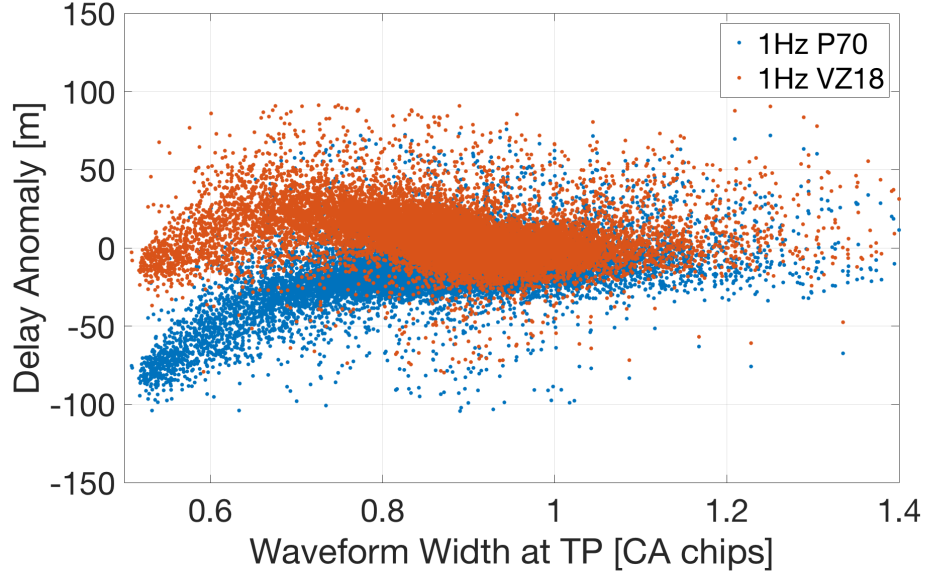
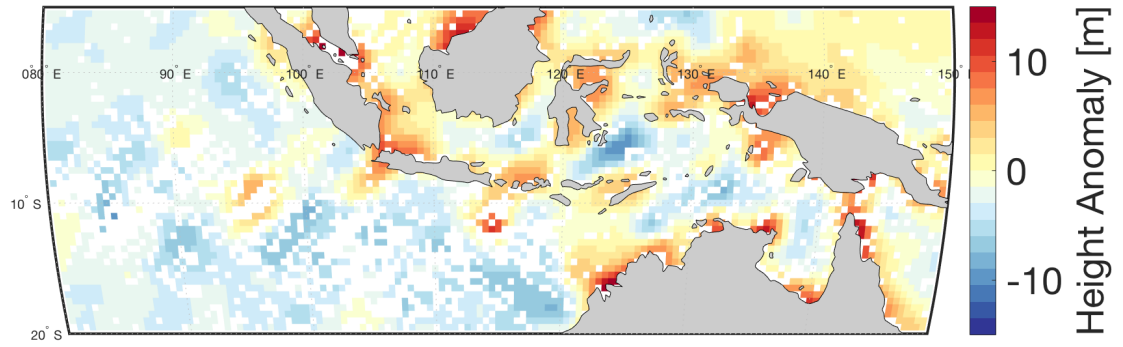


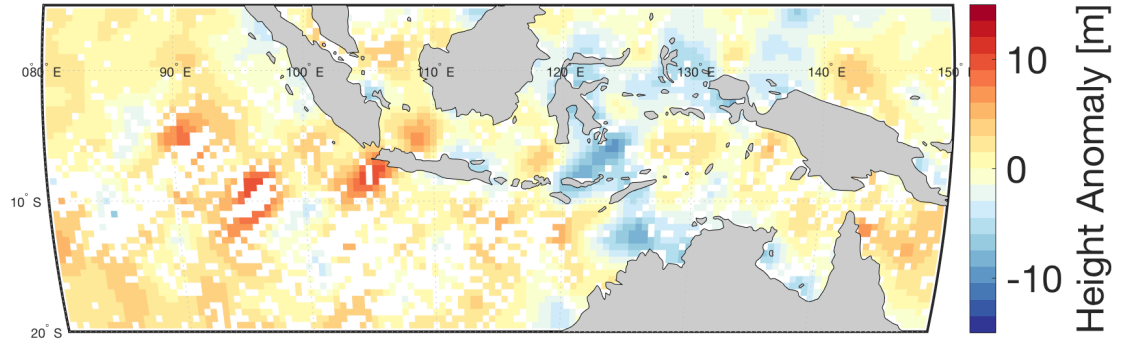
Figure 7.6: Delay anomaly versus waveform width comparing P70 and VZ18WAVE. VZ18WAVE re-tracking improves upon P70 but over-compensates for measurements with width between 0.6 - 0.9 C/A chips.

#### 7.6.2.2 VZ18DDM Tracking Results

The next step is to compare the VZ18DDM method to P70 and VZ18WAVE re-tracking. A new subset of data with  $N = 50,000$  observations is chosen. Figure 7.8 shows that VZ18DDM further improves the way coherent reflections are re-tracked. The delay anomaly overcompensation seen with VZ18WAVE is not seen with VZ18DDM. Instead the DDM model fits yield a delay anomaly that is less systematically biased as a function of waveform width. The delay anomaly precision is similar to P70 for waveform width  $> 0.9$  chips. The VZ18DDM delay anomaly standard deviation is  $\sigma_{\Delta\delta} = 12.5$  m. The improvement in performance over VZ18WAVE is likely due to more data used in the VZ18DDM fit, and its ability to correct for Doppler errors in the CYGNSS open-loop prediction. The biases observed in Figure 7.8 for very narrow observations continue to indicate some mis-modeling of the CYGNSS observations. Some of the potential limitations of the implemented VZ18 model, discussed in more detail in Chapter 5, include a limited wave spectrum to simulate



(a)



(b)

Figure 7.7: CYGNSS height anomaly in Indonesia with P70 and VZ18WAVE re-tracking. (a) P70 height anomaly from selected Indonesian zone. (b) VZ18WAVE height anomaly from selected Indonesian zone. These height anomaly results have been smoothed with a Gaussian kernel filter with  $\sigma = 0.85$  deg (FWHM = 2 deg).

ocean surface roughness, approximate geometries for receiver altitude and azimuth, and ap-

proximate representation of the receiver specific characteristics such as sampling bandwidth.

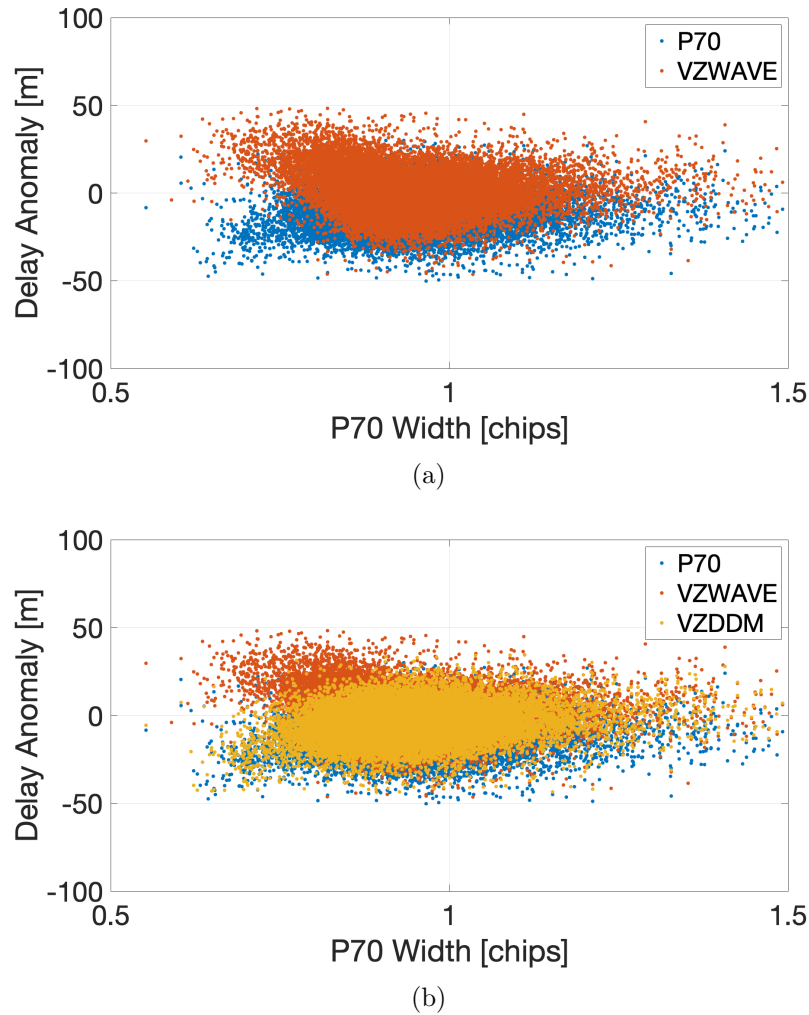


Figure 7.8: VZ18DDM delay anomaly vs correlation waveform width. (a) VZ18WAVE and P70 delay anomaly versus waveform width. (b) VZ18DDM delay anomaly versus waveform width. The VZ18DDM results do not share the delay anomaly over-correction for transition zone observations that VZ18WAVE does. These data are from day 230 - 234, 2017.  $N = 50,000$ .

## 7.7 CYGNSS Height Retrievals in Indonesia

To produce height retrieval maps, the VZ18 re-tracking methods are used primarily with time-averaged observations. That is the CYGNSS observations are smoothed with a 10 sec moving average window before re-tracking with VZ18WAVE or VZ18DDM to re-

duce sample noise and improve signal-to-noise-ratio. The height retrieval maps may also be smoothed with a Gaussian kernel filter. A Gaussian kernel with  $\sigma = 0.8$  deg (or full width at half maximum  $FWHM = 2$  deg) is chosen following the results by Clarizia et al. [2016]. Averaging across the surface in this way helps to reduce the random error in the height retrievals and highlight any underlying systematic patterns.

Time averaging the CYGNSS observations has another, unintended effect on the measured waveform width. DDM samples at delays past the correlation function peak tend to have more noise than those on the DDM leading edge [Martín et al., 2014]. Therefore, the leading edge slope is relatively stable compared to the trailing edge slope. The measured waveform width is sensitive to and altered directly by noise on the DDM trailing edge samples impacting the correlation function slope. Noisy trailing edge samples may then give the impression that the surface reflections are fluctuating between coherent and incoherent on time scales less than 10 sec. It is expected, however, that the ocean surface roughness should be consistent over distances longer than  $\sim 70$  km (roughly the horizontal distance traveled in 10 sec by CYGNSS in LEO with speed  $\sim 7$  km/s). Some of those strongly coherent observations, with very narrow waveform width, are then averaged with wider observations adjacent in the time-series. The result is a reduction in the number of observations that can be classified as coherent by the waveform width metric when 10 sec averaging is used.

In the following results, UKF filtered orbit solutions are utilized along with P70, and VZ18DDM re-tracking. The GipsyX pseudorange orbits are arguably more accurate, but the difference is small and the availability of GipsyX solutions is limited only to CYGNSS FM04. Figures 7.9, 7.10, and 7.11 show the 1 sec and 10 sec height anomaly maps for the P70 re-tracking method along with the 10 sec results for the VZ18DDM method. The (a) subplots show the height anomalies before surface averaging across with a Gaussian kernel filter. The (b) subplots include the spatial filtering. Note the change in color-bar range between 1 sec and 10 sec results.

Both of the 10 sec time-averaged results with P70 and VZ18DDM tracking perform

well, and significantly better than the 1 sec P70 results. Much of the random height anomaly error is reduced by smoothing the CYGNSS observations. There is, however, a large cost to spatial resolution. Results from 1 sec observations have a footprint that is approximately averaged along 7 km horizontal distance. Averaging for 10 seconds increases the average to 70 km horizontally. Such a large loss in spatial resolution is not acceptable if the goal is to resolve meso-scale ocean topography. However, as an analysis tool, the 10 sec results in Figures 7.10(a) and 7.11(a) help to highlight regions that still have persistent height anomaly biases and are useful for diagnosing the potential cause of such biases.

Measurement averaging in the spatial domain is examined as well. A Gaussian kernel filter with standard deviation  $\sigma = 0.8$  deg is used to smooth the height anomalies across the surface. This kernel filter yields approximately a factor of 2 improvement in height anomaly standard deviation for 10 sec observations. Similar to the time-averaged results, the height anomaly error is reduced, but spatial resolution is as well. With a  $\sigma = 0.8$  deg Gaussian kernel filter, the reduction in spatial resolution is even more significant as measurements from over 2 deg latitude/longitude are now correlated. Figures 7.9(b), 7.10(b), and 7.11(b) show the Gaussian smoothed height anomalies from P70 (1 sec), P70 (10 sec), and VZ18DDM tracking. In these maps, the surface becomes smooth, and the random, high-frequency error is largely removed, but the residual meter level, non-physical topographic error signals are still present and dominate the estimated height anomaly.

Table 7.3 lists the observed height precision for each of these cases. Clearly the time averaged results are significantly improved over the 1 sec results. The precision of the 10 sec VZ18DDM and 10 sec P70 heights are nearly identical. Smoothing the observations in time reduces re-tracking biases associated with coherent reflections.

The residual systematic patterns in Figures 7.10(b), and 7.11(b) are too large to be physical oceanographic signals. Such systematic errors are likely due to atmospheric delay mis-modeling, tracking biases due to the presence of strong coherent observations, or orbit errors. To try to isolate the cause of the residual systematic effects in height anomaly,

Table 7.3: Surface height retrieval standard deviation with the P70 and VZ18DDM re-tracking methods. Single sample and Gaussian smoothed results from 1 second and 10 second observations are listed.

| Tracking Method  | Single Sample<br>$\sigma_H$ [m] | Gaussian Smoothed<br>$\sigma_H$ [m] |
|------------------|---------------------------------|-------------------------------------|
| P70 (1 sec)      | 6.7                             | 1.9                                 |
| VZ18WAVE (1 sec) | 10.9                            | 3.2                                 |
| VZ18DDM (1 sec)  | 5.8                             | 1.9                                 |
| P70 (10 sec)     | 3.6                             | 1.3                                 |
| VZ18DDM (10 sec) | 3.8                             | 1.3                                 |

ascending and descending tracks were separated. Separating ascending and descending tracks effectively isolates night and day observations. This separation can help to isolate Earth surface modeling errors and timing errors (like those seen with TDS-1) from ionospheric modeling errors. Figure 7.12 shows the Gaussian smoothed delay anomalies for night-time, ascending (a, c, and e), and day-time, descending tracks (b, d, and f), along with the waveform width, and correlation SNR. There are some qualitative differences between the two maps, but largely, the delay anomalies in both day and night cases are correlated with waveform width and SNR. Where there are strongly coherent observations, the delay anomaly is biased to the negative. This indicates that improperly accounting for reflection coherence is still a large, dominant effect regardless of the presence of ionospheric effects. Thus, there are improvements to be made in re-tracking strong coherent reflections. The larger delay biases seen in the daytime, as compared to nighttime passes, indicate the presence of unmodeled ionospheric effects.

## 7.8 Conclusions

The CYGNSS data collected over Indonesia have proven a valuable resource to study GNSS-R altimetry. Methods previously developed for aircraft campaigns (Chapter 3) and earlier spacecraft missions (Chapter 4) have been adapted to this case and improved upon to produce the most precise conventional GNSS-R sea surface height retrievals to date.



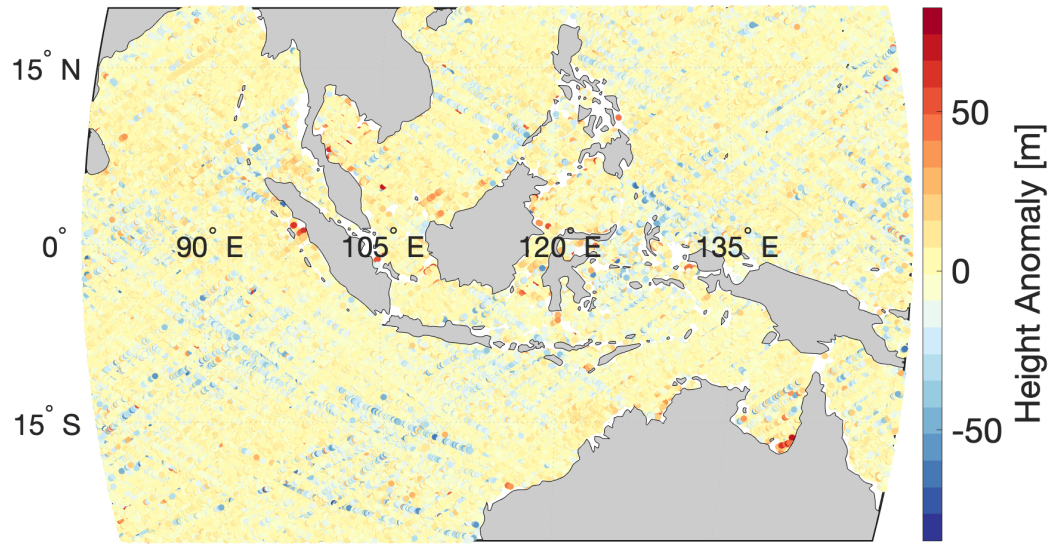
Unfortunately, the results with 1 sec observations do not meet the requirement specified by Li et al. [2016] of  $\sigma_H \leq 1$  m for the retrieval of meso-scale ocean topography. Nonetheless, the methods demonstrated here are shown to produce state-of-the-art height retrievals and help to prioritize design considerations for future missions. Future data sets generated with an altimetry-optimized GNSS-R instrument should be capable of a result matching Li's standard. The RSS residual error of the CYGNSS altimetry observations is estimated to be 6 m delay at the average observed CYGNSS SNR using VZ18DDM tracking on 1 sec observations (Table 7.2). If GPS P(Y) code or GPS L5 measurements were available instead, that delay error would improve by a factor of 10 for the same signal power levels. Practically, using the P(Y) codes would require a cross-correlation approach resulting in losses to the observed SNR. If even a factor of 3 improvement is achieved, the mesoscale utility would be realized.

Additionally, the utility of the VZ18 model for modeling and delay re-tracking of the CYGNSS observations has been shown. Proper consideration of weak and strong diffuse reflections, with the VZ18WAVE and VZ18DDM re-tracking algorithms, allows for accurate surface height observation from a range of surface conditions. GNSS-R altimetry observations are now more robust to the presence of coherent reflection conditions therefore increasing the reliability and accuracy of retrievals. There is certainly still room for improvement, in both path delay and observation modeling. Some of the VZ18 models, like the auto-correlation filter bandwidth and the CYGNSS antenna pattern, are approximate representations of the unique spacecraft installations. Tailored antenna maps and models may produce improved performance. Other model parameters, like the VZ18DDM azimuth resolution could be reduced (currently 10 deg spacing). Finally, better characterization of the GNSS-R instrument, spacecraft orbits, and the observation scenario are obvious directions for future works.

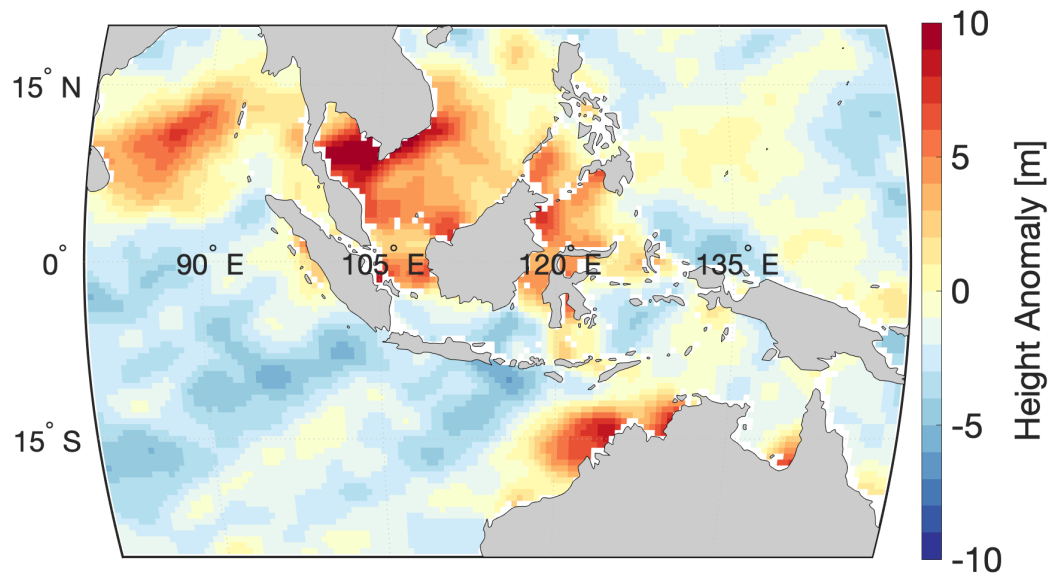
## **Acknowledgments**

The CYGNSS Level 1 Science Data Record Version 2.1 data were obtained from the NASA EOSDIS Physical Oceanography Distributed Active Archive Center (PO.DAAC) at the Jet Propulsion Laboratory, Pasadena, CA (<http://dx.doi.org/10.5067/CYGNS-L1X20>).

Part of this work was funded by the Jet Propulsion Laboratory, California Institute of Technology under subcontract # 1576219.

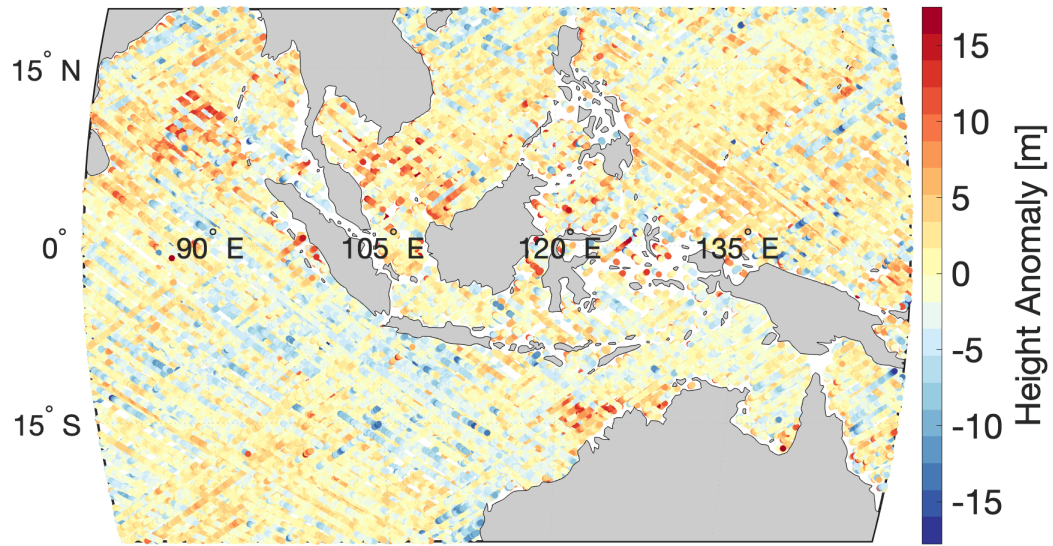


(a)

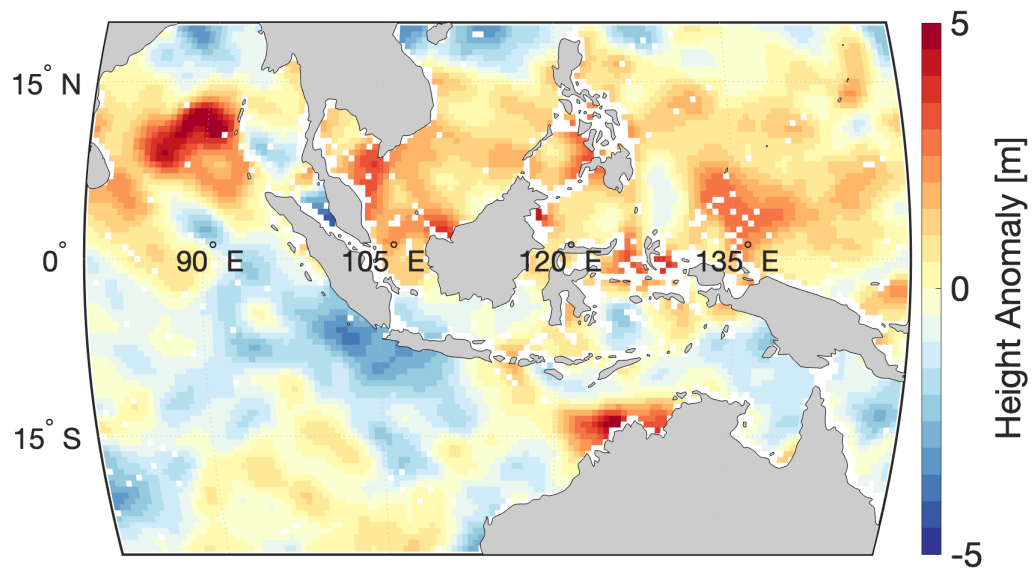


(b)

Figure 7.9: P70 1 sec height anomaly in Indonesia. (a) Single sample and (b)  $\sigma = 0.8$  deg Gaussian smoothed results with P70 retracking of 1 sec observations.

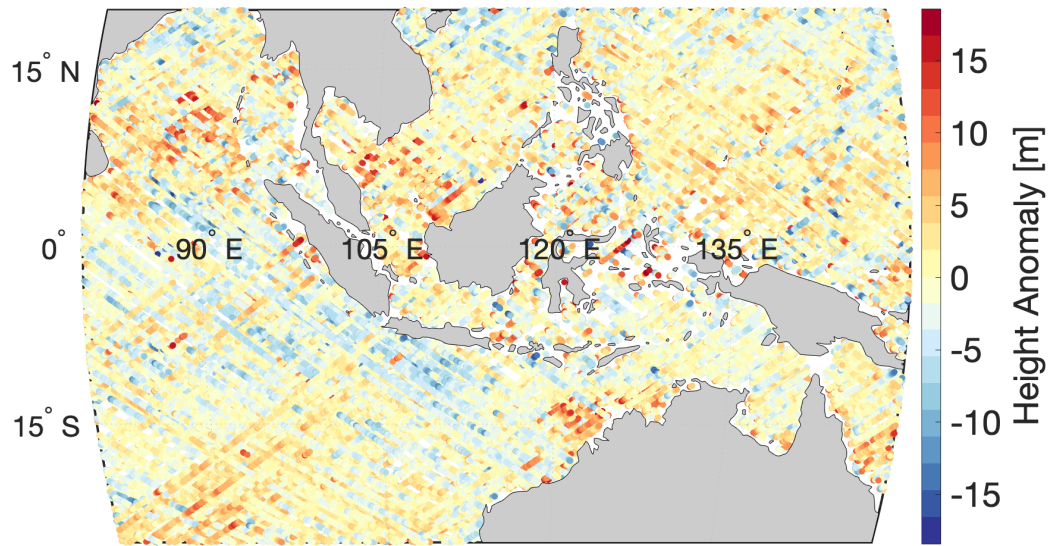


(a)

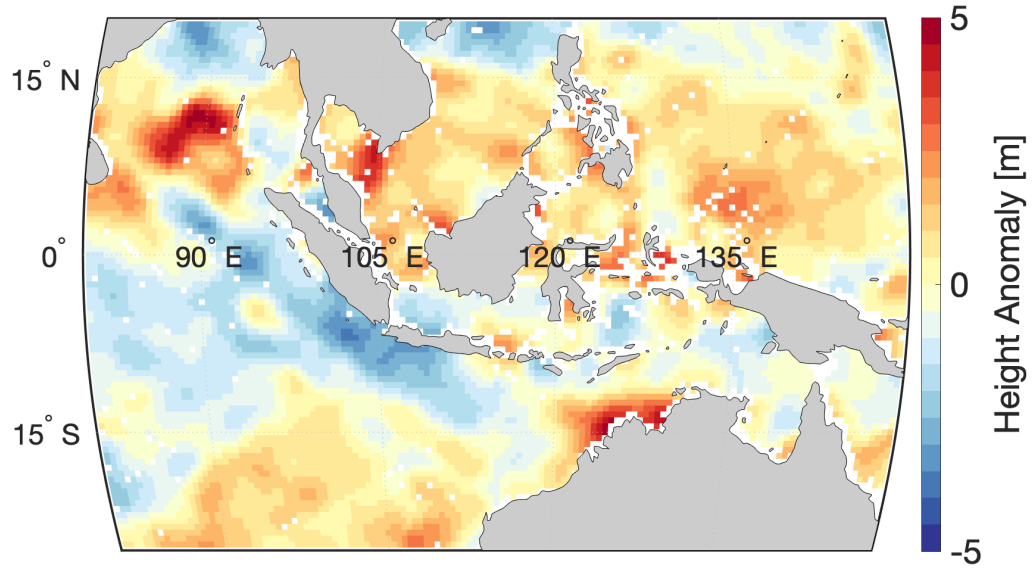


(b)

Figure 7.10: P70 10 sec height anomaly in Indonesia. (a) Single sample and (b)  $\sigma = 0.8$  deg Gaussian smoothed results with P70 retracking of 10 sec observations.



(a)



(b)

Figure 7.11: VZ18DDM 10 sec height anomaly in Indonesia. (a) Single sample and (b)  $\sigma = 0.8$  deg Gaussian smoothed results with VZ18DDM retracking of 10 sec observations.

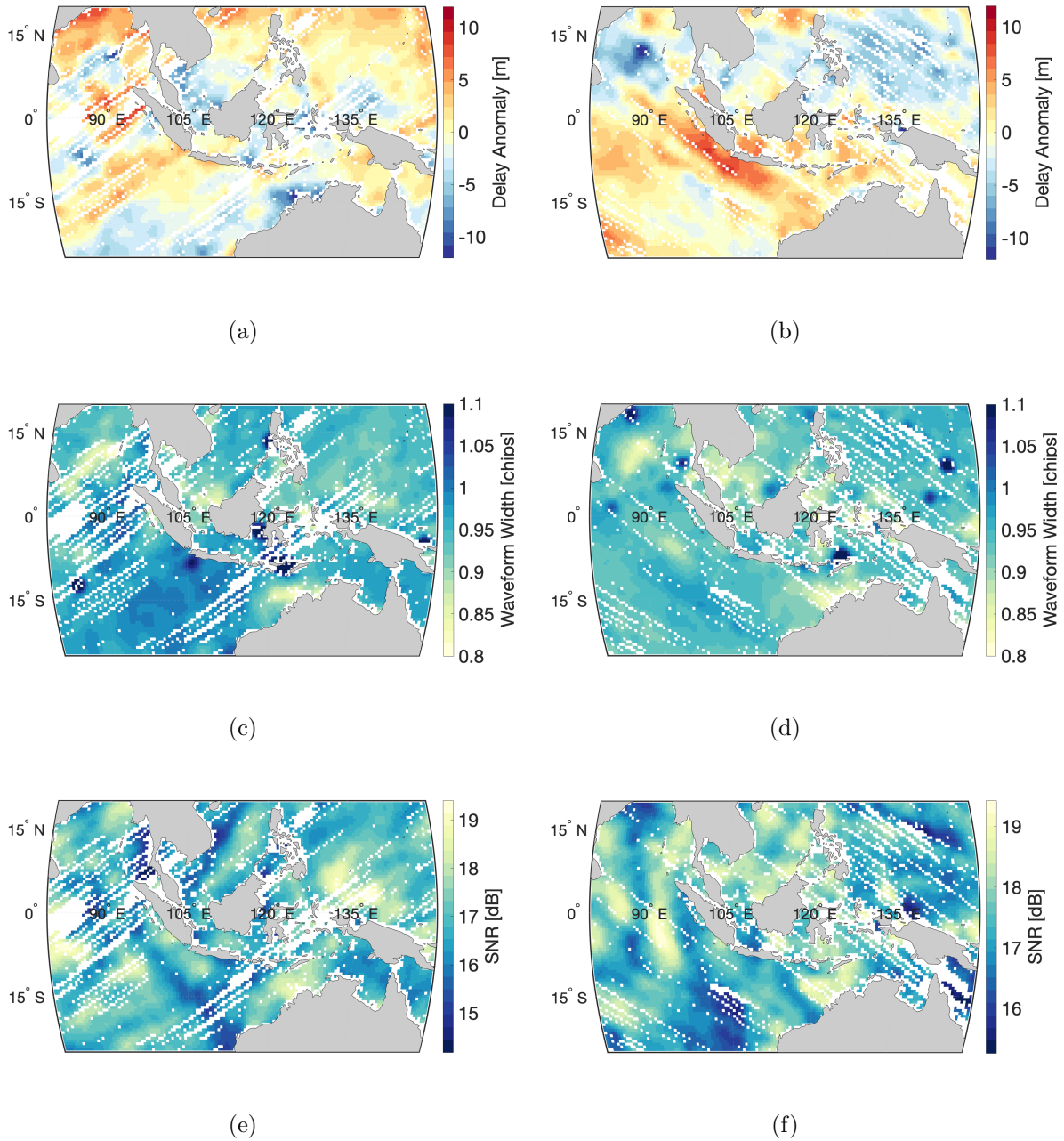


Figure 7.12: Ascending and descending track delay anomaly, waveform width, and SNR. Gaussian smoothed VZ18DDM delay anomaly (a)(b), waveform width (c)(d), and correlation SNR (e)(f). A correlation is observed between the remaining systematic delay anomaly signals and waveform width. Where there are narrow waveforms, the delay anomaly also tends toward negative. (left) Ascending track, night-time observations are shown. (right) Descending, day-time observations are shown.



## Chapter 8

### Sea Ice Detection Methodology and Preliminary Results

#### 8.1 Introduction

Maximum winter sea ice extent has been in decline in both the Arctic and Antarctic regions for several decades [Serreze et al., 2000]. In recent years, space-based remote sensing of sea ice has enabled the continuous monitoring of ice extent and concentration that shows such declining trends. Typically, microwave radiometers are used for the remote sensing of sea ice from space. These instruments, like the AMSR/-2/-E, operate between 6 – 90 GHz and have a spot size on the ground on the order of 10 – 2000 km<sup>2</sup> [NSIDC, 2001]. GNSS-R, of course, also uses microwave wavelengths, sharing the benefit of all weather capability, with a measurement footprint comparable to the highest resolution microwave radiometers [Alonso-Arroyo et al., 2016].

As with altimetry, GNSS-R assumes a complimentary role to improve coverage, spatially and temporally, of sea ice measurements. Higher density observations can inform regional analysis as well as complete Arctic/Antarctic studies. Similar studies have been completed by Alonso-Arroyo et al. [2015]; Park [2017]; Yan and Huang [2016] To that end, a method is presented to distinguish between ice and open-water reflections. The methodology is reliable, accurate, and easy to implement. The following sections describe the experimental dataset, the ice-water detection procedure, and some preliminary results.

## 8.2 TDS-1 GNSS-R Data and Ancillary Sea Ice Data

Data from the TDS-1 mission archive are used to study the potential for GNSS-R sea ice detection. The TDS-1 spacecraft is in a high-inclination sun-synchronous orbit providing a good vantage to observe polar sea ice. Data from RD17 and RD18 spanning 4 days spread over two weeks in February 2015 are used here. This includes more than 2500 observations.

Truth reference is based on the AMSR-2 Sea ice concentration product and sea ice edge product of the EUMETSAT Ocean and Sea Ice Satellite Application Facility (OSISAF, [www.osi-saf.org](http://www.osi-saf.org)) [EUMETSAT, 2017]. The OSISAF sea ice concentration products are computed from atmospherically corrected brightness temperatures from a combination of the 19, 37, and 91 GHz channels of the Special Sensor Microwave Imager/Sounder (SSMIS) sensors [Bommarito, 1993]. Uncertainty in sea ice concentration is estimated to be between 1 – 6% in winter [Yan and Huang, 2016].

## 8.3 Ice Detection Methodology

Reflections from smooth surfaces yield a coherent, specular, reflection. In GNSS-R, the corresponding cross-correlation function from a coherent reflection looks similar to the cross-correlation with a direct signal. Reflections from rough surfaces are the result of diffuse scattering, and therefore the correlation function is spread in delay and Doppler space. Figure 8.1 illustrates example DDMs from the TDS-1 data set that highlight the differences between coherent and diffuse reflections. It is expected that reflections from sea ice will have a strong coherent component, as generally, the ice surface is smooth relative to the signal wavelength. Open water on the other hand, typically produces a more incoherent reflection due to scattering from waves [Belmonte-Rivas, 2007]. Observations from the TDS-1 data sets support these predictions.

We investigated the use of correlation waveform width as a proxy for the coherence of an observed reflection, allowing us to quantify the distinction between ice and water surfaces.



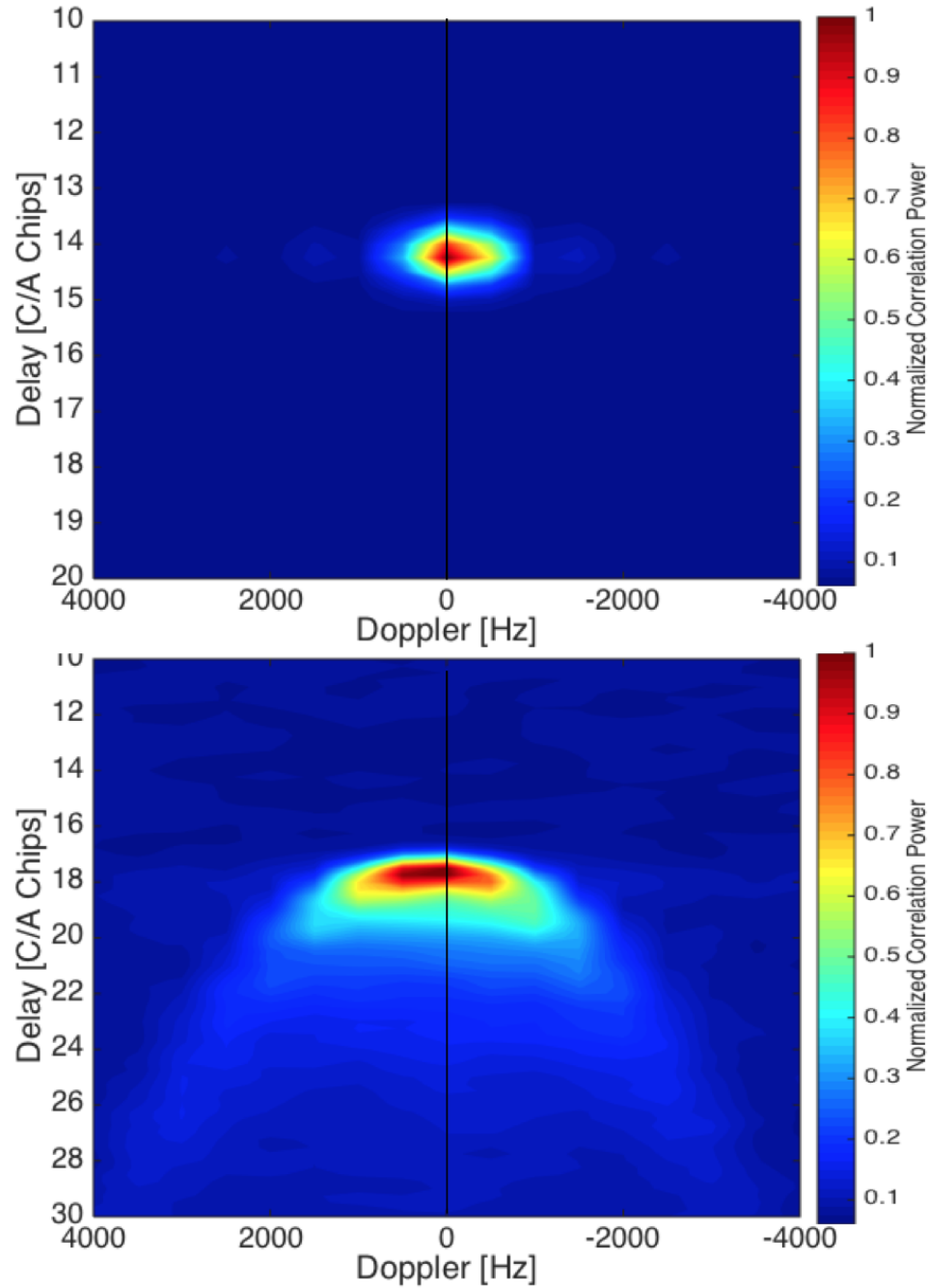


Figure 8.1: Example ice and water DDMs from TDS-1. These example DDMs illustrate the characteristic shape of a nearly specular ice reflection (top), and a diffuse open water reflection (bottom).

Here, the width of the delay waveform at 50% power and the correlation function SNR are used as metrics to quantify coherence. Figure 8.2 illustrates the observed correlations

between waveform width and SNR. Each observation is characterized in color based on OSISAF sea ice concentration [EUMETSAT, 2017]. The reflections are clearly split in width and SNR according to ice concentration. A threshold is defined (the red line in Figure 8.2) and a binary ice/water detection is used. Reflections below the threshold are classified as ice.

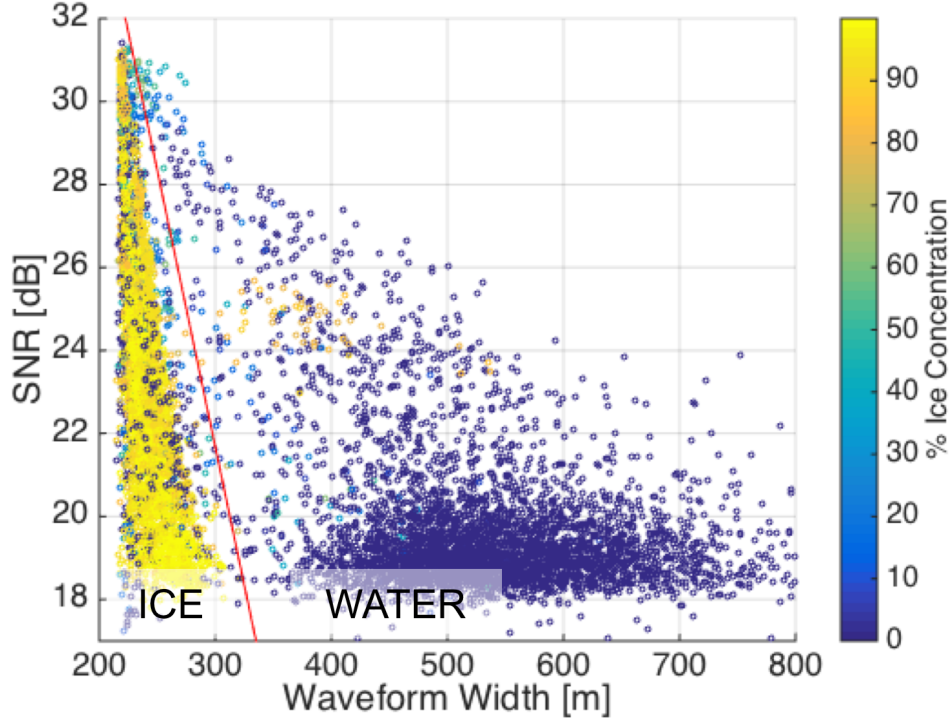


Figure 8.2: Distribution of arctic reflection events by correlation SNR and delay waveform width. The points are colored corresponding to the OSISAF daily sea ice concentration product at the specular point. The red line shown defines the threshold used to distinguish between ice and water reflections.

#### 8.4 Ice Detection Results

Following the methodology described above, a binary ice detection scheme is compared to the OSISAF sea ice concentration product. To compare ice concentration with the binary GNSS-R detection, locations that have  $> 30\%$  ice coverage in the OSISAF concentration product are said to be ice covered. Table 8.1 lists the positive, missed, and false detection

rates. Positive detections are those for which both the GNSS-R binary method and OSISAF product both show ice. Missed detections are those that the GNSS-R binary method show water while the OSISAF concentration products show ice. False detections are the reverse of missed detection.

Table 8.1: Arctic GNSS-R sea ice detection results as compared to the OSISAF sea ice concentration products. GNSS-R data are taken from the TDS-1 data sets RD17 and RD18.

|                    | <b>Percentage (%)</b> | <b># Samples</b> |
|--------------------|-----------------------|------------------|
| Positive detection | 97%                   | 2663             |
| Missed detection   | 3%                    | 73               |
| False detection    | 2%                    | 51               |

Missed and false detections are most often observed near the edges of the ice sheet where ice concentration is low. Figure 8.3 illustrates where missed and false detections are observed in the Sea of Okhotsk and the Bering Sea. These areas near the ice edge experience rapid freeze and thaw. Changes in sea ice concentration of  $\pm 60\%$  or more were observed in the OSISAF data during the time these data were collected by TDS-1 (about 2 weeks time). Areas of water near the ice sheet edge may also be dampened, and diminish the diffuse scattering, leading to false-positives. Such dynamic conditions on the surface would indicate that there may be significant uncertainty in comparing instantaneous measurements (GNSS-R observations) with daily averaged products (OSISAF). Furthermore, rapid freeze and melting might yield wet or even submerged ice surfaces that complicate the true scattering mechanisms and reduce the effectiveness of this binary ice detection.

## 8.5 Future Work

A small sub-set of the TDS-1 data set is utilized in this study. Expanding this analysis to a larger set of data that spans the winter and summer seasons is a logical next step. Considering data from winter and summer months would test the detection scheme across a range of freezing and melting surface conditions. Additionally, characterizing the spatial

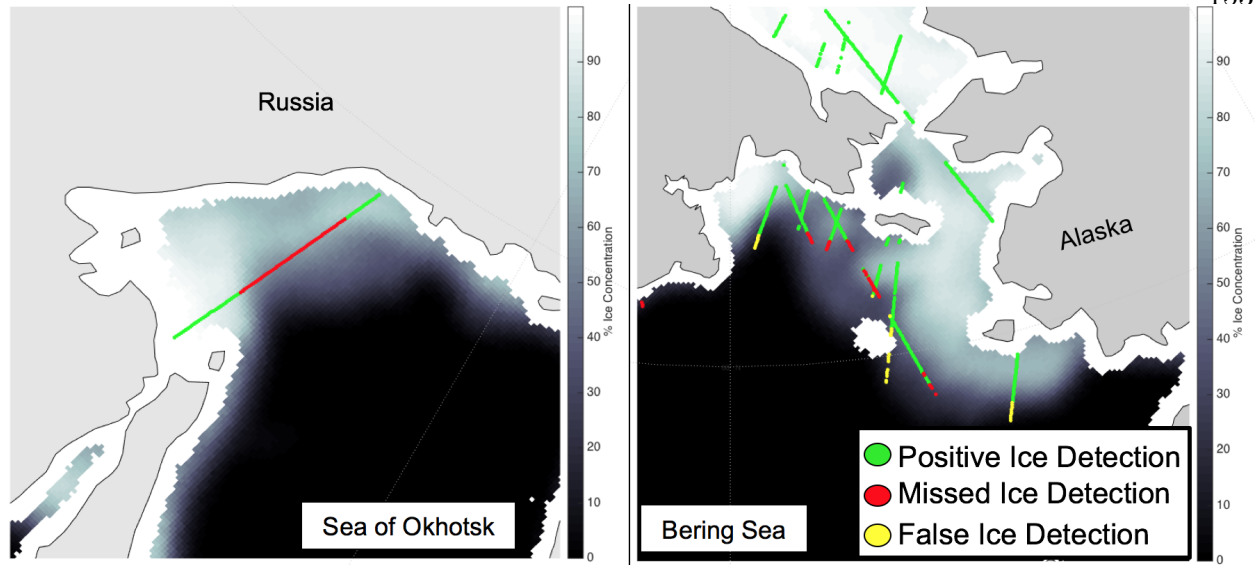


Figure 8.3: A detailed look at the Sea of Okhotsk (left) and the Bering Sea (right). Missed and false positive ice detections tend to be near the boundary of the sea ice extent. In these regions the ice concentration is low and highly variable with rapid freeze and thaw. The black-white color gradient represents the OSISAF daily sea ice concentration product.

resolution of 1 Hz GNSS-R sea ice observations is necessary before further comparing to other sea ice observation sets.

## Chapter 9

### Conclusions and Future Work

#### 9.1 Research Summary

This work was motivated by a community interest in advancing the ocean and sea ice observing capabilities of GNSS-R, and a need for ancillary data types in those fields. A set of methods and analysis techniques to produce state-of-the-art altimetric and sea ice detection retrievals have been developed. These methods for retrieval are based on findings from experimental data sets from aircraft and spacecraft GNSS-R platforms. Working with these data sets has resulted in the refinement of analysis techniques to compensate for and understand the practical aspects of the flight data.

The models and analysis tools are implemented in such a way that they can be adapted and generally applied to future data sets. Methods for the consideration of receiving platform positioning, precise Earth surface topography, ionospheric and tropospheric errors, platform-specific limitations, and the tracking of both strongly coherent and diffuse reflections are implemented and demonstrated. The studies presented here lay the ground work such that a GNSS-R mission dedicated to altimetry or ice observation might utilize these methods, and produce results with accuracy and precision of value to the ocean and polar science communities.

The most significant contributions of this work include the development of a precise model for the GNSS-R reflected path and characterization of single point and model based delay re-tracking algorithms. First, precise modeling of the reflected path allows for the

correction of systematic, signal-propagation delay biases that would otherwise contaminate the altimetric retrieval. Second, understanding the performance of the altimetry delay re-tracking algorithms for a range of conditions, related to the receiver platform and the surface scattering regime, is important for selecting the right approach to create a robust, accurate result. Together, these developments produce the most precise conventional GNSS-R altimetry retrievals to date.

The space-based altimetry results presented in this dissertation are state-of-the-art. However, they do not yet meet the standard required to resolve meso-scale ocean topography phenomena. Li et al. [2016] states that 1 sec height observations should have precision  $\sigma_H \leq 1$  m to resolve meso-scale ocean features. While limitations imposed by the receiver designs examined here preclude the possibility of meso-scale ocean altimetry, the methods developed are applicable to future GNSS-R missions, and may be employed to meet that standard. Future missions, whether designed primarily for ocean surface altimetry or not, are likely to incorporate many features that would improve the potential for ocean science. In fact, several currently planned missions, like <sup>3</sup>CAT-2 [Carreno-Luengo et al., 2016], intend to do so. Those improved features include dual-frequency GNSS observations (eg. GPS L1 and L2), wide-band code tracking (eg. GPS P(Y) or Galileo E5 signals), and high gain antennas.

Finally, a novel sea ice detection scheme is presented on a limited data set to have a 97 % detection rate. This approach might be utilized in future space-based GNSS-R missions in high-inclination orbits to supplement comparable radiometric sea ice extent observations, helping to build continuous, high resolution maps of sea ice extent. Such measurements would be an important tool for monitoring trends in seasonal ice growth or melt. GNSS-R is shown to be able to produce dense coverage (see CYGNSS observation coverage), and accurate sea ice detections. Combined, these characteristics mean that GNSS-R ice measurements are a potentially valuable resource for polar science.

## 9.2 Considerations Moving Forward

The final results from CYGNSS show that the expected RSS delay error with CYGNSS is  $\sim 6$  m. In descending order of importance, this estimate assumes model-based re-tracking of GPS L1 C/A signals, accurate ionosphere models, and precise orbit determination. If wide-band ranging codes are used, it is reasonable to expect that delay error to improve to less than 2 m (equivalently height error  $< 1$  m). Dual frequency observations would significantly reduce the ionospheric errors. Then, precise orbit determination and accurate calibration of high gain receiving antennas may further improve the delay error, yielding a powerful new way to do ocean science.

Improved data can facilitate better results, but there is, of course, significant room for improvement on the modeling side as well. The high-fidelity delay model, and re-tracking algorithms have several limitations that should be addressed in future studies. In the absence of dual-frequency observations, a higher fidelity model of the ionosphere should be considered. Ionospheric density profiles from GNSS-RO missions are likely to improve the accuracy of ionospheric delay estimates along both the direct and reflected signal paths. Additionally, as the altimetric precision improves, corrections for smaller errors, like sea state bias, will become increasingly important. When trying to represent the observations, more accurate characterization of the observing system is important as well. For example, unique, and precisely measured antenna gain patterns for each spacecraft in the CYGNSS constellation should improve the measurement-model comparisons.

Today, GNSS-R is maturing into an accepted remote sensing technique for observing ocean, land, and ice surfaces. Research in this field is building the foundation for an exciting new way of thinking about remote sensing with opportunistic signals. This perspective will help to answer compelling science questions, and allow us to increase our understanding of our planet.

## Bibliography

- A. Alonso-Arroyo, A. Camps, H. Park, D. Pascual, R. Onrubia, and F. Martin. Retrieval of Significant Wave Height and Mean Sea Surface Level Using the GNSS-R Interference Pattern Technique: Results from a Three-month Field Campaign. IEEE Transactions on Geoscience and Remote Sensing, 53(6):3198 – 3209, 2015. ISSN 01962892.
- A. Alonso-Arroyo, V. Zavorotny, and A. Camps. Sea Ice Detection using GNSS-R Data from UK TDS-1. In 2016 IEEE International Geoscience and Remote Sensing Symposium (IGARSS), pages 2001–2004, July 2016.
- O. Andersen, P. Knudsen, and L. Stenseng. The DTU13 MSS (Mean Sea Surface) and MDT (Mean Dynamic Topography) from 20 Years of Satellite Altimetry. In International Association of Geodesy Symposia, 2015.
- O. B. Andersen. The DTU10 Gravity Field and Mean Sea Surface. In Second International Symposium of the Gravity Field of the Earth (IGFS2), 2010.
- M. Belmonte-Rivas. Bistatic Scattering of Global Positioning System Signals from Arctic Sea Ice. PhD thesis, University of Colorado, 2007.
- D. Bilitza. The International Reference Ionosphere – Status 2013. Advances in Space Research, 55(8):1914 – 1927, 2015. ISSN 0273-1177.
- J. J. Bommarito. DMSP Special Sensor Microwave Imager Sounder (SSMIS), 1993.
- F. K. Brunner. An Improved Model for Dual Frequency Ionospheric Correction of GPS Observations. Manuscripta Geodetica, 16:205–214, 1991.
- A. Camps, H. Park, I. Sekulic, and J. M. Rius. GNSS-R Altimetry Performance Analysis for the GEROS Experiment on Board the International Space Station. Sensors, 17(1583), 2017. ISSN 1424-8220. doi: 10.3390/s17071583.
- E. Cardellach, F. Fabra, O. Nogues-Correig, S. Oliveras, S. Ribo, and A. Rius. GNSS-R Ground-Based and Airborne Campaigns for Ocean, Land, Ice, and Snow Techniques: Application to the GOLD-RTR Data sets. Radio Science, 46, 2011.



- E. Cardellach, A. Rius, M. Martin-Neira, F. Fabra, O. Nogues-Correig, S. Ribo, J. Kainulainen, A. Camps, and S. D'Addio. Consolidating the Precision of Interferometric GNSS-R Ocean Altimetry Using Airborne Experimental Data. IEEE Transactions on Geoscience and Remote Sensing, 52(8):4992–5004, 2014.
- H. Carreno-Luengo, H. Park, A. Camps, F. Fabra, and A. Rius. GNSS-R Derived Centimetric Sea Topography: An Airborne Experiment Demonstration. IEEE Journal of Selected Topics in Applied Earth Observations and Remote Sensing, 6(3):1468–1478, June 2013. ISSN 1939-1404. doi: 10.1109/JSTARS.2013.2257990.
- H. Carreno-Luengo, A. Camps, P. Via, J. F. Munoz, A. Cortiella, D. Vidal, J. Jané, N. Catarino, M. Hagenfeldt, P. Palomo, and S. Cornara. 3Cat-2—An Experimental Nanosatellite for GNSS-R Earth Observation: Mission Concept and Analysis. IEEE Journal of Selected Topics in Applied Earth Observations and Remote Sensing, 9(10): 4540–4551, Oct. 2016. ISSN 1939-1404. doi: 10.1109/JSTARS.2016.2574717.
- H. Carreno-Luengo, S. Lowe, C. Zuffada, S. Esterhuizen, and S. Oveisgharan. Spaceborne GNSS-R from the SMAP Mission: First Assessment of Polarimetric Scatterometry over Land and Cryosphere. Remote Sensing, 9(4), 2017. ISSN 2072-4292. doi: 10.3390/rs9040362. URL <http://www.mdpi.com/2072-4292/9/4/362>.
- J. C. Ries B. J. Haines L. L. Fu P. S. Callahan Chelton, D. B. Satellite Altimetry and Earth Sciences. Academic Press, 2001.
- C. Chew, R. Shah, C. Zuffada, G. Hajj, D. Masters, and A.J. Mannucci. Demonstrating Soil Moisture Remote Sensing with Observations from the UK TechDemoSat-1 Satellite Mission. Geophysical Research Letters, 43(7):3317 – 3324, April 2016. ISSN 0094-8276.
- M. P. Clarizia, C. Ruf, P. Cipollini, and C. Zuffada. First Spaceborne Observation of Sea Surface Height Using GPS-Reflectometry. Geophysical Research Letters, 43(2):767 – 774, 2016. ISSN 00948276.
- S. F. Clifford, V. I. Tatarskii, A. G. Voronovich, and V. U. Zavorotny. GPS Sounding of Ocean Surface Waves: Theoretical Assessment. In 1998 IEEE International Geoscience and Remote Sensing Symposium (IGARSS), volume 4, pages 2005–2007 vol.4, July 1998. doi: 10.1109/IGARSS.1998.703722.
- CYGNSS. Level 1 Science Data Record Version 2.0. Ver. 2.0. PO.DAAC, CA, USA., 2017. URL <http://dx.doi.org/10.5067/CYGNS-L1X20>. Accessed: 09-21-2018.
- S. D'Addio, M. Martin-Neira, and C. Buck. End-to-end performance analysis of a PARIS in-orbit demonstrator ocean altimeter. In 2011 IEEE International Geoscience and Remote Sensing Symposium (IGARSS), pages 4387–4390, July 2011. doi: 10.1109/IGARSS.2011.6050204.
- J. L. Davis, T. A. Herring, I. I. Shapiro, A. E. E. Rogers, and G. Elgered. Geodesy by Radio Interferometry: Effects of Atmospheric Modeling Errors on Estimates of Baseline Length. Radio Science, 20(6):1593–1607, 1985. ISSN 1944-799X.

- T. L. Delworth, A. Rosati, W. Anderson, A. J. Adcroft, V. Balaji, R. Benson, K. Dixon, S. M. Griffies, H. Lee, R. C. Pacanowski, G. A. Vecchi, A. T. Wittenberg, F. Zeng, and R. Zhang. Simulated Climate and Climate Change in the GFDL CM2.5 High-Resolution Coupled Climate Model. Journal of Climate, 25(8):2755–2781, 2012.
- J. M. Dow, R. E. Neilan, and C. Rizos. The International GNSS Service in a Changing Landscape of Global Navigation Satellite Systems. Journal of Geodesy, 83(3):191 – 198, 2009.
- S. S. Drijfhout. Heat Transport by Mesoscale Eddies in an Ocean Circulation Model. Journal of Physical Oceanography, 24(2):353–369, 1994.
- T. Elfouhaily, B. Chapron, K. Katsaros, and D. Vandemark. A Unified Directional Spectrum for Long and Short Wind-driven Waves. Journal of Geophysical Research: Oceans, 102(C7):15781–15796, 1997. doi: 10.1029/97JC00467.
- T. Elfouhaily, D. R. Thompson, and L. Linstrom. Delay-Doppler Analysis of Bistatically Reflected Signals from the Ocean Surface: Theory and Application. IEEE Transactions on Geoscience and Remote Sensing, 40(3):560–573, Mar. 2002. ISSN 0196-2892. doi: 10.1109/TGRS.2002.1000316.
- T. M. Elfouhaily and J. T. Johnson. A New Model for Rough Surface Scattering. IEEE Transactions on Geoscience and Remote Sensing, 45(7):2300–2308, July 2007. ISSN 0196-2892. doi: 10.1109/TGRS.2006.890419.
- EUMETSAT. Ocean and Sea Ice Satellite Application Facility. Global Sea Ice Concentration Climate Data Record 1979-2015 (v2.0, 2017), 2017. URL <http://osisaf.met.no>. Accessed: 08-08-2017.
- F. Fabra, E. Cardellach, A. Rius, S. Ribo, S. Oliveras, O. Nogues-Correig, M.B. Rivas, M. Semmling, and S. D’Addio. Phase Altimetry With Dual Polarization GNSS-R Over Sea Ice. IEEE Transactions on Geoscience and Remote Sensing, 50(6):2112–2121, June 2012. ISSN 0196-2892. doi: 10.1109/TGRS.2011.2172797.
- R. Farneti, T. L. Delworth, A. J. Rosati, S. M. Griffies, and F. Zeng. The Role of Mesoscale Eddies in the Rectification of the Southern Ocean Response to Climate Change. Journal of Physical Oceanography, 40(7):1539–1557, 2010.
- J. L. Garrison and S. J. Katzberg. Detection of Ocean Reflected GPS Signals: Theory and Experiment. In Proceedings IEEE SOUTHEASTCON ’97. ‘Engineering the New Century’, pages 290–294, April 1997. doi: 10.1109/SECON.1997.598694.
- J. L. Garrison and S. J. Katzberg. The Application of Reflected GPS Signals to Ocean Remote Sensing. Remote Sensing of Environment, 73(2):175 – 187, 2000.
- J. L. Garrison, S. J. Katzberg, and M. I. Hill. Effect of Sea Roughness on Bistatically Scattered Range Coded Signals from the Global Positioning System. Geophysical Research Letters, 25(13):2257–2260, 1998. doi: 10.1029/98GL51615.

- J. L. Garrison, A. Komjathy, V. U. Zavorotny, and S. J. Katzberg. Wind Speed Measurement Using Forward Scattered GPS Signals. IEEE Transactions on Geoscience and Remote Sensing, 40(1):50–65, Jan. 2002. ISSN 0196-2892. doi: 10.1109/36.981349.
- A. Ghavidel, D. Schiavulli, and A. Camps. Numerical Computation of the Electromagnetic Bias in GNSS-R Altimetry. IEEE Transactions on Geoscience and Remote Sensing, 54(1): 489–498, Jan. 2016. ISSN 0196-2892.
- S. Gleason. Remote Sensing of Ocean, Ice, and Land Surfaces Using Bistatically Scattered GNSS Signals from Low Earth Orbit. PhD thesis, University of Surrey, 2006.
- G. A. Hajj and C. Zuffada. Theoretical Description of a Bistatic System for Ocean Altimetry Using the GPS Signal. Radio Science, 38(5), 2003. ISSN 1944-799X. doi: 10.1029/2002RS002787.
- M. T. Heath. Scientific Computing: An Introductory Survey. McGraw-Hill Higher Education, 2nd edition, 1996. ISBN 0070276846.
- M. Hernández-Pajares, J. M. Juan, J. Sanz, R. Orus, A. Garcia-Rigo, J. Feltens, A. Komjathy, S. C. Schaer, and A. Krankowski. The IGS VTEC Maps: A Reliable Source of Ionospheric Information Since 1998. Journal of Geodesy, 83(3):263–275, Mar. 2009. ISSN 1432-1394. doi: 10.1007/s00190-008-0266-1.
- B. Hofmann Wellenhopf, H. Lichtenegger, and J. Collins. Global Positioning System: Theory and Practice. Springer-Verlag Wien, 1997.
- IGS. IGS Products, GPS Satellite Ephemerides. URL <http://www.igs.org/products/data>. Accessed: 09-23-2018.
- P. Jales. MERRByS Product Manual. Technical Report XP X H - #0248366, Surrey Satellite Technology Ltd., May 2016.
- P. Jales and M. Unwin. Mission Description - GNSS Reflectometry on TDS-1 with the SGR-ReSI. Technical Report SSEP - #0248367, Surrey Satellite Technology Ltd., March 2015.
- S. G. Jin, G. P. Feng, and S. Gleason. Remote Sensing Using GNSS Signals: Current Status and Future Directions. Advances in Space Research, 47(10):1645 – 1653, 2011. ISSN 1645-1653.
- A. Komjathy. Global Ionospheric Total Electron Content Mapping Using the Global Positioning System. PhD thesis, University of New Brunswick, 1997.
- A. Komjathy, J. Maslanik, V. U. Zavorotny, P. Axelrad, and S. J. Katzberg. Sea ice remote sensing using surface reflected gps signals. In 2000 IEEE International Geoscience and Remote Sensing Symposium (IGARSS), volume 7, pages 2855–2857 vol.7, 2000.

- S. Kumar. Performance of IRI-2012 Model During a Deep Solar Minimum and a Maximum Year Over Global Equatorial Regions. Journal of Geophysical Research: Space Physics, 121(6):5664–5674, 2016. ISSN 2169-9402.
- J. Lambin, R. Morrow, L. Fu, J. K. Willis, H. Bonekamp, J. Lillibridge, J. Perbos, G. Zouche, P. Vaze, W. Bannoura, F. Parisot, E. Thouvenot, S. Coutin-Faye, E. Lindstrom, and M. Mignogno. The OSTM/Jason-2 Mission. Marine Geodesy, 33(sup1):4–25, 2010.
- K. M. Larson, E. E. Small, E. Gutmann, A. Bilich, P. Axelrad, and J. Braun. Using GPS Multipath to Measure Soil Moisture Flucuations: Initial Results. GPS Solutions, 12(3), 2008a.
- K. M. Larson, E. E. Small, E. D. Gutmann, A. L. Bilich, J. J. Braun, and V. U. Zavorotny. Use of GPS Receivers as a Soil Moisture Network for Water Cycle Studies. Geophysical Research Letters, 35(24), 2008b. ISSN 1944-8007. doi: 10.1029/2008GL036013. L24405.
- K. M. Larson, R. D. Ray, F. G. Nievinski, and J. T. Freymueller. The Accidental Tide Gauge: A GPS Reflection Case Study From Kachemak Bay, Alaska. IEEE Geoscience and Remote Sensing Letters, 10(5):1200–1204, Sept. 2013. ISSN 1545-598X. doi: 10.1109/LGRS.2012.2236075.
- R. Leandro, M. Santos, and R. B. Langley. UNB Neutral Atmosphere Models: Development and Performance. In Proceedings of the 2006 National Technical Meeting of The Institute of Navigation, volume 2, pages 564 – 573, Monterey, CA, United states, 2006.
- Z. Li, C. Zuffada, S. T. Lowe, T. Lee, and V. Zlotnicki. Analysis of GNSS-R Altimetry for Mapping Ocean Mesoscale Sea Surface Heights Using High-Resolution Model Simulations. IEEE Journal of Selected Topics in Applied Earth Observations and Remote Sensing, 9(10):4631–4642, Oct. 2016. ISSN 1939-1404. doi: 10.1109/JSTARS.2016.2581699.
- S. Lowe. Voltage SNR Nonlinearity Resulting from Incoherent Summations. Technical Report TMO Progress Rep. 42-137, NASA Jet Propulsion Laboratory, Pasadena, CA, May 1999. URL [http://tmo.jpl.nasa.gov/tmo/progress\\_report](http://tmo.jpl.nasa.gov/tmo/progress_report).
- S. T. Lowe, C. Zuffada, J. L. LaBrecque, M. Lough, J. Lerma, and L. E. Young. An Ocean-Altitude Measurement Using Reflected GPS Signals Observed from a Low-Altitude Aircraft. In 2000 IEEE International Geoscience and Remote Sensing Symposium (IGARSS), volume 5, pages 2185–2187 vol.5, 2000. doi: 10.1109/IGARSS.2000.858350.
- S. T. Lowe, J. L. LaBrecque, C. Zuffada, L. J. Romans, L. E. Young, and G. A. Hajj. First Spaceborne Observation of an Earth-Reflected GPS Signal. Radio Science, 37(1):1–28, 2002a. ISSN 1944-799X. doi: 10.1029/2000RS002539.
- S. T. Lowe, C. Zuffada, Y. Chao, P. Kroger, and L. E. Young. 5-cm Precision Aircraft Ocean Altimetry Using GPS Reflections. Geophysical Research Letters, 29(10), May 2002b.

- S.T. Lowe, P. Kroger, G. Franklin, J.L. LaBrecque, J. Lerma, M. Lough, M.R. Marcin, R.J. Muellerschoen, D. Spitzmesser, and L.E. Young. A Delay/Doppler-Mapping Receiver System for GPS-Reflection Remote Sensing. IEEE Transactions on Geoscience and Remote Sensing, 40(5):1150–1163, May 2002c. ISSN 0196-2892. doi: 10.1109/TGRS.2002.1010901.
- M. Martin-Neira. Passive Reflectometry and Interferometry System (PARIS). Application to Ocean Altimetry. ESA Journal (European Space Agency), 17(4):331 – 331, 1993. ISSN 03792285.
- M. Martin-Neira, S. D’Addio, C. Buck, N. Floury, and R. Prieto-Cerdeira. The PARIS Ocean Altimeter In-Orbit Demonstrator. IEEE Transactions on Geoscience and Remote Sensing, 49(6):2209–2237, June 2011. ISSN 0196-2892. doi: 10.1109/TGRS.2010.2092431.
- F. Martín, A. Camps, H. Park, S. D’Addio, M. Martín-Neira, and D. Pascual. Cross-Correlation Waveform Analysis for Conventional and Interferometric GNSS-R Approaches. IEEE Journal of Selected Topics in Applied Earth Observations and Remote Sensing, 7(5):1560–1572, May 2014. ISSN 1939-1404. doi: 10.1109/JSTARS.2014.2300232.
- J. Mashburn, P. Axelrad, S. T. Lowe, and K. M. Larson. An Assessment of the Precision and Accuracy of Altimetry Retrievals for a Monterey Bay GNSS-R Experiment. IEEE Journal of Selected Topics in Applied Earth Observations and Remote Sensing, 9(10):4660–4668, Oct. 2016. doi: 10.1109/JSTARS.2016.2537698.
- J. Mashburn, P. Axelrad, S. T. Lowe, and K. M. Larson. Global Ocean Altimetry with GNSS Reflections from TechDemoSat-1. IEEE Transactions on Geoscience and Remote Sensing, 56(7):4088–4097, July 2018.
- D. Masters. Initial Results of Land-Reflected GPS Bistatic Radar Measurements in SMEX02. Remote Sensing of Environment, 92:507–520, Sept. 2004. doi: 10.1016/j.rse.2004.05.016.
- D. Masters. Surface Remote Sensing Applications of GNSS Bistatic Radar: Soil Moisture and Aircraft Altimetry. PhD thesis, University of Colorado Boulder, 2004.
- D. Masters, P. Axelrad, V. Zavorotny, S.J. Katzberg, and F. Lalezari. A passive GPS Bistatic Radar Altimeter for Aircraft Navigation. In Proceedings of the 14th International Technical Meeting of the Satellite Division of The Institute of Navigation (ION GPS 2001), pages 2435–2445, September 2001.
- D. D. McCarthy and G. Petit. IERS Conventions 2003 (IERS Technical Note). Technical Report No. 32, Frankfurt am Main: Verlag des Bundesamts für Kartographie und Geodäsie, 2004.
- F. Mesinger, G. DiMego, E. Kalnay, K. Mitchell, P. C. Shafran, W. Ebisuzaki, D. Jović, J. Woollen, E. Rogers, E. H. Berbery, M. B. Ek, Y. Fan, R. Grumbine, W. Higgins, H. Li, Y. Lin, G. Manikin, D. Parrish, and W. Shi. North american regional reanalysis. Bulletin of the American Meteorological Society, 87(3):343–360, 2006. doi: 10.1175/BAMS-87-3-343.

- P. Misra and P. Enge. Global Positioning System: Signals, Measurements and Performance Second Edition. Massachusetts: Ganga-Jamuna Press, 2006.
- O. Montenbruck and E. Gill. Ionospheric Correction for GPS Tracking of LEO Satellites. Journal of Navigation, 55(2):293 – 304, May 2002. ISSN 0373-4633.
- NASA. Decadal Technology Roadmaps: Science Instruments, Observatories, and Sensor Systems, 2015. URL <https://www.nasa.gov/offices/oct/home/roadmaps/index.html>. Accessed: 10-31-2018.
- NASA Jet Propulsion Laboratory. GIPSY-OASIS Orbit Analysis Simulation Software, 2018. URL [gipsy-oasis.jpl.nasa.gov](https://gipsy-oasis.jpl.nasa.gov). Accessed: 10-22-2018.
- A. E. Niell. Global Mapping Functions for the Atmosphere Delay at Radio Wavelengths. Journal of Geophysical Research: Solid Earth, 101(B2):3227–3246, 1996. ISSN 2156-2202.
- NOAA. OSTM/Jason-2 Products Handbook, 2011. URL [http://www.ospo.noaa.gov/Products/documents/OSTMJason-2Products\\_Handbook.pdf](http://www.ospo.noaa.gov/Products/documents/OSTMJason-2Products_Handbook.pdf). Accessed: 06-20-2017.
- NOAA. National Data Buoy Center, 2015. URL <http://www.ndbc.noaa.gov/>. Accessed: 09-03-2015.
- NSIDC. AMSR Instrument Description, 2001. URL [https://nsidc.org/data/docs/daac/amsr\\_instrument.gd.html](https://nsidc.org/data/docs/daac/amsr_instrument.gd.html). Accessed: 08-24-2017.
- J. Park. Investigations of GNSS-R for Ocean Wind, Sea Surface Height, and Land Surface Remote Sensing. PhD thesis, The Ohio State University, 2017. URL [http://rave.ohiolink.edu/etdc/view?acc\\_num=osu1512095954817037](http://rave.ohiolink.edu/etdc/view?acc_num=osu1512095954817037).
- J. Park, J. T. Johnson, and S. T. Lowe. A Study of the Electromagnetic Bias for GNSS-R Ocean Altimetry Using the Choppy Wave Model. Waves in Random and Complex Media, 26(4):599–612, 2016. doi: 10.1080/17455030.2016.1179820.
- J. Park, J. T. Johnson, A. O’Brien, and Y. Yi. Investigating “Rapid Revisit” Observations of CYGNSS. In 2017 IEEE International Geoscience and Remote Sensing Symposium (IGARSS), pages 2659–2660, July 2017. doi: 10.1109/IGARSS.2017.8127543.
- C. G. Rapley, H. D. Griffiths, and P. A. M. Berry. Executive Summary of the Proceedings of the Consultative Meeting on Imaging Altimeter Requirements and Techniques. June 1990.
- R. D. Ray. A Global Ocean Tide Model from TOPEX/POSEIDON Altimetry: GOT99.2. Technical Report NASA/TM-1999-209478, NASA Goddard Space Flight Center, Greenbelt, MD, USA, 1999.
- A. Rius, E. Cardellach, and M. Martin-Neira. Altimetric Analysis of the Sea-Surface GPS-Reflected Signals. IEEE Transactions on Geoscience and Remote Sensing, 48(4):2119–2127, April 2010. ISSN 0196-2892. doi: 10.1109/TGRS.2009.2036721.

- D. Roma, M. Pajares, A. Krankowski, K. Kotulak, R. Ghoddousi-Fard, Y. Yuan, Z. Li, H. Zhang, C. Shi, C. Wang, J. Feltens, P. Vergados, A. Komjathy, S. Schaer, A. García-Rigo, and J.M. Gómez Cama. Consistency of Seven Different GNSS Global Ionospheric Mapping Techniques During One Solar Cycle. *Journal of Geodesy*, 92(6):691–706, Nov. 2017. doi: 10.1007/s00190-017-1088-9.
- C. S. Ruf, R. Atlas, P. S. Chang, M. P. Clarizia, J. L. Garrison, S. Gleason, S. J. Katzberg, Z. Jelenak, J. T. Johnson, S. J. Majumdar, A. O’Brien, D. J. Posselt, A. J. Ridley, R. J. Rose, and V. U. Zavorotny. New Ocean Winds Satellite Mission to Probe Hurricanes and Tropical Convection. *Bulletin of the American Meteorological Society*, 97(3):385–395, 3 2016. ISSN 1087-3562. doi: 10.1175/BAMS-D-14-00218.1.
- A. M. Semmling, T. Schmidt, J. Wickert, S. Schön, F. Fabra, E. Cardellach, and A. Rius. On the Retrieval of the Specular Reflection in GNSS Carrier Observations for Ocean Altimetry. *Radio Science*, 47(6), 2012. ISSN 1944-799X. doi: 10.1029/2012RS005007. RS6007.
- A. M. Semmling, J. Wickert, S. Schön, R. Stosius, M. Markgraf, T. Gerber, M. Ge, and G. Beyerle. A Zeppelin Experiment to Study Airborne Altimetry Using Specular Global Navigation Satellite System Reflections. *Radio Science*, 48(4):427–440, 2013. ISSN 1944-799X. doi: 10.1002/rds.20049.
- A. M. Semmling, G. Beyerle, J. Beckheinrich, M. Ge, and J. Wickert. Airborne GNSS Reflectometry Using Crossover Reference Points for Carrier Phase Altimetry. In *2014 IEEE International Geoscience and Remote Sensing Symposium (IGARSS)*, pages 3786–3789, July 2014.
- A. M. Semmling, V. Leister, J. Saynisch, F. Zus, S. Heise, and J. Wickert. A Phase Altimetric Simulator: Studying the Sensitivity of Earth-Reflected GNSS Signals to Ocean Topography. *IEEE Transactions on Geoscience and Remote Sensing*, 54(11):6791–6802, Nov. 2016. doi: 10.1109/TGRS.2016.2591065.
- M. C. Serreze, J. E. Walsh, F. S. Chapin, T. Osterkamp, M. Dyurgerov, V. Romanovsky, W. C. Oechel, J. Morison, T. Zhang, and R. G. Barry. Observational Evidence of Recent Change in the Northern High-Latitude Environment. *Climatic Change*, 46(1):159–207, Jul 2000. ISSN 1573-1480.
- D. Stammer, R. D. Ray, O. B. Andersen, B. K. Arbic, W. Bosch, L. Carrère, Y. Cheng, D. S. Chinn, B. D. Dushaw, G. D. Egbert, S. Y. Erofeeva, H. S. Fok, J. A. M. Green, S. Griffiths, M. A. King, V. Lapin, F. G. Lemoine, S. B. Luthcke, F. Lyard, J. Morison, M. Müller, L. Padman, J. G. Richman, J. F. Shriver, C. K. Shum, E. Taguchi, and Y. Yi. Accuracy Assessment of Global Barotropic Ocean Tide Models. *Reviews of Geophysics*, 52(3):243–282, 2014. ISSN 1944-9208. doi: 10.1002/2014RG000450.
- B. D. Tapley, B. E. Schutz, and G. H. Born. *Statistical Orbit Determination*. Academic Press, 2004. doi: <https://doi.org/10.1016/B978-012683630-1/50019-9>.

- M. Unwin, S. Gleason, and M. Brennan. The Space GPS Reflectometry Experiment on the UK Disaster Monitoring Constellation Satellite. In Proceedings of the 16th International Technical Meeting of the Satellite Division of The Institute of Navigation (ION GPS/GNSS 2003), pages 2656–2663, September 2003.
- M. Unwin, R. De Vos Van Steenwijk, C. Gommenginger, C. Mitchell, and S. Gao. The SGR-ReSI - A New Generation of Space GNSS Receiver for Remote Sensing. In Proceedings of the 24th International Technical Meeting of The Satellite Division of the Institute of Navigation (ION GNSS 2011), pages 1061 – 1067, Portland, OR, United states, 2010.
- M. Unwin, P. Blunt, R. De Vos Van Steenwijk, S. Duncan, G. Martin, and P. Jales. GNSS Remote Sensing and Technology Demonstration on TechDemoSat-1. In Proceedings of the 24th International Technical Meeting of The Satellite Division of the Institute of Navigation (ION GNSS 2011), pages 2970 – 2975, Portland, OR, United states, 2011.
- A. G. Voronovich and V. U. Zavorotny. Bistatic Radar Equation for Signals of Opportunity Revisited. IEEE Transactions on Geoscience and Remote Sensing, 56(4):1959–1968, April 2018. ISSN 0196-2892. doi: 10.1109/TGRS.2017.2771253.
- J. Wickert, E. Cardellach, M. Martín-Neira, J. Bandejas, L. Bertino, O. B. Andersen, A. Camps, N. Catarino, B. Chapron, F. Fabra, N. Floury, G. Foti, C. Gommenginger, J. Hatton, P. Høeg, A. Jäggi, M. Kern, T. Lee, Z. Li, H. Park, N. Pierdicca, G. Ressler, A. Rius, J. Roselló, J. Saynisch, F. Soulat, C. K. Shum, M. Semmling, A. Sousa, J. Xie, and C. Zuffada. GEROS-ISS: GNSS Reflectometry, Radio Occultation, and Scatterometry Onboard the International Space Station. IEEE Journal of Selected Topics in Applied Earth Observations and Remote Sensing, 9(10):4552–4581, Oct. 2016. ISSN 1939-1404.
- S. Wu, T. Meehan, and L. Young. Potential Use of GPS Signals as Ocean Altimetry Observables. In Proceedings of the 1997 National Technical Meeting of The Institute of Navigation, pages 543 – 550, Santa Monica, CA, USA, 1997.
- Qingyun Yan and Weimin Huang. Spaceborne GNSS-R Sea Ice Detection Using Delay-Doppler Maps: First Results From the UK TechDemoSat-1 Mission. IEEE Journal of Selected Topics in Applied Earth Observations and Remote Sensing, 9:4795–4801, 10 2016. doi: 10.1109/JSTARS.2016.2582690.
- V. Zavorotny and A. Voronovich. Scattering of GPS Signals from the Ocean with Wind Remote Sensing Application. IEEE Transactions on Geoscience and Remote Sensing, 38(2):951–964, Mar. 2000. ISSN 0196-2892.
- V. U. Zavorotny and A. G. Voronovich. Bistatic Radar Scattering from an Ocean Surface in the Small-Slope Approximation. In 1999 IEEE International Geoscience and Remote Sensing Symposium (IGARSS), volume 5, pages 2419–2421 vol.5, 1999. doi: 10.1109/IGARSS.1999.771529.
- C. Zuffada and V. Zavorotny. Coherence Time and Statistical Properties of the GPS Signal Scattered Off the Ocean Surface and Their Impact on the Accuracy of Remote Sensing of



Sea Surface Topography and Winds. In 2001 IEEE International Geoscience and Remote Sensing Symposium (IGARSS), volume 7, pages 3332 – 3334, 02 2001. ISBN 0-7803-7031-7.